Individual and joint inversion of surface wave tomography for near-surface applications

Ph.D. in
Civil and Environmental Engineering (34th Cycle)

Individual and joint inversion of surface wave tomography for near-surface applications

Mohammadkarim Karimpour

******

Supervisor(s):
Prof. Laura Valentina Socco
Prof. Evert Slob

Politecnico di Torino
2022

Acknowledgement

I would like to thank my Ph.D. supervisor Prof. Valentina Socco from the bottom of my heart. This work would have not been possible without her priceless experience and deep knowledge of geophysics, continuous guidance during my Ph.D., and constructive suggestions.

My sincere gratitude to Prof. Evert Slob to make me feel like home during my stay in Delft, and for being a mentor to me both in my academic and personal life.

I thank Compagnia di San Paolo for funding my Ph.D. scholarship. I am also grateful to Maria, Jens, Marat, Hamed, and Dieter for their collaboration in data acquisition.

I would like to thank Prof. Alberto Godio for his constant evaluation of my work during the whole Ph.D. period.

My deepest gratitude to Farbod for his scientific and moral supports during the challenging times of my Ph.D.

Finally, I thank my family for motivating me and their unconditional supports.

List of Symbols and Acronyms

VS	S-wave velocity
VP	P-wave velocity
SW	Surface waves
BW	Body waves
DC	Dispersion curve
SWT	Surface wave tomography
BWT	Body wave tomography
f	Frequency
V	Phase velocity
σ	Standard deviation
h	Layer thickness
v	Poisson's ratio
p	Phase slowness
s	slowness
Φ	Misfit function
ρ	Density
t	Time
λ	Damping factor
fw	Forward response
N	Number of layers
K	Number of model points
n_{DC}	Number of dispersion curves
n_c	Number of inversion cells

n_d	Number of data points
$\mathbf{d}_{\text{exp}}$	Vector of experimental data
$\mathbf{R}$	Spatial regularization matrix
$\mathbf{m}$	Model
$\mathbf{C}_{\text{exp}}$	Data covariance matrix
$\mathbf{C}_R$	Regularization covariance matrix
$\mathbf{G}$	Sensitivity matrix
$\mathbf{tt}$	first-arrival travel times

Table of Contents

Chapter 1

Introduction

1.1 Background and Motivation

The shallow Earth subsurface is interested by human activities and the properties of the shallow geological formations have significant impact on them. Therefore, the knowledge about subsurface property distribution is of paramount importance for planning, designing, managing, and assessing all those actions which are affected by them. Shallow subsurface modelling is of great significance in different fields like civil engineering, seismic hazard, mining industry, climate change mitigation and adaptation, and hydrocarbon exploration.

In civil engineering, to plan and design foundations or underground works, the knowledge of mechanical properties of soils and shallow bedrock is a key element in reducing geological risk during works and also during infrastructure life and decommissioning (Anbazhagan et al., 2013). With this respect, not only on land, but also shallow water offshore investigations are becoming a fundamental step in the design of windmills power plants and other offshore infrastructures (Wang et al., 2018). Local variation of soil stiffness or bedrock depth can represent important information particularly in heterogeneous geological setting like karst areas (Bačić et al., 2020).

The prediction of ground motion in high seismicity regions requires the detailed model of the distribution of seismic velocities, particularly shear-wave velocity (VS) model (Thomas et al., 2016). The velocity model is the input for seismic

hazard modelling, and it is the basis for seismic zonation in many national and international regulations and codes (Gerstenberger et al., 2020). Moreover, the distribution of Poisson's ratio, that can be retrieved from seismic data, can be considered a proxy for the liquefaction risk in liquefaction prone areas (Kutanaei and Choobbasti, 2019). Also, in the study of seismicity induced by hydrocarbon industry, the shallow velocity model is a key knowledge to estimate the expected seismicity effect (Grigoli et al., 2017).

In mining industry, the mechanical properties distributions have value both at the exploration phase, where they can be used to map ore bodies and their extent, geometry and characteristics (Manzi et al., 2015), and at the mine development phase where they can be used to plan the engineering works, the drilling and digging, and have a major role in operation de-risking.

The challenges related to climate change impose the design and implementation of actions aimed at climate change mitigation and adaptation. In both contexts, the shallow subsurface characterization has major relevance. In mitigation actions, negative technologies, such as CO2 underground storage, require monitoring for underground fluid flows and for potential induced hazard such as subsidence (Kelemen et al., 2019). In adaptation measures are included levee and earthen dam characterization and monitoring (François et al., 2019), shallow waterbed evolution assessment (Rosendahl, 2019), landslide and unstable slope characterization and monitoring (Almeida et al., 2017), glacier and permafrost characterization and monitoring (Roe et al., 2017), rock falls and fracture detection (Mourey et al., 2019), monitoring of arid zone and desertification phenomena (Guo et al., 2017). For all these topics, the distribution of mechanical properties plays a major role and can be used either as proxy or as design and assessment parameters.

In hydrocarbon exploration and in deep seismic exploration in general, the shallow part of the subsurface is commonly known to have low-velocity and highly heterogeneous structures. It is important to build the velocity distribution of the shallow subsurface even if the target exists at deeper portions of the subsurface. If the seismic data from the shallow subsurface is not treated properly, it impacts the modelling of the deeper structures (Sheriff, 2002). Static correction is carried out to address this issue by correcting the travel times within the weathering layer. The accuracy of the constructed near-surface velocity model directly affects the accuracy of the static correction.

The shallow subsurface velocity models for the above applications can be obtained by analysing surface waves (SW). SW are usually present in the seismic data and dominate seismic recordings. The reason is that most of the produced energy by a source acting on the surface is transformed into surface waves (Richart et al., 1970). Moreover, the geometric attenuation of SW is considerably lower than body waves (BW) since SW propagate with a cylindrical wavefront, but BW have a spherical one (Aki and Richards, 1980).

Surface waves are dispersive, meaning that in a vertically heterogeneous medium, the phase velocity is frequency dependent. Dispersion curves (DCs) can be estimated from seismic recordings and then inverted to produce subsurface velocity models. Surface waves are mainly sensitive to the VS distribution of the subsurface (Xia et al., 1999). Hence, SW are usually analysed to obtain subsurface VS models.

There are different methods to invert the surface wave data. Surface wave tomography (SWT) is a powerful method that has been widely used in seismological studies. SWT was introduced in global seismology based on earthquake signals in early 1980s which led to the construction of the first global upper mantle models based on surface wave data (Masters et al., 1982; Woodhouse and Dziewonski, 1984; Nataf et al., 1986; Tanimoto, 1986). The first example of SWT inversion with a local parameterization in horizontal direction was proposed by Gu et al. (2001). Chiao and Kuo (2001) suggested a regularization approach to address the nonuniform sampling issue of SWT. Besides mantle studies, SWT has also been used for crustal studies since having a proper model of the Earth's crust, including the Moho depth, impacts the retrieved velocity model of the mantle (Smith and Masters, 1989; Woodhouse and Masters, 1991; Montagner, 1991; Li and Romanowicz, 1996; Boschi and Esktrom, 2002). SWT based on earthquake generated signals has some limitations. For instance, earthquake sources are not homogeneously distributed (mainly concentrated near plate boundaries) and the recorded signal at distant stations lacks the high-frequency information due to intrinsic attenuation. Shapiro and Campillo (2004) proposed SWT based on cross-correlation of recorded ambient seismic noise data over long periods of time. The advantage is that the noise can be recorded in any location. Shapiro et al. (2005) demonstrated the reliability of the noise cross-correlation. They computed the cross-correlation of monthly recorded ambient noise data and showed that the results from different months are like one another. Yao et al. (2006) introduced the application of empirical Green's functions to retrieve Rayleigh wave phase velocity

from ambient noise data and Lin et al. (2008) extended the application of SWT from ambient seismic noise to Love waves.

SWT usually consists of three steps (Yoshizawa and Kennett, 2004; Yao et al., 2008). First, different path-averaged dispersion curves (DCs) are computed for different receiver pairs aligned with a source. Then, the DCs are inverted to build phase velocity maps at different period (frequency). Finally, the obtained phase velocity maps are inverted to produce 1D VS models at different locations. However, the efficiency of SWT can be increased by the direct inversion of the path-averaged DCs, i.e., skipping the intermediate step of building phase velocity maps (Boschi and Ekstrom, 2002; Boiero, 2009; Fang et al., 2015).

In seismology, it is traditionally assumed that SW propagate along the great circle between the source and receiver (Trampert and Woodhouse, 1995; Ritzwoller and Levshing, 1998; Boschi and Ekstrom, 2002; Yao et al., 2010; Bussat and Kugler, 2011; Kästle et al., 2018). Alternatively, some researchers have used curved-ray SWT in which ray tracing is performed at each frequency (Spetzler et al., 2002; Trampert and Spetzler, 2006; Lin et al., 2009). Compared to seismology, the application of SWT to near-surface seismic studies is more recent. Kugler et al. (2007) employed SWT to characterize shallow-water marine sediments using Scholte waves dispersion data. Gouédard et al. (2010) applied SWT to an exploration dataset. Rector et al. (2015) applied SWT to construct a VS mode in a mining site. Ikeda and Tsuji (2020) applied SWT to exploration seismic data and constructed a subsurface VS model by inverting the phase velocity maps. Barone et al. (2021) applied three different tomography algorithms, which have been used in seismology, at the exploration scales. They used fast marching surface tomography method (Rawlinson, 2005), the reversible jump algorithm (Bodin and Sambridge, 2009), and the eikonal tomography (Lin et al., 2009) to build 3D phase velocity maps and then performed a depth inversion to obtain 3D VS models. Alternatively, some researchers have applied SWT in their near-surface studies to construct VS models directly from DC data, skipping the phase velocity maps (Da Col et al., 2020; Khosro Anjom, 2021).

Despite seismology, a study between the performance of straight-ray and curved-ray SWT at near-surface scale is missing. It seems to be important since the level of complexity and lateral heterogeneity at near-surface scale is much higher than at seismological studies and the straight-ray approximation of surface waves propagation may not be valid. Therefore, the question is would curved-ray SWT by means of ray tracing at each frequency, improve the 3D estimated model?

Each geophysical inversion method has intrinsic limitations. SW methods suffer from non-uniqueness and ill-posedness, and the inverse problem is mixed determined. SWT inversion, both straight-ray and curved-ray approaches, also suffers from these problems. An effective method to reduce the limitation of individual inversion methods is through joint inversion approaches. In joint inversion schemes, different datasets are inverted simultaneously rather than individually. The obtained model from joint inversion is internally more consistent and mitigates the interpretation ambiguities that might arise from individual inversions. It has been shown that the integration of complementary geophysical methods in joint inversion schemes can provide superior results to individual inversions. The first application of joint inversion can be found in the work by Vozoff and Jupp (1975) in which the magnetotelluric and resistivity data were combined to build a subsurface resistivity model. Since then, joint inversion has received significant attention and different kinds of datasets were integrated and various types of joint inversion methods have been proposed (Gallardo and Meju, 2003; Moorkamp et al., 2011; Ogunbo et al, 2018; Paulatto et al., 2019). In most of joint inversion approaches, the individual methods are related to each other by imposing the same geometry to the model. Petrophysical relationships can be integrated into the joint inversion if they can reliably link the model parameters from individual methods.

Different approaches have been proposed for structural coupling in joint inversion. Zhang and Morgan (1997) suggested a method for the joint inversion of seismic and electrical data in which the structural constraint was imposed on the model by a 'curvature' operator, i.e., Laplacian. Gallardo and Meju (2003) introduced cross-gradient as a structural constraint in the joint inversion of resistivity and seismic travel time data. In this approach, the model is constrained by forcing the directions of the model parameters to be parallel. Haber and Gazit (2013) suggested joint total variation approach in which the structural similarity was measured based on the norms of the absolute spatial gradient values of the models. Lien (2013) proposed a method for structural coupling of model parameters in which the structure was considered as transition between dominating parameter values and inverted for a common model parameter that represented the structure in the different parameter fields. Boiero and Socco (2014) presented a joint inversion method for P-wave first arrival times and DCs using layer thickness as the structural constraint. Having a physical link, when available, can further improve the results of the joint inversion. The model parameters can be linked from an empirical formula (De Stefano, 2011; Garofalo et al., 2015; Wagner et al., 2019; Mollaret et al., 2020) or using the information from well log measurements (Jegen

et al., 2009; Dell'Aversana et al., 2011; Gao et al., 2012a; Heincke et al., 2017). Nevertheless, care should be taken since errors in the rock-physics relations may produce highly erroneous results (Colombo and Rovetta, 2018).

To mitigate the intrinsic limitations of SWT, we propose a joint inversion scheme to integrate body wave tomography (BWT) and SWT using Poisson ratio as the physical constraint between the two methods for near-surface applications. BWT based on first-arrival time data consists of inverting the P-wave first-arrival times to build P-wave velocity (VP) models. The input data for both BWT and SWT methods are usually present in near-surface recordings. This can facilitate the use of the joint inversion of BWT and SWT for near-surface applications. The integration of these two methods in a joint inversion scheme might reduce the associated limitations of the individual SWT by applying the physical constraint. In other words, in the joint inversion of SWT and BWT, the VS model from SWT and the VP model from BWT can be constrained through Poisson's ratio. This might produce physically more meaningful models, compared to individual inversions. Moreover, the VP and VS models from the joint inversion might be more accurate than individual inversions.

The current thesis investigates the following schemes for near-surface velocity modelling in details:

- What are the differences between the performance of straight-ray and curved-ray SWT at near-surface scale, particularly in terms of the accuracy and computational cost?
- Is it possible to improve the obtained VS model from SWT through a joint inversion scheme between SWT and BWT? And how would the VP model from the joint inversion be different from individual BWT inversion?

To investigate these questions, we implemented SWT (straight-ray and curved ray approaches) and BWT in Python. To evaluate the accuracy and efficiency of the proposed algorithms and the implemented codes, we apply them to different numerical and field examples.

1.2 Outline

In Chapter 2, we describe the models, fields, and datasets that are used in this thesis. We describe five examples, including three numerical and two field

examples, and estimate DCs and P-wave travel times for them. We first address the acquisition strategies and the applied method to optimise the shot positions in 3D. Then we briefly illustrate the processing steps to retrieve the DCs from the raw data with their corresponding uncertainties. The synthetic models are aimed at testing the developed methods on specific targets and features. We use a numerical Step model which simulate a 2D faulty medium; a numerical Blocky model that includes two sharp blocks of low- and high-velocity anomalies; the Sand Bar model which is designed as a pre-study for a field data acquisition in Pijnacker, Netherlands and consists of a sand-filled channel embedded in a clay medium. We then describe sites, acquisition layouts and parameters, and data of the two field cases. At the Pijnacker field, characterised by a sand bar embedded in saturated soft organic soil, we acquired 2D and 3D data. The CNR field contains an artificial loose sand body surrounded by silty gravels. Also, for CNR site we acquired both 2D and 3D data but differently from the other three 3D examples, the CNR 3D dataset was acquired using a classical cross-spread layout. We show the impact of the acquisition layouts on the final DC coverage of SWT.

In Chapter 3, we explain the employed methodologies. We first present the SWT inversion algorithm and explain the difference between straight-ray and curved-ray SWT approaches. Then, we describe the proposed algorithm for the joint inversion of BWT and SWT. We also explain the method to integrate these two methods, the normalisation strategy, and the employed approach to integrate the two methods by means of a physical constrain.

Chapter 4 presents the evaluation between the performance of straight-ray and curved-ray SWT at the near-surface scale. The two SWT methods are applied to four 3D examples and the results are shown for the Blocky Model, the Sand Bar Model, the Pijnacker example, and the CNR example. For each example, the inversions start from the same initial model and the results are compared in terms of data misfit, model misfit, and computational cost.

In Chapter 5, we apply the physically constrained joint inversion SWT and BWT to three 2D and one 3D examples. For each example, we compare the results from individual inversions with joint inversion. In 3D, we employ the joint inversion algorithm in two different ways: joint inversion of straight-ray SWT and BWT, and also joint inversion of curved-ray SWT and BWT. Both methods are applied to the CNR 3D dataset, and the results are compared with individual inversions.

In Chapter 6, we summarise the final remarks of the thesis and provide some recommendations for future works.

Chapter 2

Models, fields, and datasets

To assess the performances of the methods and the effectiveness and efficiency of the implemented codes we use a series of datasets. Synthetic datasets are used to test the capability of the surface wave tomography and of the surface and body wave joint tomography to resolve challenging near surface targets such as subvertical discontinuities, blocky anomalies embedded in smooth velocity gradients with positive or negative velocity contrasts. Synthetic data are also used to simulate field test site properties and help in field survey design. Field data were acquired in well controlled test sites to assess the performances of the methods on real site conditions.

Both synthetic and field data are generated in 2D and 3D configuration. The acquisition layouts of the 3D data are chosen either optimising the source positions to maximize the data coverage with a minimum number of sources or as classical cross spread 3D scheme.

In the following sections, we describe the shot optimisation criteria, data processing approach, model and site features, acquisition layouts, examples of raw and processed data, and the inter-station coverage of DCs for each dataset.

2.1 Optimisation of source positions

The acquisition of optimal datasets for 3D surface wave tomography requires survey design aimed at maximizing the data coverage both from azimuth and wavelength point of view. The optimisation of source positions affects the amount of retrieved information significantly. In the presented examples we optimise the shot positions to obtain acquisition layouts which can produce high coverage of DCs. We also use a dataset where the acquisition layout mimics at a smaller scale the classical seismic exploration 3D cross-spread acquisition scheme with orthogonal lines of sources and receivers. This dataset, not being optimised will help analysing the criticalities introduced by a non-optimal acquisition scheme.

For SWT, we use a cross-correlation method to extract a DC between every receiver pair aligned with a source. In a 2D seismic line, all the shots and receivers are in-line and many DCs can be extracted from different receiver pairs. With *nr* as the number of receivers, the maximum number of unique receiver pairs (i.e., maximum number of DCs) would be (*nr**(*nr*-1)/2).

In a 3D SWT study, the acquisition layout should be designed carefully to make sure that high coverage of data can be extracted from the recordings. Varangoulis (2014) proposed a procedure to optimise the source positions for acquisition setups with regular grids of receivers. Da Col et al. (2020) optimised positions of (irregular) receivers for a set of pre-defined source positions. In our 3D examples, we use the former method in which the azimuthal coverage and the number of in-line receiver pairs with a source are used to optimise the source positions for a regular grid of receivers. In the following, we briefly explain the employed procedure to optimise the shot positions.

It should be noted that to optimise the theoretical DC coverage, we assume that a DC can be estimate between every receiver pair aligned with a source, and the ray paths between every receiver pair are straight lines. The actual coverage of DCs is obtained after processing the raw data (explained in Section 2.2) and it depends on the quality of the data, the frequency of the retrieved DCs, and the velocity distribution of the medium, which can perturb the ray paths from the straight lines.

For each 3D example, after defining the receiver grid, we first define many shot positions in a regular grid with a spacing equal to or less than the receivers spacing. For each shot, we find all the receiver pairs aligned with the shot using the developed code by Da Col et al. (2020). After computing all the possible receiver pairs for all the defined shot positions, the shots are sorted based on either their azimuthal coverage and on the number of in-line receiver pairs with each shot. We apply the latter criterion for the shot selection. For each 3D example, we pick the shots which could provide the greatest number of unique DCs and plotted the data coverage (inter-station paths). If the obtained theoretical DC coverage is satisfactory also from the azimuth point of view, we consider the selected shots as the final ones. Otherwise, more shots are added to increase the data coverage.

2.2 Data processing

The input data in this thesis are first-arrival times and DCs. We pick the first-arrival times manually on the seismograms. We do not apply any filters to the data

and use MATLAB to visualize the recorded signals. If the location of the first-arrival time in a seismogram is not clear and masked by noise, we do not pick it. The DCs are extracted from the raw data. Hence, we explain the processing steps to extract the DCs in Section 2.2.1. Moreover, we provide the used criteria to assess the experimental uncertainty of the DC data in Section 2.2.2.

2.2.1 DC extraction

We use a MATLAB code that automatically retrieves the DCs between each receiver pair that are collinear with a source. Here, we provide the general concepts based on which the code estimated the DCs from the raw data (for detail see Papadopoulou, 2021).

For each receiver pair, a frequency-domain narrow band-pass Gaussian filter, which was originally proposed by Dziewonski and Hales (1972), is used to analyse the traces into monochromatic components. The traces are then cross-correlated frequency by frequency to produce the cross-correlation matrix. The phase velocities of SW correspond to the maxima on the cross-correlation matrix, but there are many maxima. Hence, to avoid ambiguity in picking the correct maxima, a reference DC is used. The reference DC is estimated automatically using multichannel analysis method (Park et al., 1998) for the positions near to the receiver pair. The code picks all candidate DCs on each cross-correlation matrix. Then, the candidate that is closest to the reference DC at all frequencies is picked. Afterward, a set of QC processes allow to automatically reject data points that do not follow the smooth trend of the DC and also to remove poor quality DCs (Papadopoulou, 2021).

2.2.2 Data uncertainty

If a receiver pair is in-line with several shots, the DC for the receiver pair can be extracted both on individual and stacked cross-correlation matrices. Then, the standard deviation of the phase velocities can be computed based on the picked DCs in the individual-shot cross-correlation matrices. This standard deviation can be used later as the experimental uncertainty in the inversion process.

Alternatively, the experimental uncertainties of the DC data can be obtained based on the equation proposed by Passeri (2019), in which he investigated the uncertainty of the DC data for 52 sites and proposed an equation to approximate the standard deviation (σ) of the phase velocities as a function of frequency (f) and phase velocity (V) values as:

$$\sigma = \left[0.2822\ \sigma^{-0.1819 f} + 0.0226\ \sigma^{0.0077 f} \right] * V \qquad 2.1$$

Since for many of the receiver pairs, particularly in our synthetic examples, there is only one in-line shot, we use the approach suggested by Passeri (2019) to compute the uncertainties of the DC data for all the synthetic and field examples for consistency.

2.3 Synthetic models and datasets

We use three numerical examples including a 2D model and two 3D models. The purpose of the 2D model is to compare the joint inversion of BWT and SWT with individual inversions in presence of a sharp lateral velocity variations. We generate the 3D examples to investigate the performance of straight-ray and curved-ray SWT in 3D media. We use finite-difference methods to compute the synthetic data. For the 2D example, the synthetic waveform data are generated using a 2D-finite difference (FD) code (Qin et al., 2020). For the 3D examples, we use SOFI3D software (described in Bohlen, 2002) to generate synthetic data. It is an FD modelling program based on the FD approach described by Virieux (1986) and Levander (1988) with some extensions. It can consider viscoelastic wave propagation effects such as attenuation and dispersion, employ higher order FD operators, apply perfectly matched layer (PML) boundary conditions at the edges of the model, and it works in message passing interface (MPI) parallel environment which reduces the running time of the simulations.

To avoid numerical dispersion during the simulations, the spatial grid point distance in all three dimensions (dh) should be defined such that the wavefield can be well-sampled spatially. The maximum dh can be computed as:

$$dh \leq \frac{\lambda_{\min}}{n}, \qquad 2.2$$

where $\lambda_{\min}$ is the minimum wavelength and n represents the number of grid points per minimum wavelength. As shown in Table 2.1, the factor n varies for different orders of (Taylor) finite-difference operator.

Table 2.1. The number of grid points per minimum wavelength for a Taylor finite-difference operator (SOFI3D software described in Bohlen, 2002).

Finite-difference order	2^{nd}	4^{th}	6^{th}	8^{th}	10^{th}
n	12	8	7	6	5

Using higher-order of the finite-difference operator increases the computational effort but allows larger grid size to be used. We use a 4^{th} order finite-difference operator in our simulations. Therefore, based on the information in Table 2.1, at least 8 grid-points should be defined in one shortest wavelength to compute the elastic wave propagation without numerical dispersion. The timestep of the simulation should be chosen less than the needed time for the wave to travel between two neighbouring grid points to satisfy Nyquist's criterion and results in a stable simulation. The maximum timestep (dt) can be computed from:

$$dt \leq \frac{dh}{r_{\max} \cdot VP_{\max}}, \tag{2.3}$$

where $r_{\max}$ represents the Courant-Friedrichs-Lewy (CFL) number and $VP_{\max}$ is the maximum VP in the model. The values of $r_{\max}$ for a Taylor finite-difference operator can be obtained from Table 2.2 (Bohlen and Wittkamp, 2016).

Table 2.2. The r_{max} values of a Taylor FD operator as a function of spatial and temporal orders.

Spatial order	Temporal order		
	2	3	4
2	0.577	0.494	0.384
4	0.494	0.424	0.329
6	0.464	0.398	0.309
8	0.448	0.384	0.299
10	0.438	0.375	0.292

We use 0.329 as the value of r_{max} in our calculations. In the simulation processes, we employ absorbing boundaries at each side of the model (except at the surface) with a size of 30 grids.

2.3.1 Step Model

The Step Model contains a vertical uplift in the bottom-right part of the model (Figure 2.1) which can be related to a faulty formation as a real-world example. The geophysical parameters of the Step Model are reported in Table 2.3

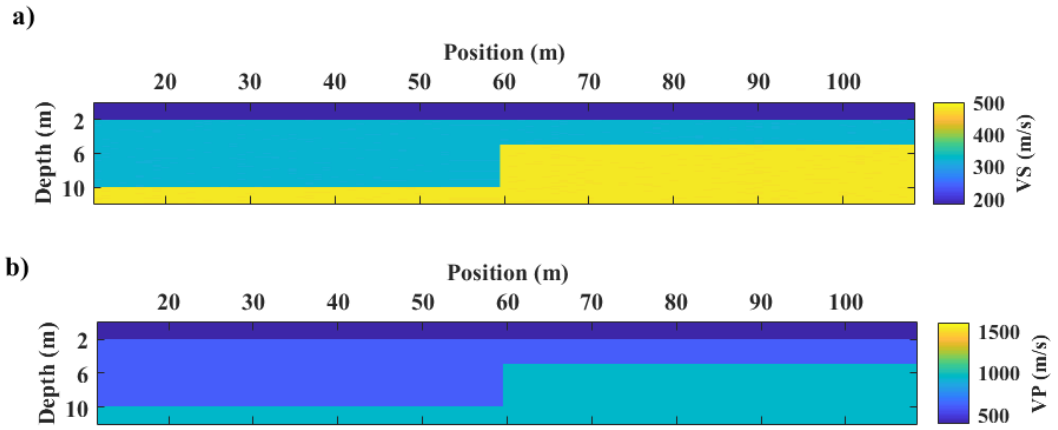

Figure 2.1. Velocity distribution of the Step Model. a) VS, b) VP.

Table 2.3. Geophysical parameters of the Step Model.

Layer	VS (m/s)	VP (m/s)	h (m)	ρ (g/cm^3)
1	180	310	2	2
2	320	590	3-8	2.1
Half-space	480	950	-	2.2

The synthetic data for the Step Model were available and had been generated for other purposes, but we use them in this thesis to compare the results of the joint inversion of BWT and SWT with the individual inversions. The simulation parameters are presented in Table 2.4.

Table 2.4. The simulation parameters of the Step Model

Number of receivers	101 (with 1 m spacing)
Source	Ricker wavelet with dominant frequency of 20 Hz
Number of sources	25 (with 5 m spacing)
Sampling rate (ms)	0.1
Recording time window (s)	2
dh (m)	0.2
Maximum *dh* from Equation 2.2 (m)	0.56
dt (ms)	0.1
Maximum *dt* from Equation 2.3 (ms)	0.64

Figure 2.2 depicts an example of the simulated data, all the estimated DCs, and the picked first-arrival times. The number of unique pairs (i.e., maximum number of DCs using a two-station processing method) out of 101 receivers would be 5050. The number of extracted DCs from the raw data is 664. The DCs and first arrivals have been used in Section 5.1.

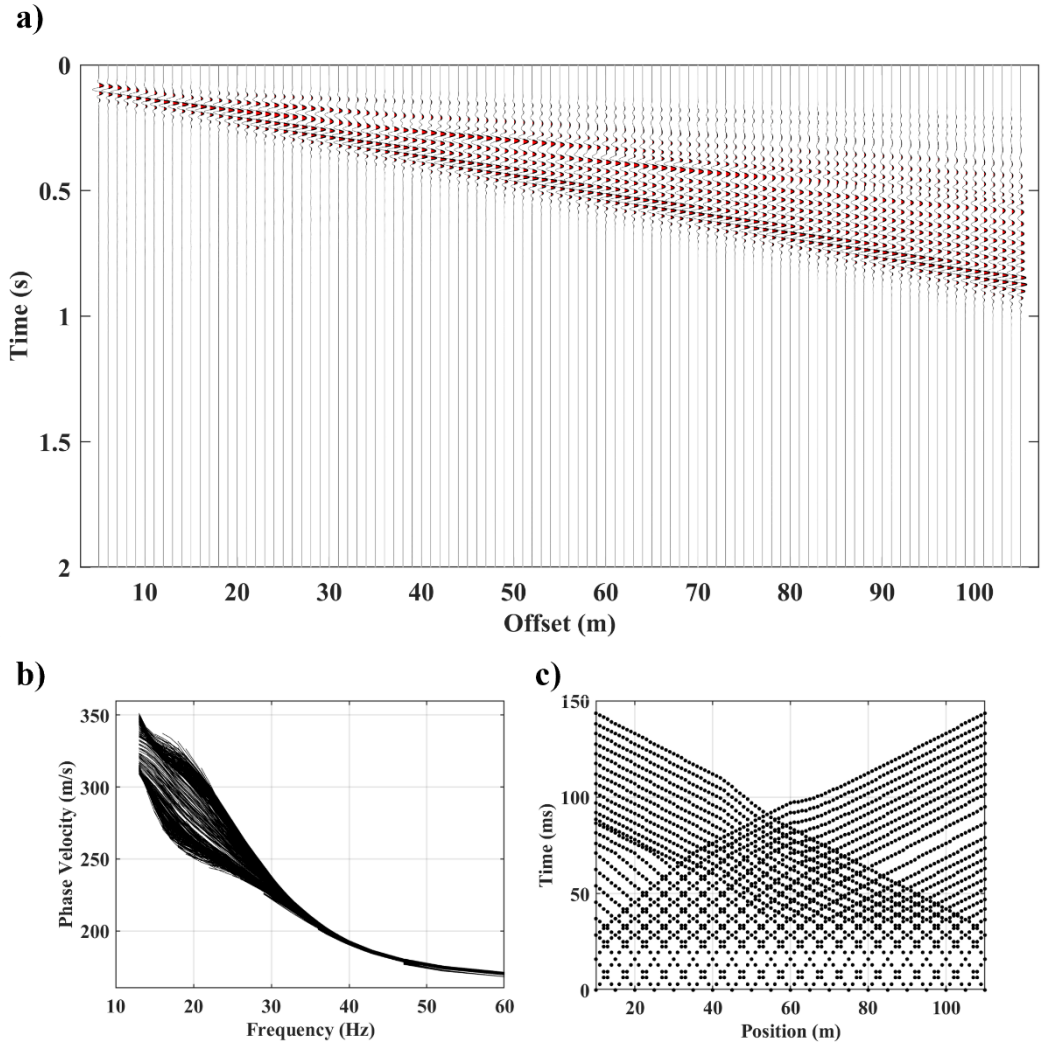

Figure 2.2. a) An example of the simulated data. b) The extracted DCs, c) the picked first-arrival times.

2.3.2 Blocky Model

This model is designed to study the performance of straight-ray and curved-ray SWT in an environment with high lateral velocity variation. The model corresponds to a sandy medium with a vertical velocity gradient in which two blocks of low and high velocity are embedded as shown in Figure 2.3. Each block is a cube of 4 m on a side (Figure 2.3b-d). One block has a VS value equal to almost half of its surrounding layers (Figure 2.3b), while the velocity of the other block is approximately twice as the background VS (Figure 2.3d). The geophysical parameters of the Blocky Model are reported in Table 2.5.

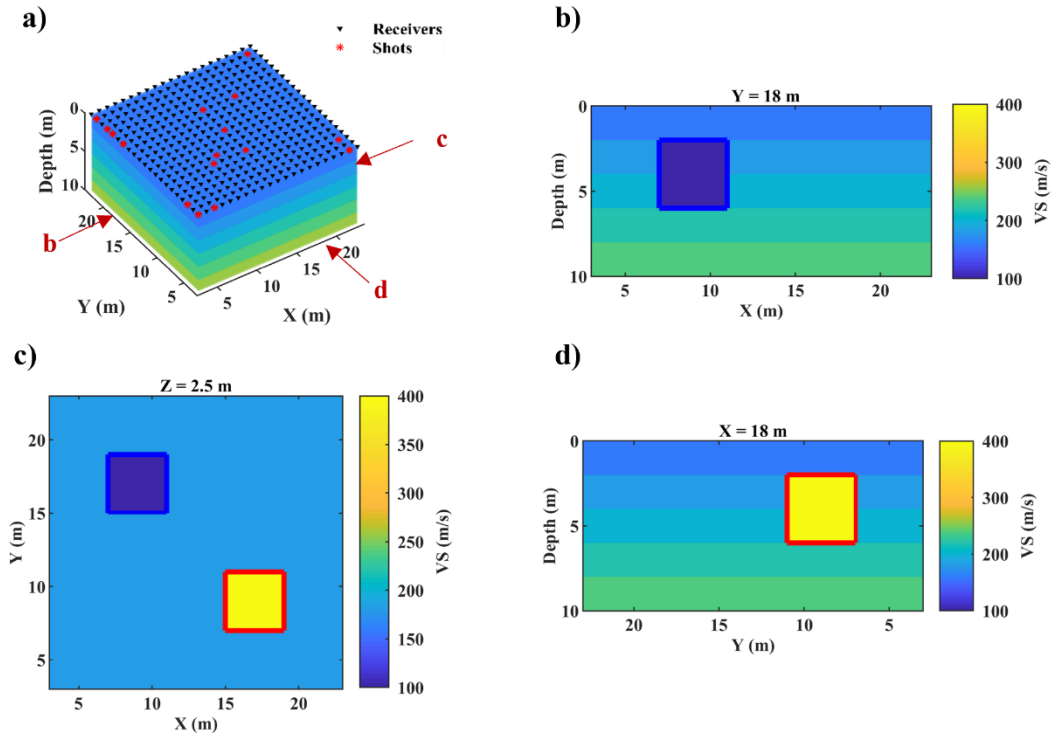

Figure 2.3. a) 3D view of the true VS model together with the acquisition layout. The red arrows represent the location of 2D slices in subplots (b-d). b) Vertical slice at Y=18m, shown as arrow b in subfigure (a). c) Horizontal slice at 2.5 m depth, arrow c in subplots (a). d) Vertical slice at X=18m, corresponding to the arrow d in subfigure (a). The boundaries of the low- and high-velocity anomalies are superimposed in blue and red, respectively.

Table 2.5. Geophysical parameters of the Blocky Model

Layer	VS (m/s)	h (m)	VP	ρ (kg/m^3)
1	160	2	320	2000
2	180	2	360	2000
3	200	2	400	2000
4	220	2	440	2000
5	240	2	480	2000
Low-velocity block	100	4	200	2000
High-velocity block	400	4	800	2000

We spread the receivers in a regular grid with 1 m spacing in an area of 20 m by 20 m. We have chosen 16 sources to generate the raw data. We have optimized the shot positions and picked the 11 shots that provided the greatest number of unique inter-stational pairs. Since most of the chosen 11 shots are located near to the edges of the model, we have added 5 shots at the centre of the model to ensure the high coverage of broadband DCs in the areas of the target blocks. Figure 2.4 shows the obtained theoretical DC coverage by the selected shots (assuming straight ray paths between each receiver pair), and the simulation parameters of the Blocky Model are reported in Table 2.6.

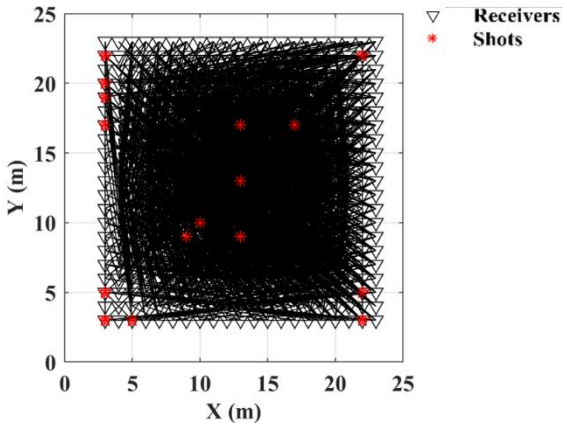

Figure 2.4. The theoretical DC coverage for the selected shots.

Table 2.6. Simulation parameters to generate the synthetic data of the Blocky Model

Number of receivers	441 (regular grid of 1 m spacing)
Source	Ricker wavelet with dominant frequency of 40 Hz
Number of sources	16
Sampling rate (ms)	0.05
Recording time window (s)	0.5
dh (m)	0.1
Maximum *dh* from Equation 2.2 (m)	0.156
dt (ms)	0.010
Maximum *dt* from Equation 2.3 (ms)	0.041

Figure 2.5 displays an example of the recorded data for the shot located at (3 m, 3 m). Two examples of the computed frequency-phase velocity spectra in Figure 2.6.

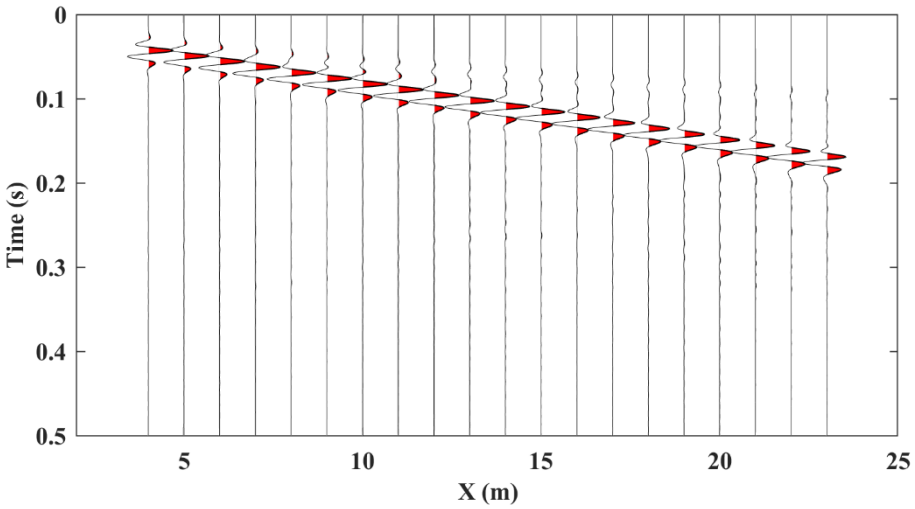

Figure 2.5. The recordings for the shot located at x,y=3 m and the receivers with y=3 m.

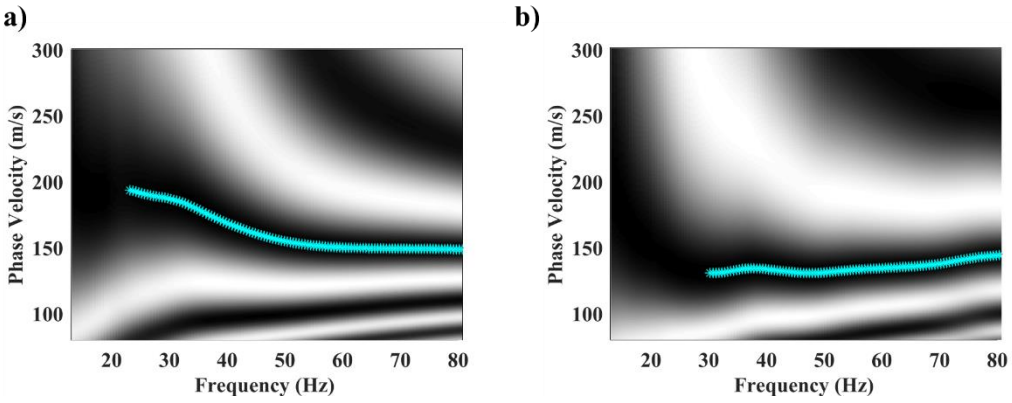

Figure 2.6. a) The spectrum crossing the block of high-velocity anomaly. b) The spectrum and the fundamental DC for an interstation path crossing the block of low-velocity anomaly. The estimated DCs are shown in cyan.

We depict all 921 extracted DCs for the blocky model and their corresponding inter-station coverage in Figure 2.7. We use the estimated DCs in Section 4.1 to study the performance of straight- and curved-ray SWT.

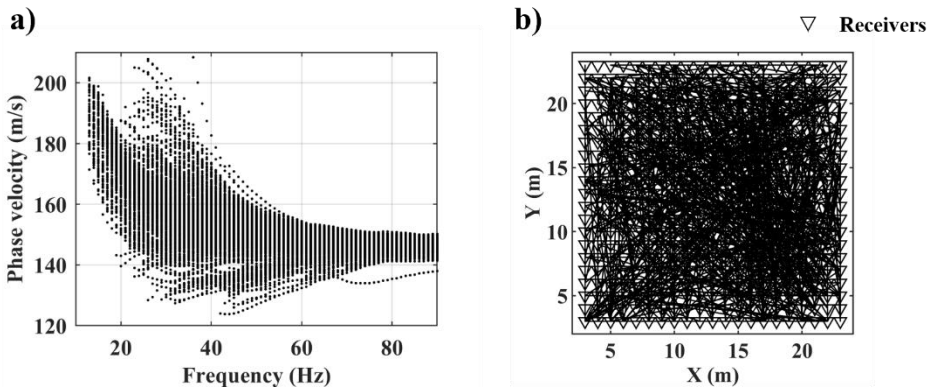

Figure 2.7. a) The estimated DCs for the Blocky Model, b) the actual DC coverage.

2.3.3 Sand Bar model

The Sand Bar Model was inspired by a field site in Pijnacker, the Netherlands, and serves to allow for a pre-study for the data acquisition in the Pijnacker field. We compute the data from this model to evaluate the performance of SWT on a synthetic dataset before acquiring the field data. The Pijnacker field contains unconsolidated clays, and possibly peat, and sand-filled channels in some locations. Therefore, we design the Sand Bar model to simulate an environment where a sand channel (high-velocity anomaly) is buried in unconsolidated clays. To add some complexity to the model, we design a curved sand bar embedded in a low velocity background to assess the ability of SWT to resolve the target geometry and properties. Figure 2.8 shows the true VS model. The receiver and shot positions are superimposed in Figure 2.8a, and the curved shape of the Sand Bar can be seen clearly in Figure 2.8b. We select the seismic properties of the Sand Bar Model (Table 2.7) based on information coming from the boreholes available at the Pijnacker site.

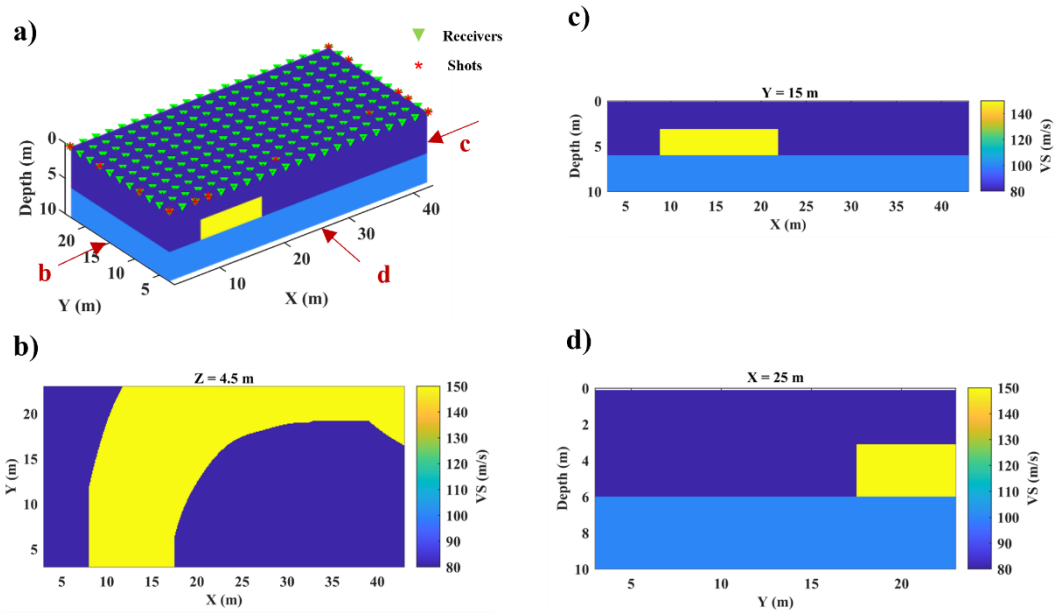

Figure 2.8. a) 3D view of the true VS model together with the acquisition layout. The red arrows represent the location of 2D slices in subfigures (b-d). b) Horizontal slice at 2.5 m depth, corresponding to the arrow c in subfigure (a). c) Vertical slice at Y=18m, corresponding to the arrow b in subfigure (a). d) Vertical slice at X=18m, arrow d in subfigure (a).

Table 2.7. Geophysical parameters of the Sand Bar Model

Material	VS (m/s)	VP (m/s)	h (m)	ρ (kg/m^3)
Clay - 1st layer	80	1700	3-6	1750
Sand	150	2000	3	1900
Clay - lower half space	100	1850	-	1950

We set the VS value of the first layer of clay to 80 m/s based on a previous study (Bharadwaj et al., 2017) of a clay field near to our field (Pijnacker). We assume that the second layer of clay is slightly consolidated and therefore, increase its VS to 100 m/s. We set a VS value of 150 m/s for the sand layer. We assume that the medium is saturated and hence, all the VP values are more than 1500 m/s.

We show the positions of source and receivers in Figure 2.8a. We optimise the shot positions and select 13 sources that provide the highest DC coverage to generate the synthetic data. Figure 2.9 shows the theoretical DC coverage by these shots. The simulation parameters of the Sand Bar model are summarised in Table 2.8.

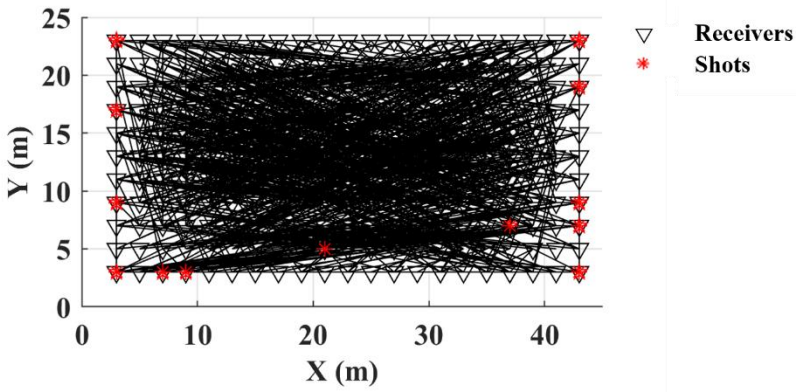

Figure 2.9. The theoretical DC coverage for the optimised shot positions.

Table 2.8. The simulation parameters of the Sand Bar Model.

Number of receivers	231 (regular grid of 2 m spacing)
Source type	Ricker wavelet with dominant frequency of 40 Hz
Number of sources	13
Sampling rate (ms)	0.05
Recording time window (s)	1
dh (m)	0.1
Maximum *dh* from Equation 2.2 (m)	0.125
dt (ms)	0.010
Maximum *dt* from Equation 2.3 (ms)	0.016

Figure 2.10 displays an example of the recorded signals from the shot located at (3 m, 3 m). Figure 2.11 shows two examples of the computed frequency-phase velocity spectra. The straight-line between the receiver pair in the first example

(Figure 2.11a) crosses the sand layer whereas this is not the case for the second example (Figure 2.11b).

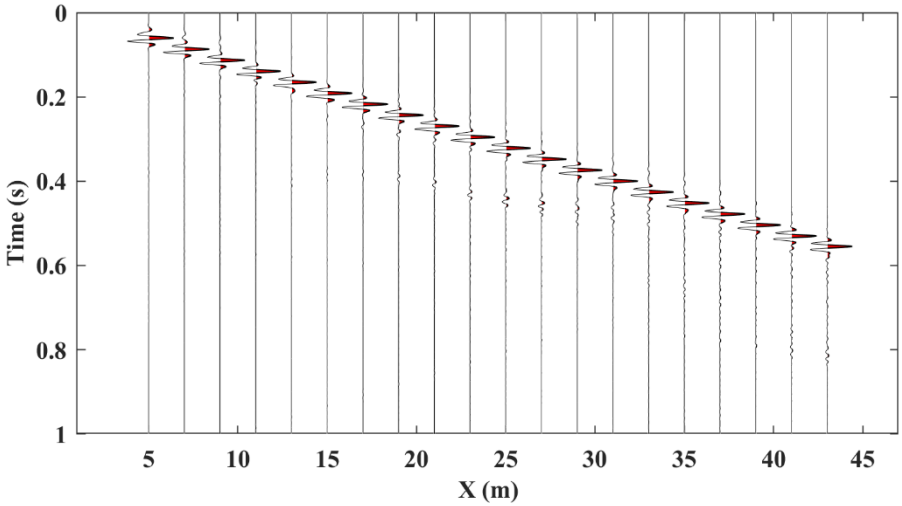

Figure 2.10. An example of recordings for the inline receivers with the shot at (3,3).

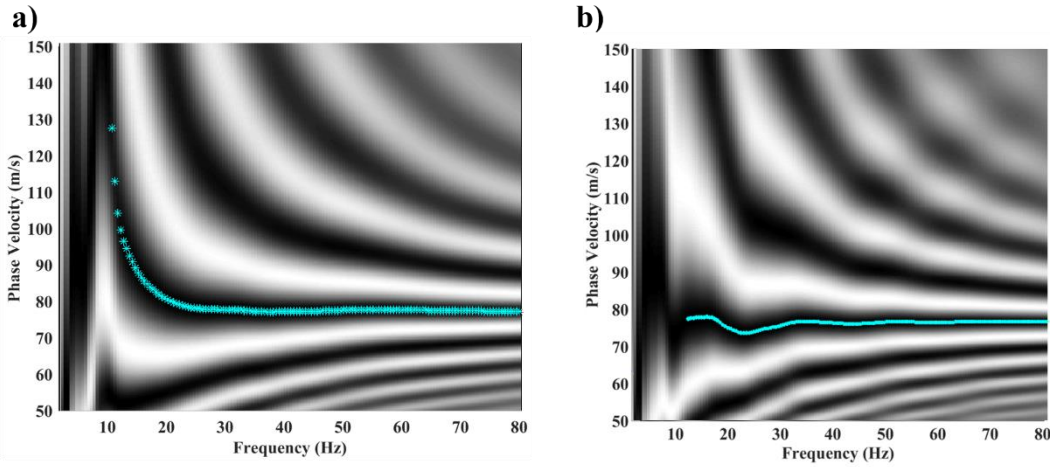

Figure 2.11. a) The spectrum for an inter-station path crossing the sand anomaly. The receivers in the pair are located at (11 m, 9 m) and (17 m, 3 m). b) The spectrum where the inter-station path does not cross the sand. The locations of the receiver couple are at (33 m, 11 m) and (43 m, 9 m). The estimated DCs are displayed in cyan.

Figure 2.12 shows all 1207 retrieved DCs for the Sand Bar model and the actual DC coverage. We use the extracted DCs in Section 4.2 as inputs of SWT inversion.

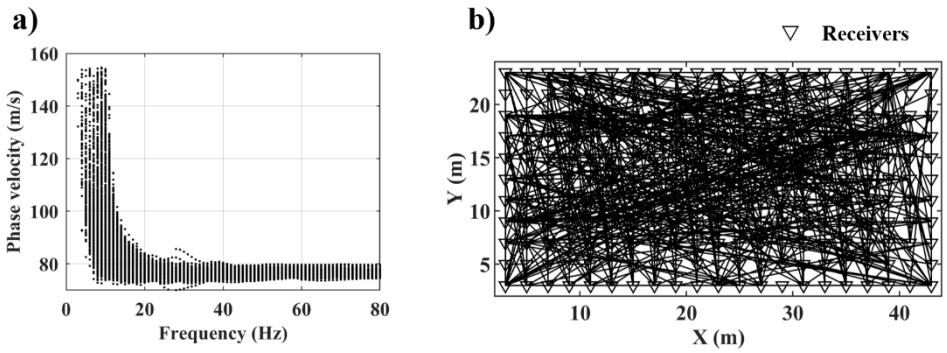

Figure 2.12. a) The estimated DCs. b) The actual DC coverage.

2.4 Field datasets

We use two field datasets from Pijnacker and CNR (Consiglio Nazionale delle Ricerche) fields. The target in the Pijnacker field is a sand layer embedded in unconsolidated clay and peat materials. The low velocity materials, particularly below the higher velocity target, can be challenging for the detection of the sand layer. In case of the CNR field, the target is an artificial sand body surrounded by silty gravel. The sharp lateral variation between the artificial sand body and the background medium requires high resolution to be properly depicted. For each field, the data have been acquired in a 2D and a 3D scheme.

2.4.1 Pijnacker field

The field is located near Pijnacker, South Holland, Netherlands (Figure 2.13). The field consists of unconsolidated material and the publicly available (www.dinoloket.nl) well data (Figure 2.13c) near to the field suggest that the field mainly contains clay, together with peat and possibly sand in some locations.

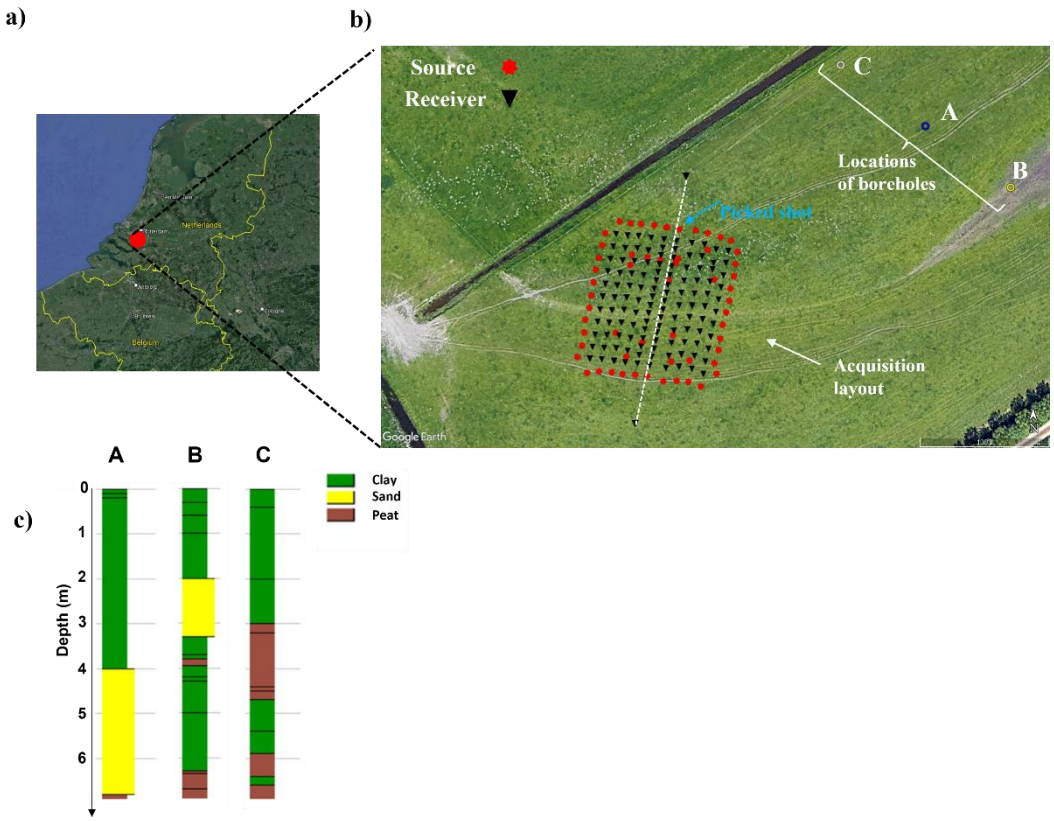

Figure 2.13. a) Aerial view of Netherlands with the red circle showing the location of the field. b) The acquisition layout. The white dashed line represents the 2D seismic line. c) The available borehole data near to the field. The location of each well is marked in subfigure (b).

The data acquisition was carried out adopting 2D and 3D layouts. In both cases, the source was a vibrator that emitted a linear sweep signal from 2 to 100 Hz for 5 seconds at a force level of 1150 N, and the signals were recorded by 120 vertical 4.5 Hz geophones. The acquisition parameters in 2D and 3D are reported in Table 2.9.

Table 2.9. The acquisition parameters between the 2D and 3D layouts.

Receivers		120 vertical 4.5 Hz geophones
Receiver spacing	2D	0.5
	3D	2-3 m
Source		Vibrator
Number of sources	2D	15
	3D	59
Source spacing (m)	2D	5
	3D	various
Sampling rate (ms)		0.125
Recording time window (s)		2

Figure 2.14 displays an example of the recordings, the extracted DCs from the raw data (Figure 2.14b) and the picked the first-arrival times (Figure 2.14c) for the 2D layout. The theoretical number of receiver pairs (possible DCs) for 120 receivers is 7140. But the number of estimated DCs is 175, which shows that the quality of the data was poor. These DCs and first arrivals have been used for the joint inversion of SWT and BWT in Section 5.2.

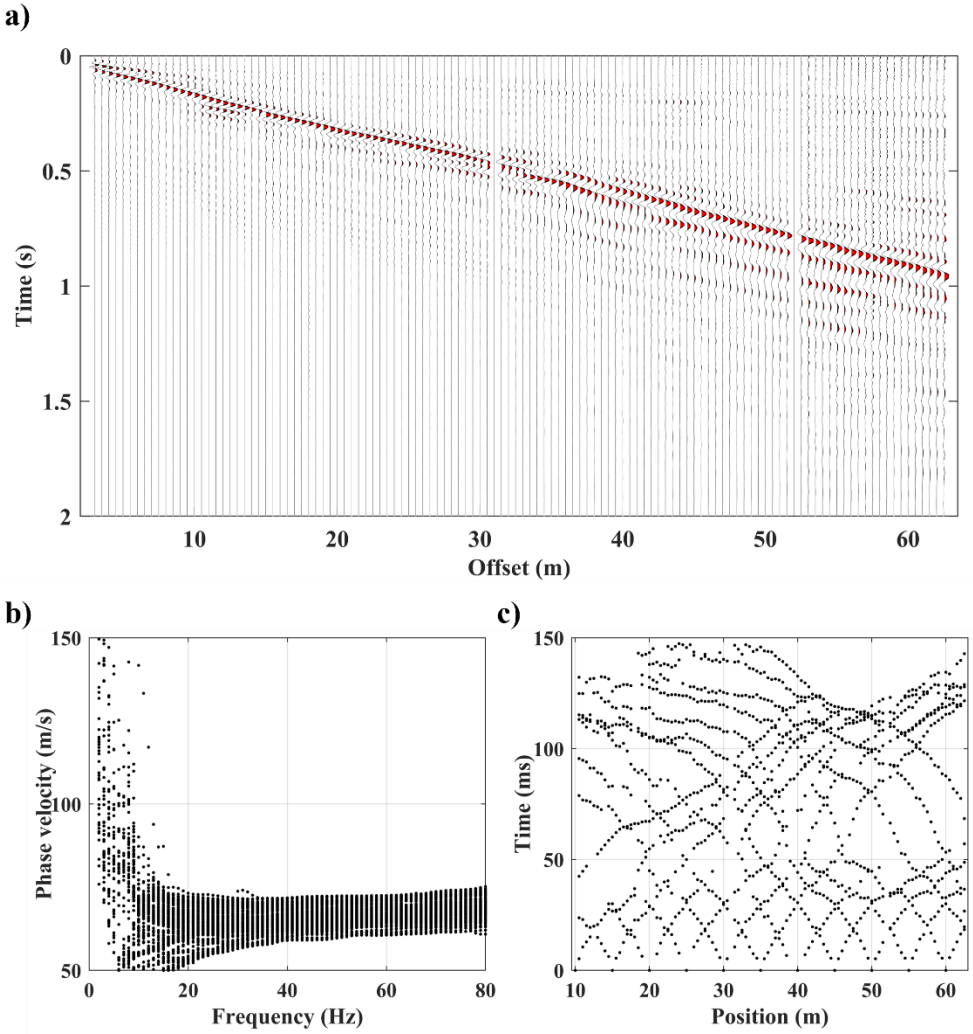

Figure 2.14. a) An example of recorded raw data. b) The estimated DCs, b) picked first-arrival times.

In the 3D acquisition layout (Figure 2.13b), the geophones are distributed in an area of 27 m×30 m as a regular grid with 3 m spacing along east-west direction. The geophone spacing along north-south direction is equal to 2 m in the central part of the array (close to the white dashed line in Figure 2.13b), and 3 m in the rest of the grids. The signals were recorded from 59 shot locations. Since the field consists of unconsolidated materials and the vibrator source and its carrier are relatively heavy, we have tried to minimise the number shot positions inside the acquisition area to prevent the change of subsurface properties caused by moving the source. Hence, the positions of 44 shots are located outside the array area, at 3 m distance from each geophone located at the outer boundary of the acquisition area. To ensure having broadband DCs, we select 15 shot positions inside the acquisition area. The

shot positions that are either at the edge of the array area or at the geophone positions are not selected. In Figure 2.15, we show the obtained theoretical DC coverage by the 15 shots inside the acquisition area (in Figure 2.15a) and by all 59 shots (in Figure 2.15b).

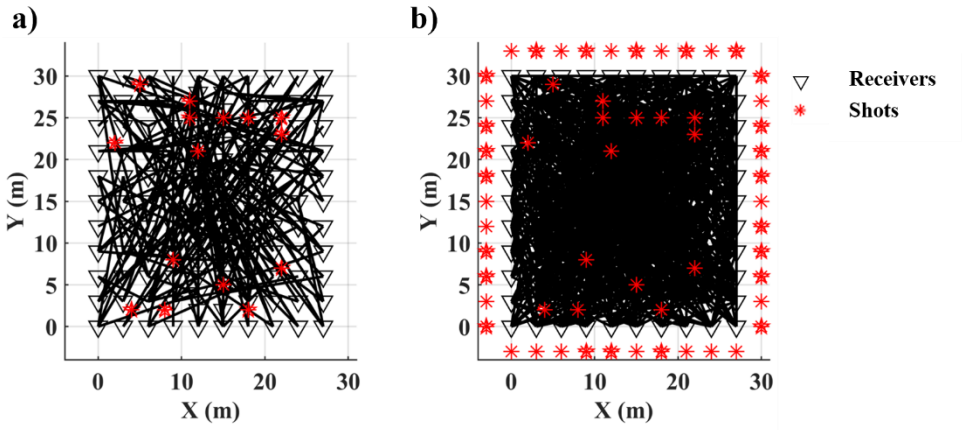

Figure 2.15. The theoretical DC coverage for: a) the shots inside the array area, b) all shots.

Figure 2.16 shows an example of recorded signals and the estimated DCs. All the 972 estimated DCs and the actual DC coverage are displayed in Figure 2.17. In Section 4.3, the DCs have been used as the input of SWT.

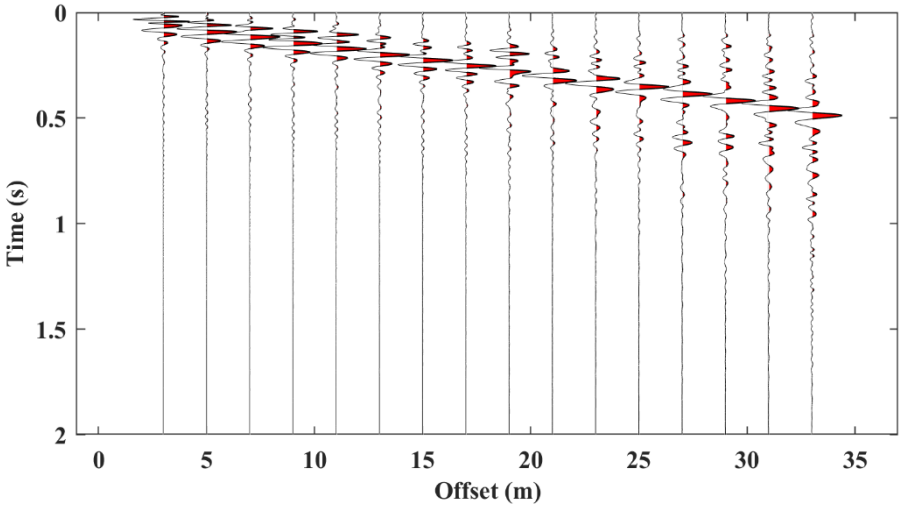

Figure 2.16. Recordings for the shot which is marked by a blue arrow in Figure 2.13b and the inline receivers with the shot.

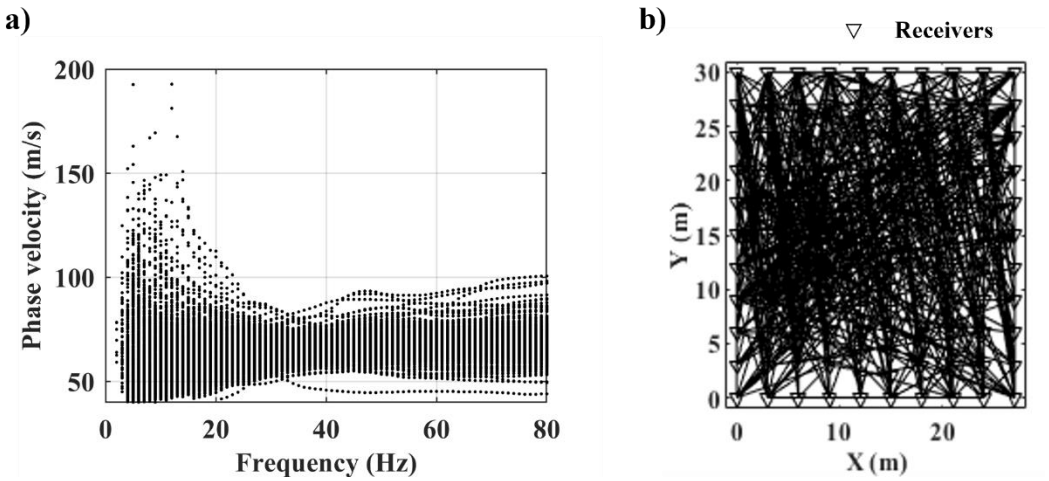

Figure 2.17. a) All 972 extracted DCs, b) the inter-station path coverage of the estimated DCs.

2.4.2 CNR field

The site is located at the CNR headquarter in Turin, Italy (Figure 2.18). The site consists of stiff sand and silty gravel formations surrounding an artificial loose sand body. The maximum depth of the sand body is 2.5 m, and it occupies an area of 5 m by 5 m at the surface. The extent of the sand body reduces with depth and reaches to a minimum 3 m by 3 m. As it can be seen in Figure 2.18b, the field is located next to a street, which might cause to have some noise in the recorded data.

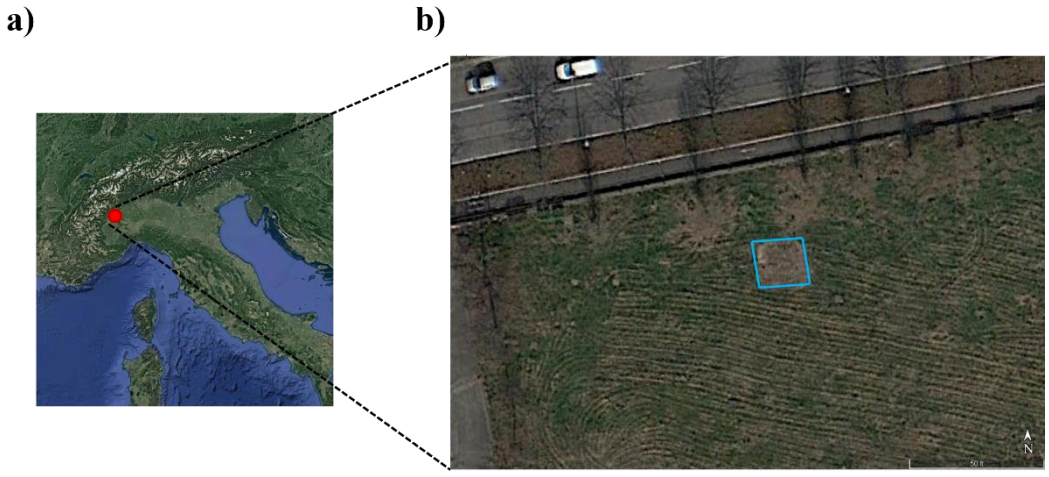

Figure 2.18. Aerial view of the CNR acquisition site. a) The site's location is shown in red circle. b) A closer view of the CNR site with the boundaries of the loose sand body highlighted in blue.

The field data have been acquired in 2D and 3D layouts. The acquisition parameters are reported in Table 2.10.

Table 2.10. The acquisition parameters of 2D and 3D layouts for the CNR field.

Receivers		72 vertical 4.5 Hz geophones
Receiver spacing (m)	2D	0.3
	3D	0.5-2.5
Source		8 kg hammer
Number of sources	2D	15
	3D	83
Sampling rate (ms)		0.512
Recording time window (s)		2.1

The sand body is in the centre of the 2D line, and the data have been acquired from 11 shot positions. Figure 2.19 depicts the 2D acquisition scheme and an example of the recorded signal.

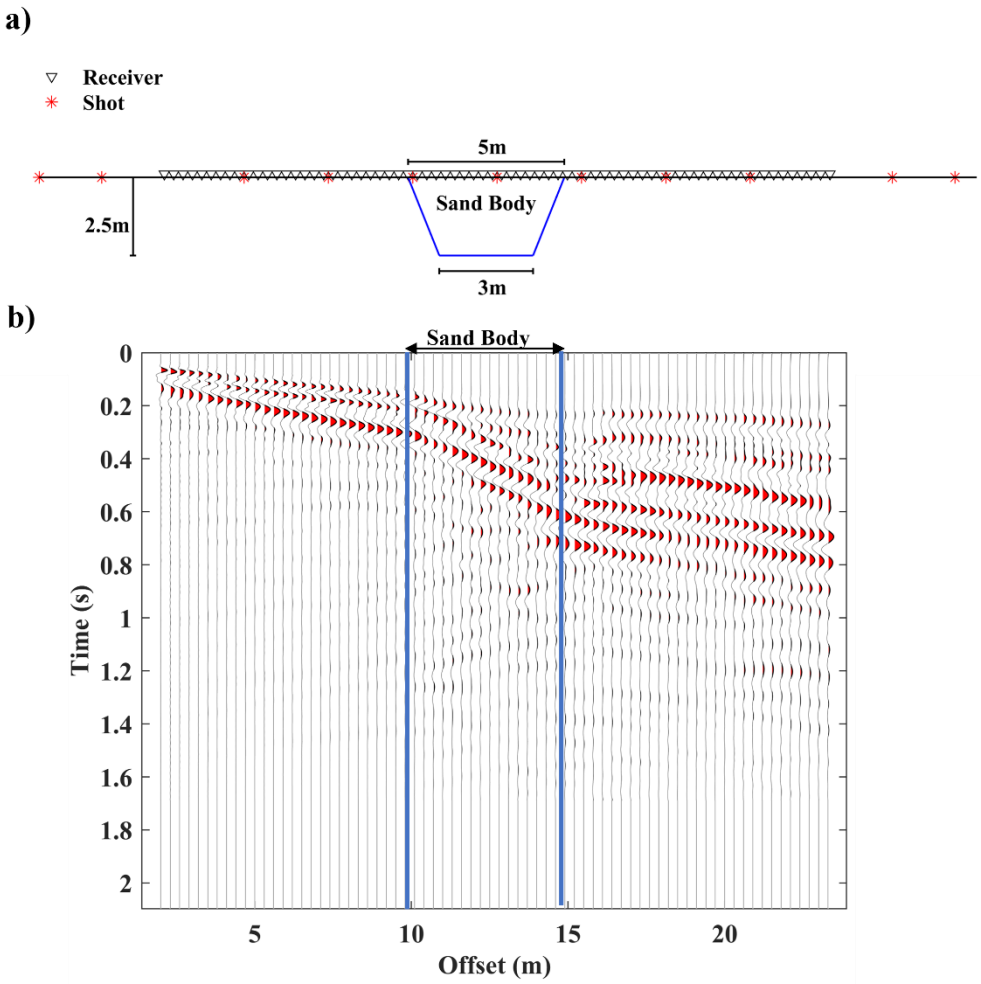

Figure 2.19. a) The acquisition outline of the 2D seismic line of the CNR field. b) An example of the recorded signal.

In Figure 2.20, we show two examples of the computed frequency-phase velocity spectra, all the extracted DCs, and the picked first-arrival times.

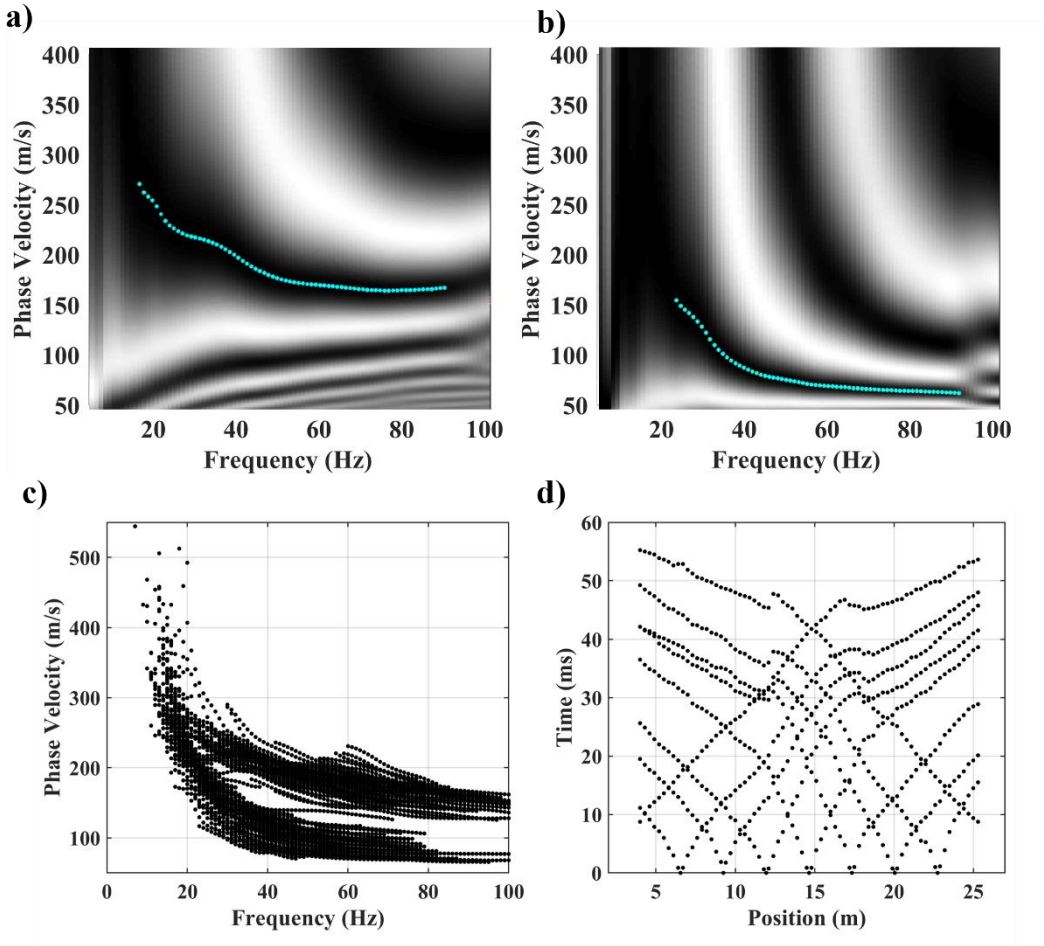

Figure 2.20. The processed data for the CNR 2D line. a) The frequency-phase velocity spectrum where both receivers (2nd and 14th) are located outside the loose sand body. The estimated DC is shown in cyan. b) An example of the computed spectrum between the 28th and 42nd receivers that are both located inside the sand body. c) All estimated DCs. d) The picked first-arrival times.

Figure 2.20 shows that the phase velocity values of the estimated DC is much higher when both receivers are outside the loose sand body (Figure 2.20a) than inside it (Figure 2.20b). This difference can also be observed in Figure 2.20c where the DCs form two relatively distinct groups.

The number of unique pairs out of 72 receivers is 2556, but only 140 DCs have been extracted from the raw data. The low quality of the data could be due to the noise and the sharp lateral velocity variation which could produce 'breaks' in the computed frequency-phase velocity spectra. The extracted DCs (Figure 2.20c) and first arrivals (Figure 2.20d) are used in Section 5.3.

The 3D acquisition scheme (Figure 2.21a) replicated at small scale a classical 3D seismic acquisition and consists of 4 lines of receivers orthogonal to 6 lines of shots. The receiver lines are 2.5 m apart. Each line includes 18 vertical geophones with 0.5 m spacing. Figure 2.21b displays an example of the recorded signal. Figure 2.22 shows all 315 estimated DCs from the raw data as well as the picked first-arrival times.

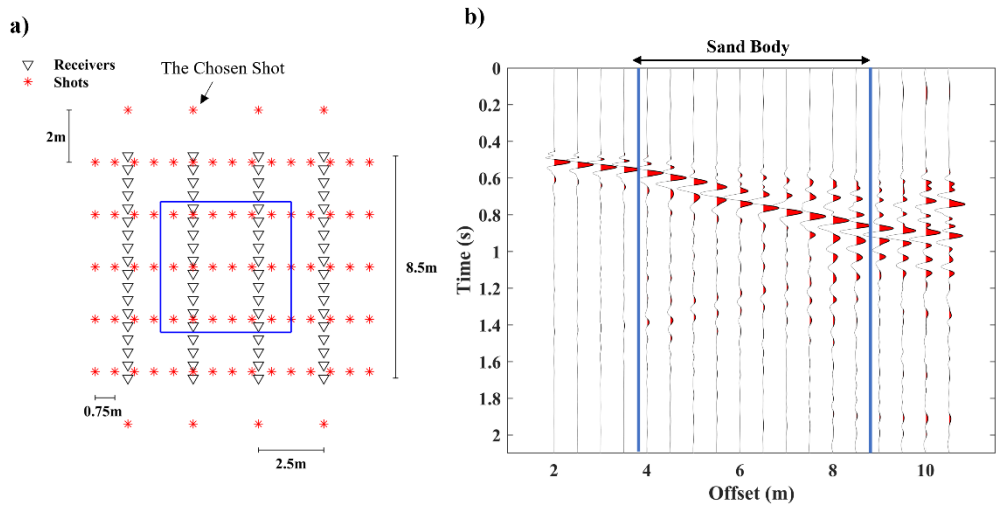

Figure 2.21. a) The 3D acquisition outline with the extent of the sand body at the surface is superimposed in blue. b) An example of recordings for the shot that is marked by an arrow in subfigure (a) and the inline receivers with the chosen shot.

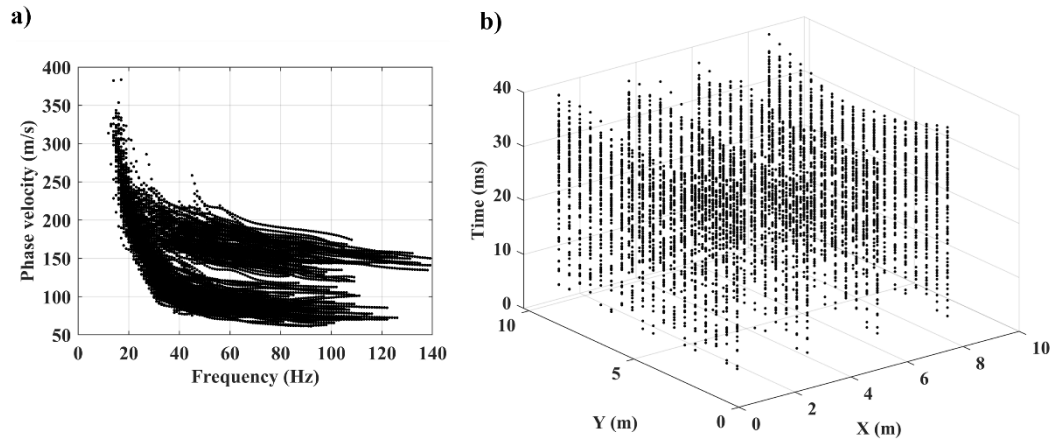

Figure 2.22. The processed 3D data for the CNR field. a) DCs, b) first-arrival times.

Like the 2D example (Figure 2.20c), we can see in Figure 2.22a that the extracted DCs from the 3D dataset have also two ranges of phase velocities where

the lower range can be assigned to the ones crossing the loose sand body. In Figure 2.23, we depict the actual coverage for the estimated DCs.

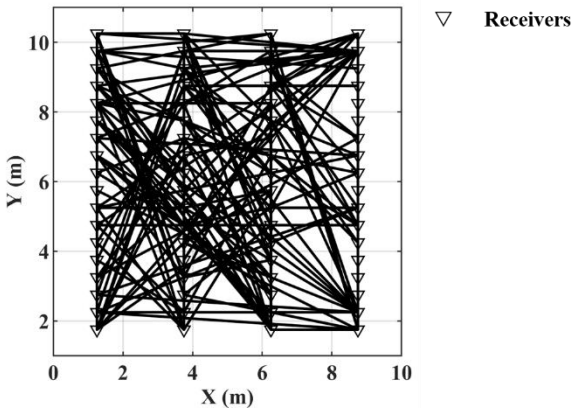

Figure 2.23. The obtained actual DC coverage.

The DCs have been used in Section 4.4 as inputs of SWT inversion. Moreover, the DCs and first-arrival data (Figure 2.22) have been used in Section 5.4 for the joint inversion of SWT and BWT in 3D.

2.5 Conclusion

We described the synthetic and field examples that are used in the thesis. We explained the employed procedure to optimise the source positions in a SWT study. We also explained the procedure to extract DCs from the raw data using a two-station processing method. We used a MATLAB code which estimated the DCs automatically and rejected the low-quality DCs.

For the synthetic examples, we described the simulation parameters and how the model can represent a real-world example. We also explained the geological information and the specific challenges for each field example and listed the used acquisition parameters. We also showed examples of the raw data, frequency-phase velocity spectra, and the estimated DCs and displayed the obtained DC coverage for the 3D examples.

Chapter 3

Method

In this Chapter, the employed inversion algorithms are described. We first explain the applied inversion algorithm for SWT to obtain subsurface VS models in 2D and 3D media. In 3D media, the paths between each receiver pair can be fixed as straight lines, i.e., straight-ray SWT. Alternatively, in curved-ray SWT, a ray tracing method is used to compute the fastest path between every receiver pair at each frequency. In this Chapter, we describe the differences between straight-ray and curved-ray SWT approaches.

We then propose an algorithm for the joint inversion of SWT and BWT in which Poisson's ratio is used as the physical constraint between SWT and BWT. We also provide details about the employed procedure to integrate SWT and BWT methods.

3.1 SWT algorithm

Our SWT inversion scheme is an evolution of the proposed SWT algorithm and the implemented MATLAB codes by Boiero (2009) which had been applied in seismological studies. We have implemented the codes in Python and made several modifications and improvement compared to the original MATLAB code. We have added curved-ray SWT to our code by means of ray tracing at each frequency. We have reduced the running time of the inversion process by parallelisation of the major time-consuming functions of the code, which are the computation of the sensitivity matrix and the frequency dependent path-average slowness. We have modified the computation of inter-station paths, avoiding the computation of great-circle path for each receiver pair, which is unnecessary for near-surface studies. We have also used an open access Python library (*disba*) for the forward modelling of SW.

In our SWT scheme, we estimate the DCs from the raw data using a two-station method and then invert them to build subsurface VS models without inverting phase velocity maps. We define a misfit function (Φ) and minimise it iteratively. To

minimise the misfit function, we start the inversion from an initial model and update iteratively. We define Φ as:

$$\Phi = \left[\left(\mathbf{d}_{\exp} - \mathbf{fw}\left(\mathbf{m}\right) \right)^T \mathbf{C}_{\exp}^{-1} \left(\mathbf{d}_{\exp} - \mathbf{fw}\left(\mathbf{m}\right) \right) \right] + \left[\left(\mathbf{Rm} \right)^T \mathbf{C}_{\mathbf{R}}^{-1} \left(\mathbf{Rm} \right) \right], \qquad \mathbf{3.1}$$

where $\mathbf{d}_{\exp}$ shows the vector of experimental data (DCs), $\mathbf{fw}\left(\mathbf{m}\right)$ is the computed forward response of the model ($\mathbf{m}$), the data covariance matrix is represented as $\mathbf{C}_{\exp}$, $\mathbf{R}$ is the spatial regularization matrix and $\mathbf{C}_R$ is the corresponding covariance matrix.

Figure 3.1 shows a schematic representation of the employed SWT inversion algorithm. We explain each step in the following paragraphs.

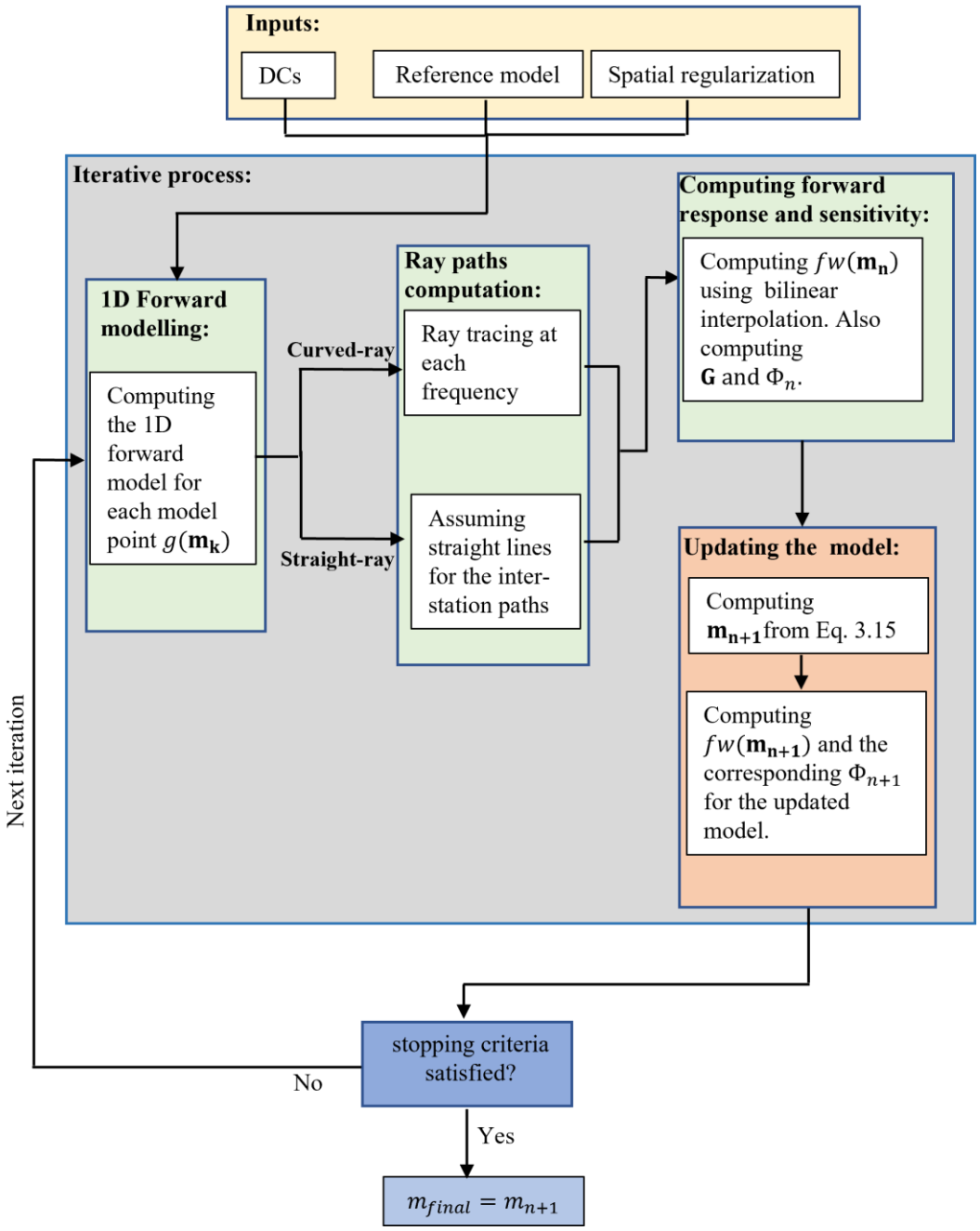

Figure 3.1. Scheme of the inversion algorithm for straight-ray and curved-ray SWT.

3.1.1 Inputs

DCs

DCs are the experimental input data for SWT inversion. In Section 2.2, we explained the applied methodology to estimate DCs and their corresponding

uncertainties from the raw data. We use an automatic two-station code (Papadopoulou, 2021) to estimate DCs. Each DC is extracted between using the recorded seismic signal between a receiver pair ($R_1 - R_2$). For the frequency band of the generic ith estimated DC, we put the corresponding phase velocity values into a vector ($\mathbf{V_i}$). Then, the input data for the inversion would be a vector ($\mathbf{V}$) containing the phase velocities of all DCs as:

$$\mathbf{V} = \left[\mathbf{V}_1;\ \cdots;\ \mathbf{V_i};\ \cdots;\ \mathbf{V}_{n_{DC}} \right]. \qquad \textbf{3.2}$$

where n_{DC} is the total number of estimated DCs. For the generic jth element of the vector of phase velocities (V_j), we approximated the uncertainties of phase velocity data as (Passeri, 2019):

$$\sigma_{V_j} = \left[0.2822\ \mathrm{e}^{-0.1819 f_j} + 0.0226\ e^{0.0077 f_j} \right] * V_j . \qquad \textbf{3.3}$$

where σ_{V_j} is the standard deviation of V_j, and f_j is the corresponding frequency. The vector of standard deviation of all phase velocity data (σ_V) is defined as:

$$\boldsymbol{\sigma}_{\mathbf{V}} = \left[\sigma_{V_1};\ \cdots;\ \sigma_{V_j};\ \cdots;\ \sigma_{V_{nv}} \right]. \qquad \textbf{3.4}$$

where nv shows the total number of elements of the phase velocity vector ($\mathbf{V}$). Then, the uncertainty of the experimental phase velocity data $\mathbf{C}_{\mathrm{exp}}$ is defined as:

$$\mathbf{C}_{\mathrm{exp}} = diag\left(\boldsymbol{\sigma}_{\mathbf{V}}{}^2 \right). \qquad \textbf{3.5}$$

Reference model

We discretize the subsurface to *K* model points where each one is a 1D vertical stack of *N* layers. The schematic discretization of the subsurface is depicted in Figure 3.2.

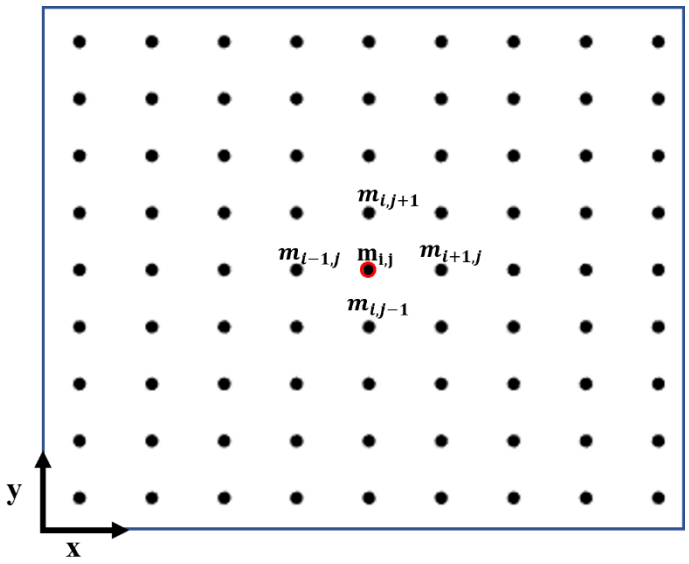

Figure 3.2. Plan view of the model discretisation scheme in 3D. Each point represents a model point which is a stack of vertical layers. Each layer has VS, ν, ρ, and h values. The k^{th} model point is shown in red.

For each layer of the shown model points in Figure 3.2, we need to define the following properties: VS, ν, ρ, and *h*. Since SW are more sensitive to VS than to ν and ρ (Xia et al., 1999), we assume that ν, ρ are available as a priori information and we do not change the defined initial values of ν and ρ during the inversion process. We define the vector of unknown model parameters (For the remaining parts of the thesis we refer to unknown model parameters as model parameters for briefness) for the k^{th} model point ($\mathbf{m_k}(x,y)$) as:

$$\mathbf{m_k}(x,y)=\left[h_{k,1};\cdots;h_{k,N};VS_{k,1};\cdots;VS_{k,N+1}\right]. \qquad \textbf{3.6}$$

The vector of model parameters for the whole medium ($\mathbf{m}$) is defined as:

$$\mathbf{m}=\left[\mathbf{m_1}(x,y);\cdots;\mathbf{m_k}(x,y);\cdots;\mathbf{m_K}(x,y)\right]. \qquad \textbf{3.7}$$

To reduce the computational cost in case of SWT inversion in 3D, we consider the *h* values to be constant during the inversion while in 2D media the values of *h* are considered as unknowns and change during the inversion process.

Spatial regularization

Inversion of SW data usually suffers from ill-posedness and non-uniqueness. Stochastic SW inversion approaches (e.g., Wathelet et al., 2004; Dal moro et al., 2007; Maraschini and Foti, 2010; Zhang et al., 2018) could be employed to reduce these problems by investigating a larger portion of the model parameter space than deterministic inversion methods. However, the stochastic methods are computationally expensive. Spatial regularization methods are applied to SW data inversion to address the ill-posedness and non-uniqueness of the inversion process. There are different strategies for spatial regularization. For instance, some authors applied regularization methods to reconstruct sparse models. (Haney and Qu, 2010; Esfahani et al., 2020; Vignoli et al., 2021). Since we started from the implemented codes and the suggested SWT algorithm by Boiero (2009), we used the same spatial regularization method, which was the proposed approach by Auken and Christiansen (2004). They introduced a regularization method for 2D inversion of resistivity data. This regularization method was later applied to surface wave data by Wisén and Christiansen (2005). Since then, it has been widely used by researchers to surface wave data (Boiero, 2009; Socco et al., 2009; Bergamo et al., 2016; Baradaine et al., 2017). In this approach, the spatial constraints are defined to control the degree of variation of each model parameter with respect to its adjacent model points.

The spatial regularization matrix $\mathbf{R}$ controls the extent of lateral variation of each model parameter with respect to its neighbouring model points. The matrix $\mathbf{R}$ is zero for the non-linked parameters, and +1 and -1 for the linked ones:

$$\mathbf{R} = \begin{bmatrix} 1 & 0 & \cdots & -1 & 0 & \cdots & 0 \\ 0 & 1 & 0 & \cdots & -1 & \cdots & 0 \\ \vdots & & \ddots & \vdots & & & \vdots \\ 0 & 0 & \cdots & 1 & 0 & \cdots & -1 \end{bmatrix}. \qquad \textbf{3.8}$$

For instance, for each model parameter of the kth model point ($\mathbf{m}_{i,j}$) in Figure 3.2, $\mathbf{R}$ has only four nonzero values corresponding to its four closest model points (shown in Figure 3.2). The strength of the spatial regularization term is determined by the corresponding covariance matrix $\mathbf{C_R}$. The lower the values of $\mathbf{C_R}$, the stronger the constraints. For instance, a value of 10^4 for the $\mathbf{C_R}$ corresponding to VS value of the generic ith layer of the kth model point imposes a variability of 100 m/s among that layer and the neighbouring model points.

3.1.2 Iterative process

We divide the iterative process in Figure 3.1 into two subsections: forward operator (shown in green) and updating the model (shown in orange) and explain them separately.

3.1.2.1 Forward operator

1D forward modelling

Thomson (1950) suggested a transfer matrix algorithm to obtain the synthetic DC for a 1D (i.e., laterally invariant) layered medium on top of a half-space. The formulation of the method was modified later by Haskell (1953). In this method, the stress and displacement fields at the bottom and top of each layer are computed. The corresponding equations for the intermediate layers are eliminated by assuming the continuity of the normal stress and the displacement field at layer interfaces. For the system to have a non-trivial solution, the determinant of Haskell-Thomson matrix ($\mathbf{HT}(V, f)$), which is a function of phase velocity and frequency, should be zero. The solutions of this equation are different modes of SW. Dunkin (1965) modified the forward algorithm to resolve the issue with having ill-conditioned modal solutions at high frequencies. In our proposed SWT algorithm, we use the 1D forward modelling method proposed by Thomson (1950) and Haskell (1953), modified by Dunkin (1965). For this purpose, we have used *disba* library written in Python, which is a fast, easy to use, and publicly available code (https://github.com/keurfonluu/disba).

For the k^{th} model point in Figure 3.2, the local phase slowness (inverse of phase velocity) for a given frequency $p_k(f)$ is determined using the described 1D forward algorithm as:

$$p_k(f) = g(m_k), \tag{3.9}$$

Ray paths

The difference between the straight- and curved-ray SWT inversion approaches is in the computation of inter-station ray paths. In the straight-ray SWT, for every receiver pair, it is assumed that the ray paths for all frequencies are straight lines. On the other hand, in the curved-ray SWT, the path between each receiver pair should be computed for every frequency component of the DC. To perform the ray tracing at each frequency, we build the corresponding 2D phase velocity map using

the computed local forward responses (Equation 3.9) at each model point. Then, we compute the fastest paths between the two receivers by using an eikonal solver (Noble et al., 2014). We show the algorithm to compute the ray paths in curved-ray SWT in Table 3.1.

Table 3.1. The pseudocode to compute the frequency dependent ray paths in curved-ray SWT.

Algorithm: Computing the frequency dependent ray paths at the n^{th} iteration of curved-ray SWT inversion

Input: vector of model parameter ($\mathbf{m_n}$), position of the grid point (*pos*), vector of unique frequencies of the estimated DCs (**f**).

Output: The matrix of the computed ray paths at the n^{th} iteration ($\mathbf{l_n}$)

% Perform the 1D forward modelling for each of the K model points.

1 **for** *i* **from** 1 **to** *K*

2 $\mathbf{p}_k(f) = g(\mathbf{m_k})$ % p is the vector of phase velocities at the frequency range of $\mathbf{f}_{min}$ to $\mathbf{f}_{max}$

3 **end**

4 **for** *j* **from** 1 **to** *F*

% *F* is the length of vector **f**

5 **do** *map_2D_f_j* = build_phase_velocity_map(*f(j)*, *pos*, $[p_1(f(j)); \ldots; p_K(f(j))]$)

% *map_2D_f_j* is the built 2D phase velocity map at the frequency *f(j)*.

6 **for** *i* **from** 1 **to** *N*

% *N* is the number of estimated *DCs*

7 **do** $l_{R_{1,i},R_{2,i}}(f(j))$ = ray_tracing*(map_2D_f_j, pos($R_{1,i}$, $R_{2,i}$))*

%$R_{1,i}$, $R_{2,i}$ are the positions of the first and second receiver for the i^{th} estimated DC, and $l_{R_{1,i},R_{2,i}}(f(j))$ shows the computed discretised fastest path between these two receiver position.

8 $\mathbf{l_n}(i,j) = l_{R_{1,i},R_{2,i}}(f(j))$

9 **end**

10 **end**

Computing forward response

Then, the frequency dependent ray path between the receiver pair (R_1-R_2) is discretized to many points. Figure 3.3 shows a schematic representation of the bilinear interpolation along the discretised path between the receiver pair.

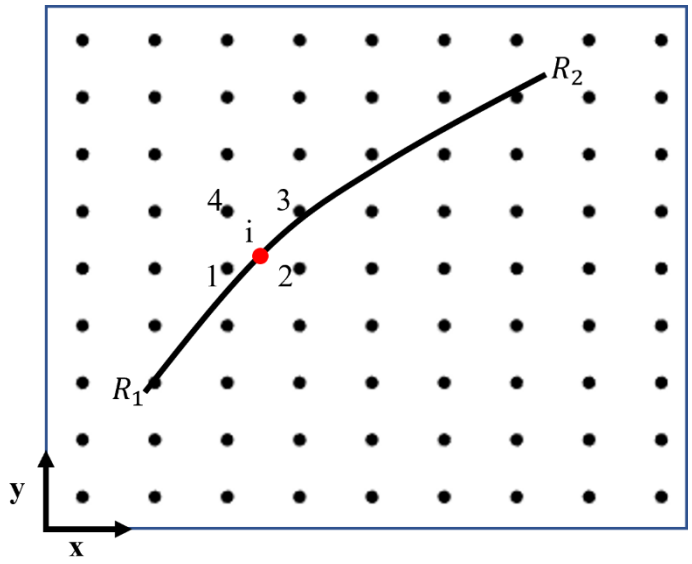

Figure 3.3. The ray path between receivers R_1 and R_2 at a generic frequency is represented by the solid black line. The phase slowness for any discretised point (i) along the path is computed based on the values of its four adjacent grid points using a bilinear interpolation (Equation 3.10). (See also Boiero, 2009).

At the generic i^{th} discretised point (shown in red in Figure 3.3) along the path ($l_{R_1R_2}$), the phase slowness (p_i) is computed using a bilinear interpolation among the computed 1D local forward models at the four surrounding gird points as:

$$p_i(f) = \frac{\sum_{m=1}^{2} |x_i - x_{m+2}||y_i - y_{m+2}| p_m + |x_i - x_m||y_i - y_m| p_{m+2}}{|(x_1 - x_2)(y_1 - y_2)|} \qquad \textbf{3.10}$$

where x and y show the position of each point in Figure 3.3. Since the ray path ($l_{R_1R_2}$) in Equation 3.10 would be different for the straight-ray and curved-ray approaches (unless the computed ray path in the curved-ray approach is also a straight line), the computed phase slowness from Equation 3.10 would be different

in case of the straigh-ray and curved-ray SWT approaches. The path-average phase slowness along the path for each frequency ($p_{R_1R_2}(f)$) is then computed as:

$$p_{R_1R_2}(f) = \frac{\int_{l_{R_1R_2}} p_i(f,l)\,dl}{\int_{l_{R_1R_2}} dl}, \qquad \textbf{3.11}$$

The corresponding phase velocity ($V_{R_1R_2}(f)$) is equal to the inverse of the computed phase slowness:

$$V_{R_1R_2}(f) = \frac{1}{p_{R_1R_2}(f)} \qquad \textbf{3.12}$$

We obtain the simulated DC for the receiver pair (R_1- R_2) by:

$$\mathbf{DC}_i = \left[V_{R_1R_2}(f_1);\ \ldots;\ V_{R_1R_2}(f_n)\right], \qquad \textbf{3.13}$$

where $f_1, \ldots, f_n$ represent the frequency components of the corresponding DC. It should be noted that each estimated DC may have a frequency band different from the others and therefore, the lengths of DCs are not the same. The experimental DCs consist of a vector of frequencies ($\mathbf{f}$) with their corresponding phase velocities. The vector of the forward response of the model ($\mathbf{fw}(\mathbf{m})$), which contains the simulated phase velocities corresponding to each element of $\mathbf{f}$, is then obtained as:

$$\mathbf{fw}(\mathbf{m}) = \left[\mathbf{DC_1};\ldots;\mathbf{DC_i};\ldots;\mathbf{DC_n}\right]. \qquad \textbf{3.14}$$

3.1.2.2 Updating the model

We define an initial model to start the inversion process. We solve the inverse problem using a damped weighted least-squares method suggested by Boiero (2009). At the n^{th} iteration, we update the model at the current iteration $\mathbf{m_n}$ to $\mathbf{m_{n+1}}$ as:

$$\mathbf{m_{n+1}} = \mathbf{m_n} + \left(\begin{array}{l}\left[\mathbf{G^T C_{exp}^{-1} G} + \mathbf{R^T C_R^{-1} R} + \lambda\mathbf{I}\right]^{-1} \\ \times\left[\mathbf{G^T C_{exp}^{-1}}\left(\mathbf{d_{exp}} - \mathbf{fw}(\mathbf{m_n})\right) + \mathbf{R^T C_R^{-1}}\left(\mathbf{-Rm_n}\right)\right]\end{array}\right), \qquad \textbf{3.15}$$

where λ represents the damping factor (see Marquardt, 1963, for details). The damping factor (λ) is used to prevent the matrix singularity and to stabilize the solution. The matrix $\mathbf{G}$ consists of the sensitivity of the data to the model parameters. The dimension of $\mathbf{G}$ is determined by the number of data (n_d) and model parameters (n_m). For the generic i^{th} layer of the k^{th} model point, the sensitivity matrix is built as:

$$\mathbf{G} = \begin{bmatrix} \cdots & \cdots & \cdots & \cdots & \cdots \\ \cdots & \dfrac{\partial \mathbf{fw}(\mathbf{m})}{\partial h_{k,i}} & \cdots & \dfrac{\partial \mathbf{fw}(\mathbf{m})}{\partial VS_{k,i}} & \cdots \\ \cdots & \cdots & \cdots & \cdots & \cdots \end{bmatrix}_{n_d \times n_m} . \qquad \textbf{3.16}$$

As mentioned previously, in case of SWT inversion in 3D, we consider the h values to be constant and consequently, they would be removed from Equation 3.16. The partial derivatives in Equation 3.16 are approximated using a Taylor expansion. For the generic j^{th} element of the model parameters vector ($\mathbf{m}_j$), the partial derivative is computed as:

$$\frac{\partial \mathbf{fw}(\mathbf{m})}{\partial m_j} \approx \frac{\partial \mathbf{fw}(\mathbf{m} + dm_j.\mathbf{e_j}) - \partial \mathbf{fw}(\mathbf{m} - dm_j.\mathbf{e_j})}{2dm_j}, \qquad \textbf{3.17}$$

where dm_j shows the degree to which m_j is perturbed and $\mathbf{e_j}$ is the unit vector with the size of model vector ($\mathbf{m}$) and it has non-zero value only at its j^{th} element. We set dm_j equal to 5% of m_j . The amount the perturbation (dm_j) should be small enough to satisfy the linearization condition around m_j, but not too small to introduce rounding errors at the numerator (Aster et al., 2005).

3.1.3 Stopping criteria

We define two stopping criteria to end the inversion process. The inversion ends when either number of iterations exceeds 35 or the relative difference between the misfit value of the updated model (Φ_{n+1}) and the current model (Φ_n) is less than 10^{-4} as:

$$\frac{\Phi_n - \Phi_{n+1}}{\Phi_n} < 10^{-4}, \qquad \textbf{3.18}$$

If one of these conditions is met, the inversion stops and the updated model ($\mathbf{m}_{n+1}$) is considered as the final model.

The proposed SWT inversion algorithm has been applied to different 2D and 3D datasets and the results are shown in Chapters 4 and 5.

3.2 Joint inversion of SWT and BWT

Our proposed tomographic inversion SWT and BWT is a further evolution of our SWT inversion scheme, and it has been also implemented in Python. We propose a fully tomographic approach for the joint inversion of SWT and BWT. To the best of our knowledge, this is the first tomographic approach to integrate the extracted DCs and first-arrivals from active seismic data. Garofalo (2014) proposed an algorithm and implemented an inversion code (in MATLAB) to invert SW, first-arrival, and resistivity data to build semi 2D VS, VP, and resistivity models. We started from that work and employed the integration and normalisation methods by Garofalo (2014). We replaced SWA by SWT. SWT provides the possibility to consider the lateral variability of the subsurface in the forward operator. We also extended our method to 3D and employed a more advanced eikonal solver which can operate both in 2D and 3D. We used an open access, parallel Python library (fteikpy library, which is available at https://github.com/keurfonluu/fteikpy) to perform forward modelling in BWT based on the proposed method by Noble et al. (2014). In the following paragraphs, we explain our scheme for the joint inversion of SWT and BWT.

BWT based on first-arrival times data consists of inverting the P-wave first arrival times to build VP models. In the 1D forward modelling of SWT, a VP distribution of the subsurface is needed. In SWT, it is commonly assumed that the VP model is known as a priori information, and DC data are inverted to get a VS model. Alternatively, the obtained VP model from BWT at each iteration can be used in SWT forward modelling. This has been the main idea in the studies that have integrated SW methods and BWT (Dal Moro, 2008; Pasquet et al., 2015; Fang et al., 2016; Bardainne, 2018; Toney et al., 2019). Here, we employ the latter method and use the obtained VP model from BWT at each iteration in the forward modelling of SW. We propose a SWT and BWT joint inversion algorithm in which VP and h are the common parameters between the two methods. Moreover, we suggest using Poisson's ratio (ν) as the physical constraint in the joint inversion of SWT and BWT. It should be noted that even though the VS model from SWT does not affect the forward modelling of BWT, it is used to compute the ν model at every

iteration. In our 3D individual and joint inversions, we consider the h values to be constant during the inversion to reduce the computational cost the inversion. However, in 2D the values of h are considered as unknowns and update during the inversion process. In Table 3.2, we list the joint inversion parameters and specify which parameters are updated during the joint inversion, which parameters are common between the forward modelling of SWT and BWT, and which parameters act as the inversion constraint.

Table 3.2. Model parameters in the proposed joint inversion algorithm.

Joint inversion parameters	VS	VP	h		ν	ρ
			2D	3D		
Updated during inversion	✓	✓	✓	×	×	×
Used in both SWT and BWT forward model	×	✓	✓	×	×	×
Act as inversion constraint	**(×)**	**(×)**	**(×)**	×	✓	×

Even though we do not use VS, VP, and h (in 2D) as inversion constraint, their values can be constrained by means of spatial regularization, and we have used parentheses in Table 3.2 to clarify it. The forward response of BWT is computed by solving the eikonal equation. Solving the elastic wave equation by applying the high-frequency approximation gives the eikonal equation. The eikonal equation in 3D Cartesian coordinates can be defined as:

$$\left(\frac{\partial t}{\partial x}\right)^2+\left(\frac{\partial t}{\partial y}\right)^2+\left(\frac{\partial t}{\partial z}\right)^2=s^2(x,y,z), \qquad \textbf{3.19}$$

where t is the traveltime, s is the slowness, and x, y, and z show the Cartesian coordinates.

Different approaches have been proposed to solve the eikonal equation. Vidal (1988) first introduced the finite-difference approximation to solve the eikonal

equation, which provided accurate traveltimes for smooth velocity models. However, this model could not provide accurate traveltimes in presence of sharp velocity contrasts in the medium. Since then, many researchers have tried to improve the accuracy of this approach and address the associated problems with the source singularity and highly heterogeneous media (Podvin and Lecomte, 1991; Hole and Zelt, 1995; Qian and Symes, 2002; Rawlinson and Sambridge, 2004a; Zhang et al., 2005; Fomel et al., 2009). Noble et al. (2014) suggested a hybrid algorithm to combine a spherical approximation of the eikonal equation close to the source and a plane wave approximation for further distances from the source, to handle the issues related to the source singularity and highly heterogeneous media. Since shallow subsurface media are known to be usually complex and highly heterogeneous, we have chosen this method (Noble et al., 2014) to compute the forward response of the model in BWT at the near-surface scale.

The applied inversion algorithm in the joint inversion of SWT and BWT is based on the inversion algorithm for SWT which was described in Section 3.1. However, in the following paragraphs, we explain the main differences, which are the integration of the two methods, normalisation, and the employed physical constraint in the joint inversion algorithms. Figure 3.4 shows a schematic representation of the joint inversion algorithm.

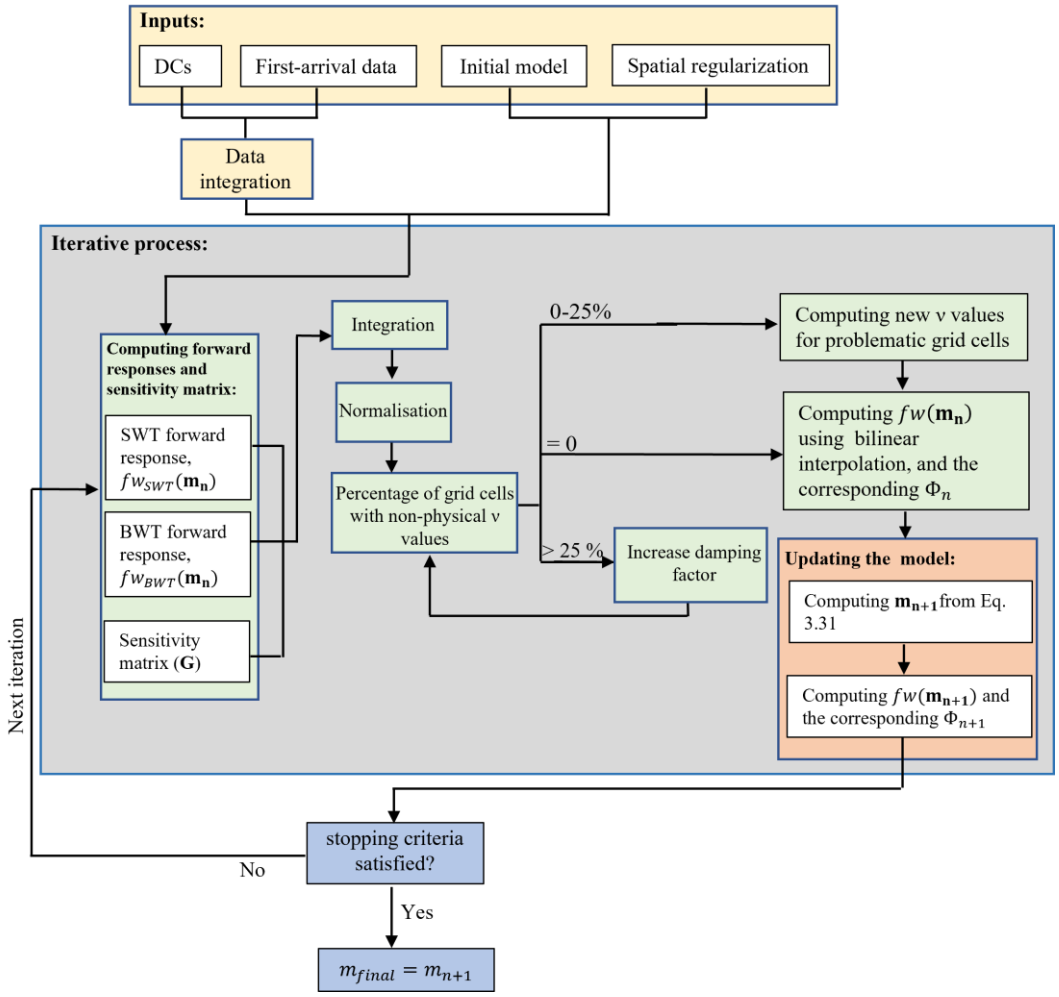

Figure 3.4. Scheme of the proposed algorithm for the joint inversion of SWT and BWT.

3.2.1 Integration of SWT and BWT

The input data for the joint inversion of SWT and BWT are DCs and first-arrival travel times $\mathbf{tt}$, respectively. Each element of $\mathbf{tt}$ is related to a source receiver couple and each DC correspond to a pair of receivers. The input data for the joint inversion are integrated in the experimental data vector $\mathbf{d}_{exp}$ as:

$$\mathbf{d}_{exp} = [\mathbf{DC}; \mathbf{tt}]. \qquad \mathbf{3.20}$$

The data uncertainty is described by covariance matrix $\mathbf{C}_{exp}$ as:

$$\mathbf{C}_{\exp} = \begin{bmatrix} \mathbf{C}_{DC} & 0 \\ 0 & \mathbf{C}_{tt} \end{bmatrix}, \qquad \textbf{3.21}$$

where $\mathbf{C_{dc}}$ represents the covariance matrix of DC data and $\mathbf{C_{tt}}$ is the covariance matrix for first-arrival travel times. In the joint inversion of BWT and SWT, the model parameters at each layer are *h*, VS, and VP. So, the vector of model parameters for the generic kth model point ($\mathbf{m_k}(x,y)$) is defined as:

$$\mathbf{m_k}(x,y) = \left[h_1; \cdots; h_N; VS_1; \cdots; VS_{N+1}; VP_1; \cdots; VP_{N+1}\right], \qquad \textbf{3.22}$$

and the vector of model parameters $\mathbf{m}$ is defines as:

$$\mathbf{m} = \left[\mathbf{m_1}(x,y); \cdots; \mathbf{m_k}(x,y); \cdots; \mathbf{m_K}(x,y)\right], \qquad \textbf{3.23}$$

The forward response $fw(\mathbf{m})$ of the model $\mathbf{m}$ in the proposed joint inversion algorithm is given by:

$$fw(\mathbf{m}) = \begin{bmatrix} fw_{SWT}(\mathbf{m}) \\ fw_{BWT}(\mathbf{m}) \end{bmatrix}, \qquad \textbf{3.24}$$

where $fw_{SWT}(\mathbf{m})$ and $fw_{BWT}(\mathbf{m})$ are the forward responses of SWT and BWT, respectively. Equation 3.16 is modified as:

$$\mathbf{G} = \begin{bmatrix} \cdots & \cdots & \cdots & \cdots & \cdots & \cdots & \cdots \\ \cdots & \dfrac{\partial \mathbf{fw}(\mathbf{m})}{\partial h_{k,i}} & \cdots & \dfrac{\partial \mathbf{fw}(\mathbf{m})}{\partial VS_{k,i}} & \cdots & \dfrac{\partial \mathbf{fw}(\mathbf{m})}{\partial VP_{k,i}} & \cdots \\ \cdots & \cdots & \cdots & \cdots & \cdots & \cdots & \cdots \end{bmatrix}. \qquad \textbf{3.25}$$

It should be noted that like SWT inversion, if the joint inversion is carried out in 3D, we do not update *h* values (i.e., their corresponding terms would be removed from Equation 3.25) to reduce the computational cost of the inversion.

3.2.2 Normalisation

Experimental datasets with different dimensions are integrated in the joint inversion. Researchers have employed different normalisation methods in their

joint inversion studies (Linde et al., 2008; Doetsch et al., 2010; Molodtsov et al., 2015; Colombo and Rovetta, 2018, Jordi et al., 2019).

The input data for SWT and BWT have velocity and time dimensions, respectively. Also, the elements of $\mathbf{m_n}$ have different dimensions and their sensitivity can be different by orders of magnitudes. Therefore, normalisation is important for the stability of the proposed joint inversion results. We follow the normalisation approach suggested by Boiero and Socco (2014) and implemented in MATLAB by Garofalo (2014). We normalise the ith component of the error between experimental data and forward response (Δd_i) as:

$$\Delta d_i = \frac{d_{\exp,i} - fw(\mathbf{m_n})_i}{d_{\exp,i}}. \qquad \textbf{3.26}$$

Subsequently, the covariance matrix of experimental data ($\mathbf{C}_{\exp}$) should also be normalised. The ith diagonal element of $\mathbf{C}_{\exp}$ is normalised as:

$$\hat{C}_{\exp,ii} = \frac{C_{\exp,ii}}{d^2_{\exp,i}}. \qquad \textbf{3.27}$$

In case of model parameters, the jth element of the model vector (m_j) is normalized as:

$$\hat{m}_j = \frac{m_j}{m_{n,j}}. \qquad \textbf{3.28}$$

The normalization to model parameters is also applied to the regularization covariance matrix $\mathbf{C_R}$ as:

$$\hat{C}_{R,jj} = \frac{C_{R,jj}}{m^2_{n,j}}. \qquad \textbf{3.29}$$

The sensitivity matrix should be normalised for both data and model parameters. The $\hat{G}_{n,ij}$ element of the sensitivity matrix, which corresponds to the ith element of the data and the jth element of the model parameters, is normalised as:

$$\hat{G}_{n,ij} = \frac{\partial fw(\mathbf{m_n})_i}{\partial m_j} \frac{m_{n,j}}{d_{\exp,i}}. \qquad \textbf{3.30}$$

To update the model at the n[th] iteration of the joint inversion algorithm, the Equation 3.15 is modified to:

$$\mathbf{m_{n+1}} = \mathbf{m_n} \left(\hat{\mathbf{m}} + \left(\begin{array}{l} \left[\hat{\mathbf{G}}^{\mathbf{T}} \hat{\mathbf{C}}_{\mathbf{exp}}^{\mathbf{-1}} \hat{\mathbf{G}} + \mathbf{R}^{\mathbf{T}} \hat{\mathbf{C}}_{\mathbf{R}}^{\mathbf{-1}} \mathbf{R} + \hat{\lambda} \mathbf{I} \right]^{-1} \\ \times \left[\hat{\mathbf{G}}^{\mathbf{T}} \hat{\mathbf{C}}_{\mathbf{exp}}^{\mathbf{-1}} \Delta \mathbf{d} + \mathbf{R}^{\mathbf{T}} \hat{\mathbf{C}}_{\mathbf{R}}^{\mathbf{-1}} \left(\mathbf{-R} \hat{\mathbf{m}}_{\mathbf{n}} \right) \right] \end{array} \right) \right). \qquad \textbf{3.31}$$

3.2.3 Physical Constraint

The obtained VS model from SWT and VP model from BWT are linked through ν which is defined as:

$$\nu = \frac{0.5\left(\frac{VP}{VS}\right)^2 - 1}{\left(\frac{VP}{VS}\right)^2 - 1}. \qquad \textbf{3.32}$$

At each iteration of the joint inversion, the Poisson's ratio value of each layer of every model point is computed. To be physically meaningful, Poisson's ratio should be higher than 0 and lower than 0.5. Negative values of Poisson's ratio might be obtained if the ratio of VP/VS is less than $\sqrt{2}$, (dashed line in Figure 3.5) and it could be more than 0.5 if $VP < VS$.

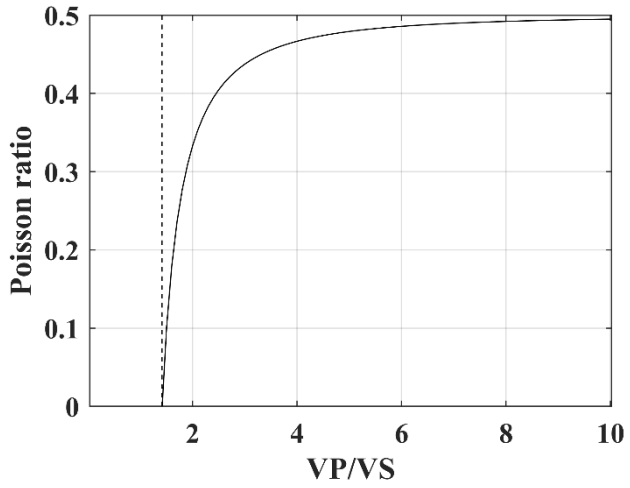

Figure 3.5. Poisson's ratio value as a function of VP/VS ratio. The dashed line corresponds to VP/VS ratio of $\sqrt{2}$ *. Poisson ratio values which are not in the range of 0-0.5 are not physically meaningful.*

In the proposed joint inversion algorithm, ν values are not updated during the inversion but they are used as a physical constraint in the inversion process. If at any iteration more than 25% of grid points have non-physical ν values, the damping factor (λ) is changed until at least 75 % of all ν values in the updated model vector $\boldsymbol{m_{n+1}}$ have physical values. Then, for each remaining grid point with a non-physical ν value, new VP and VS values are computed by averaging the corresponding values of the four closest grid points which have physical ν values. Having computed new velocities for these grid points, new ν values are computed using Equation 3.32. The algorithm to compute new ν for the grid points with non-physical ν is shown in Table 3.3.

Table 3.3. Correcting non-physical ν values in the joint inversion pseudocode.

Algorithm: Correcting for non-physical Poisson ratio values in the joint inversion

Input: updated model ($\mathbf{m}_{n+1}$), position of the grid point (*pos*), minimum allowed value of Poisson ratio (ν_{min}), maximum allowed value of Poisson ratio (ν_{max}), current Poisson ratio model ($\mathbf{m}_{\nu}$).

Output: updated model with corrected Poisson ratio values ($\mathbf{m}_{n+1_{new}}$)

% Find cells which have physical ν. The default values of ν_{min} and ν_{max} are 0 and 0.5, respectively.

1 **do** *cell_physical_v* = find ($\mathbf{m}_{\nu} > \nu_{min}$ **and** $\mathbf{m}_{\nu} < \nu_{max}$)

% Find cells which have non-physical ν.

2 **do** *cell_non_physical_v* = find ($\mathbf{m}_{\nu} <= \nu_{min}$ **or** $\mathbf{m}_{\nu} >= \nu_{max}$)

% $N_{cell\_non\_physical\_v}$ is the number of cells with non-physical ν.

3 **for** *i* **from** 1 **to** $N_{cell\_non\_physical\_v}$

% Computing the distance of the i^{th} cell with non-physical ν from all the cells which have physical ν.

4 *distances* = compute_distance ($(cell\_non\_physical\_v)_i$, *cell_physical_v*)

% Finding the four cells with the smallest distance from the i^{th} cell with non-physical ν.

5 *cell_4* = find_smallest_distances(*distances*)

% Computing the new velocities (VS_i and VP_i) by averaging the corresponding values of *cell_4*

6 VS_i = mean (VS_{pos_4})

7 VP_i = mean (VP_{pos_4})

% Computing the new ν based on the new velocity values (VS_i and VP_i)

8 $\nu_i = (0.5*(VP_i/ VS_i)^2-1)/ ((VP_i/ VS_i)^2-1)$

9 **end**

Having physical Poisson's ratio values for all model points, the inversion process can continue to the next iteration. The inversion stops when one of the stopping

criteria is satisfied. The proposed joint inversion method has been applied to different 2D and 3D datasets in Chapter 5.

3.3 Different types of defined misfits

We use different types of misfits in this thesis. To avoid confusion, we explain them in the following. First, we have defined the global misfit in Equation 3.1. The values of the global misfit can be monitored during the inversion to evaluate the convergence of the inversion process. We also define the average relative data misfit (e_d) as:

$$e_d = mean\left(\frac{\left|\mathbf{d}_{\mathbf{exp}} - \mathbf{fw}\left(\mathbf{m}_{\mathbf{final}}\right)\right|}{\mathbf{d}_{\mathbf{exp}}}\right). \qquad \textbf{3.33}$$

where $\mathbf{d}_{\mathbf{exp}}$ is the vector of the experimental data and $\mathbf{fw}\left(\mathbf{m}_{\mathbf{final}}\right)$ represents the computed forward response of the model at the final iteration of the inversion. The defined e_d shows the overal misfit between the experimental and simulated data. For the generic ith DC, we define the local DC misfit (e_c), that represents the relative local error between phase velocities of the experimental DC ($\mathbf{V}_{\mathbf{exp,i}}$) and the corresponding simulated phase velocities ($\mathbf{V}_{\mathbf{sim,i}}$) as:

$$e_c = mean\left(\frac{\left|\mathbf{V}_{\mathbf{exp,i}} - \mathbf{V}_{\mathbf{sim,i}}\right|}{\mathbf{V}_{\mathbf{exp,i}}}\right). \qquad \textbf{3.34}$$

Since we know the true VS model (VS_{true}) in case of numerical examples, we define average relative model misfit (e_m) to evaluate the obtained VS models from the inversions (VS_{final}) with VS_{true} as:

$$e_m = \frac{1}{n_c}\sum_{i=1}^{nc}\left(\frac{\left|VS_{i,true} - VS_{i,final}\right|}{VS_{i,true}}\right), \qquad \textbf{3.35}$$

where n_c shows the total number inversion cells.

3.4 Conclusions

We described the employed SWT inversion algorithm for direct inversion of DC data, without building phase velocity maps, to obtain VS models in 2D and 3D. We also illustrated the differences between the forward operators of straight-ray and curved-ray approaches in 3D. Then, we presented a scheme to integrate SWT and BWT methods in a joint inversion scheme which can be applied in both 2D and 3D media. We described the procedure to obtain physically meaningful VS and VP (and the corresponding ν) models from the proposed joint inversion. We explained the employed method to integrate the experimental data and the normalisation approach which were crucial steps at the integration of SWT and BWT. Moreover, we illustrated the applied mechanism to constrain the VS model from SWT and the VP model from BWT through Poisson's ratio. We also explained the proposed approach to make sure that the obtained velocity models at every iteration of the joint inversion would lead to a physically meaningful Poisson's ratio distribution. We applied the described methodologies to different numerical and field examples and the results are shown in Chapters 4 and 5.

Chapter 4

Evaluation of straight-ray and curved-ray SWT[1]

In this chapter, we investigate how the inversion results depend on whether straight rays or curved rays are used in modelling SWT. we apply straight-ray and curved-ray SWT to four 3D datasets. We aim to investigate the difference between the results of straight-ray and curved-ray SWT at near-surface scale.

SWT has been used in seismological studies for decades and different SWT approaches have been compared by seismologists. For instance, Laske (1995) studied deviations from straight line in the propagation of long-period surface waves and concluded that they usually have small effects on the propagation phase. Spetzler et al. (2001) applied both straight-ray and curved-ray SWT methods. They computed the maximum deviations of ray paths from straight lines and pointed out that this maximum is typically below the estimated resolution, except for long paths at short periods.

Some studies showed that a more complex forward modelling in SWT did not improve the results (Sieminski et al., 2004; Levshin et al., 2005) while other studies reported obtaining better results (Ritzwoller et al., 2002; Yoshizawa and Kennett, 2004; Zhou et al., 2005). Trampert and Spetzler (2006) pointed out that a common practice in SWT is to show "nice" (smooth) results and hence, the choice of regularization has a major impact on SWT results. They studied SWT methods based on ray theory (straight-ray and curved-ray) and scattering theory in which the integral along the ray path is replaced by the integral over an influence zone. They showed that both methods are statistically alike and any model from one method can be obtained by the other one by changing the value of the regularization. They

[1] This chapter is based on the following paper:
Karimpour, M., Slob, E., and Socco, L.V., 2022, A comparison of straight-ray and curved-ray surface wave tomography approaches at near-surface studies, Solid Earth [preprint], doi: 10.5194/egusphere-2022-279.

concluded that the only option to increase the resolution of the model is to increase and homogenize the data coverage. Bozdag and Trampert (2008) compared straight-ray and curved-ray SWT methods in their study and mentioned that performing ray tracing could be so time-consuming that the potential gain in crustal corrections on a global scale might not be worth the additional computational effort imposed by ray tracing.

We evaluate straight-ray and curved-ray SWT at the near-surface scale. We invert the DCs using the algorithm explained in Section 3.1 to obtain a VS model. We start SWT inversion from the same initial model for both straight-ray and curved-ray approaches. We first show the results for the synthetic examples: the Blocky model and the Sand Bar model. Since the true VS models are known for the synthetic examples, it is possible to evaluate the obtained VS models from the SWT inversions quantitatively. Afterwards, we apply the straight-ray and curved-ray SWT to two field examples: the Pijnacker field and the CNR field. For the field examples, we assess the VS models based on the available information for each site. In case of the Pijnacker site, some nearby borehole data are available and for the CNR site, the borders of the target (loose sand anomaly) are known. Finally, we compare the obtained results from straight-ray and curved-ray SWT in terms of data misfits, model misfits, and computational cost.

4.1 Blocky model

We define an initial model with 2 m cell size (both vertically and horizontally). The initial VS values are set to 200 m/s in all cells and the initial values of VP and ρ are the true ones. We set very weak spatial regularization by choosing the values of $\boldsymbol{C_R}$ equal to 10^6. The SWT inversion starts from the same initial model for both straight- and curved-ray SWT.

We show the values of the misfit function (Φ) at different iterations of straight-ray and curved-ray SWT in Figure 4.1. We see that the initial values of misfit are the same for both inversions Also, the final values of misfit are almost the same. However, the taken paths from the initial to the last iteration are different for the straight- and curved-ray. The straight-ray has converged faster than the curved-ray SWT (16 vs. 20 iterations). Besides, the computed misfit values at each iteration are not the same for straight- and curved-ray. This difference is more obvious at the 4^{th} and 7^{th} iterations. We show the obtained VS models at the last iterations of the straight- and curved-ray SWT in Figure 4.2.

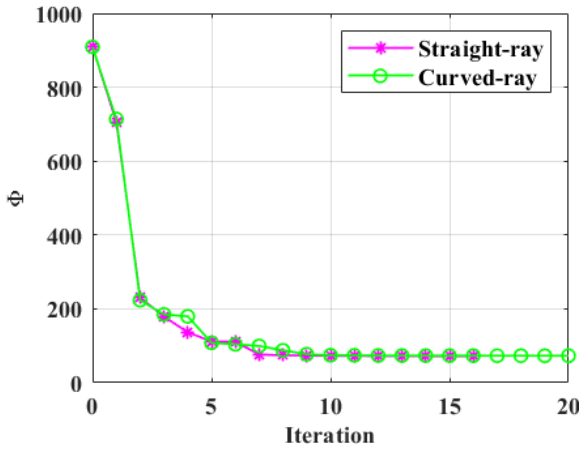

Figure 4.1. The computed values of the misfit function at different iterations of the straight-ray and curved-ray SWT.

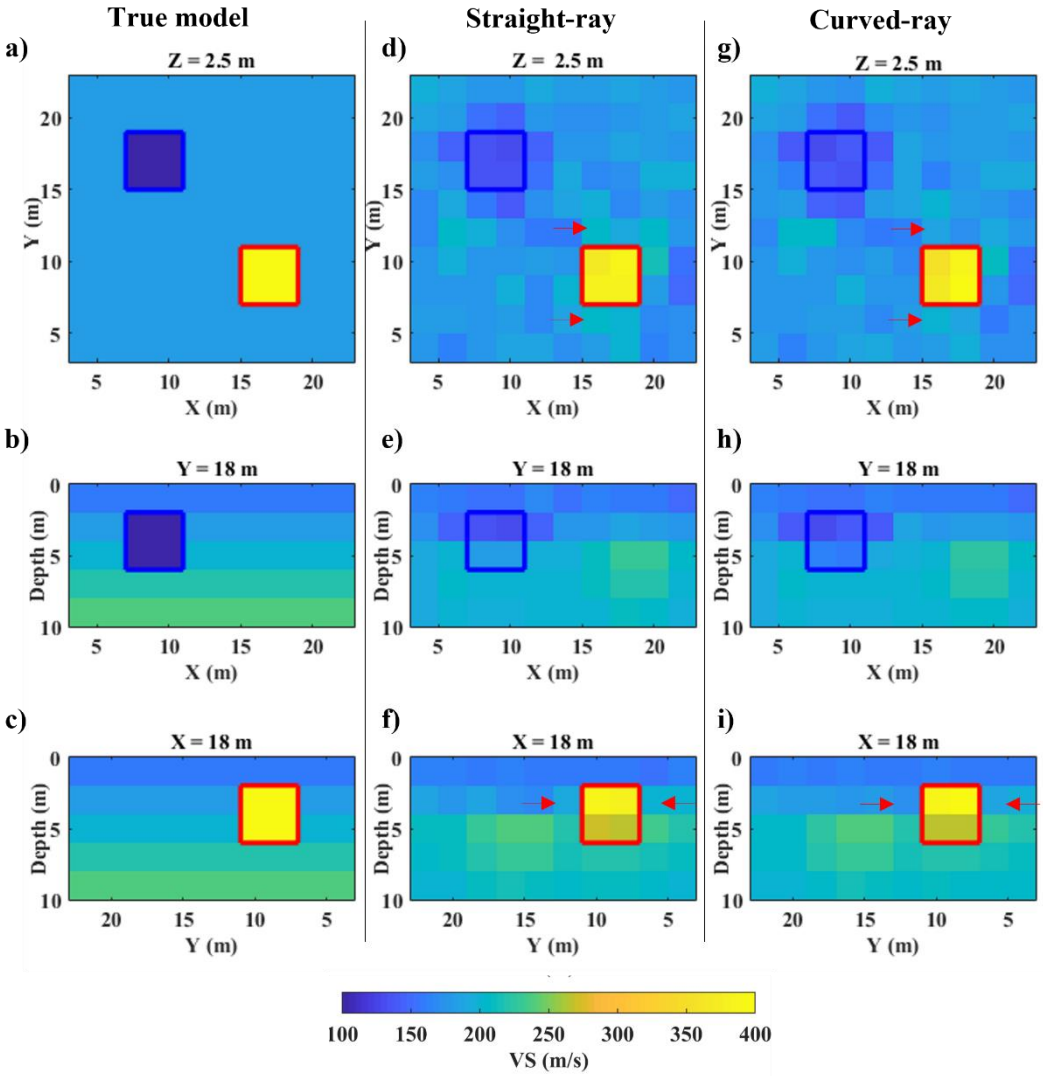

Figure 4.2. The true VS model and the obtained VS models from SWT inversions. The slices of true model are shown in subfigures (a-c) and the corresponding VS models from the straight-ray and curved-ray SWT are shown in subfigures (d-f) and (g-i), respectively. The shown 2D velocity models correspond to three different slices: horizontal slice at 2.5 m depth (subfigures a, d, and g), vertical slice at Y = 18 m (subfigures b, e, and h), and the vertical slice at X=18 m (subfigures c, f, and i). The red arrows show the cells around the high-velocity anomaly where the VS values from straight- and curved-ray have high differences compared with the rest of the medium. All subfigures have the same colour scale which is shown at the bottom of the figure.

Figure 4.2 shows that the obtained VS models from the straight-ray (Figure 4.2a to c) and curved-ray (Figure 4.2d to f) are very similar. In case of the high-

velocity anomaly, we can see that both approaches have modelled the location and the value of the high-velocity block accurately. As shown by the red arrows in Figure 4.2, the model from the curved-ray SWT (Figure 4.2g and i) is slightly better than the straight-ray SWT result (Figure 4.2d and f) at the grid blocks surrounding the high-velocity anomaly. In case of the low-velocity anomaly, both approaches have provided very similar results in the horizontal slices (Figure 4.2d and g). However, by comparing the vertical slices (Figure 4.2e and h) with the true VS model, we can see that the curved-ray SWT has provided better results since the bottom half of the low-velocity block is better retrieved by the curved-ray (Figure 4.2h) than the straight-ray (Figure 4.2e).

Using Equation3.35, we obtain a slightly lower value of e_m for the model from the curved-ray (9.23 %) than the straight-ray (9.74%). In Figure 4.3, we show the distribution of model misfit for the obtained VS model from straight-ray (Figure 4.2d-f) and curved-ray SWT (Figure 4.2g-i).

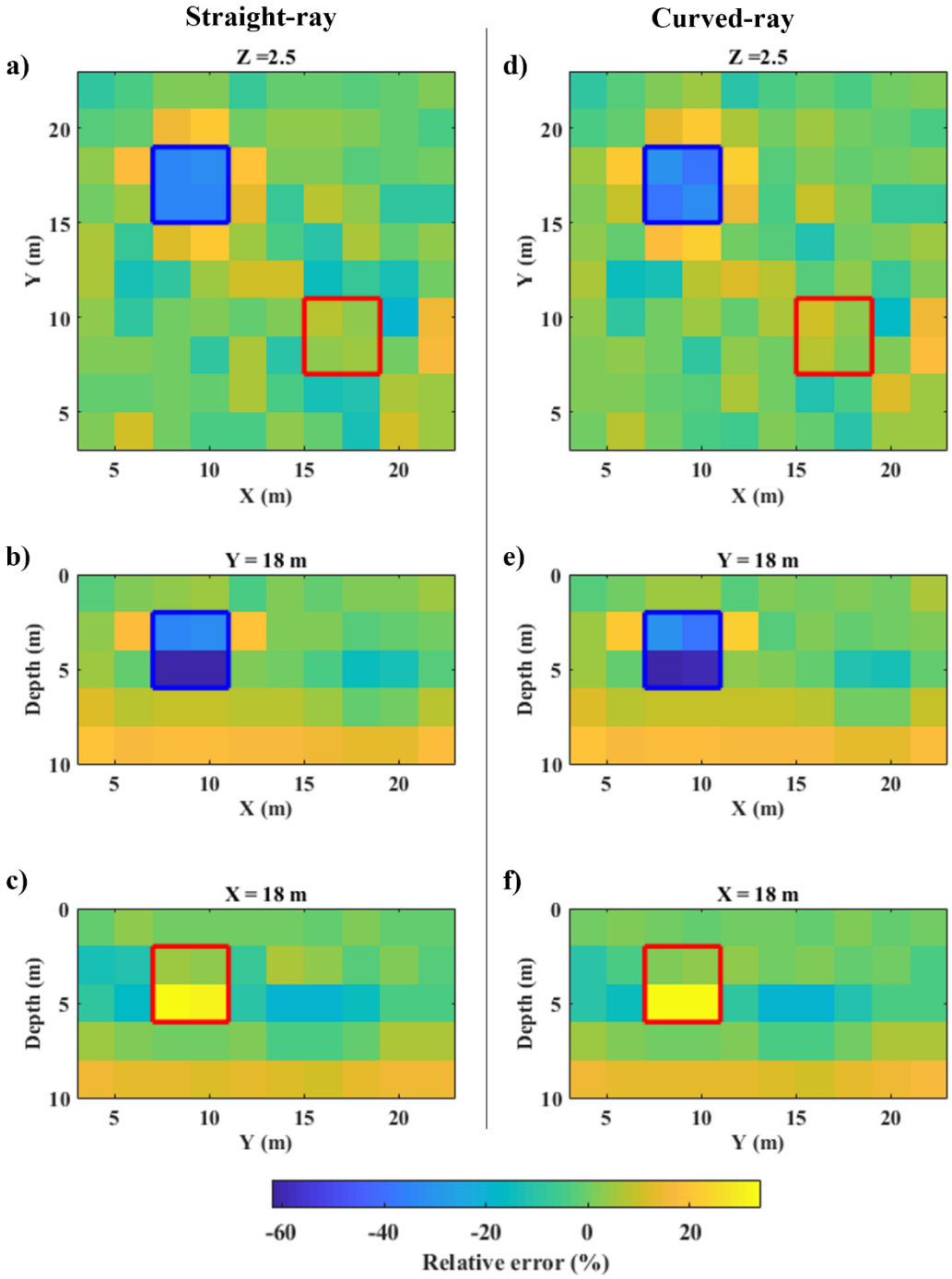

Figure 4.3. Distribution of model misfits at the last iteration of the inversion of straight-ray (subfigures a-c) and curved-ray SWT (subfigures d-f). The boundaries of the low- and high-velocity anomalies are superimposed in blue and red, respectively.

Using Equation 3.33, the computed value of e_d is 0.99% for both straight-ray and curved-ray approaches. For each DC, we have computed the misfit between the experimental and simulated DCs (e_c). We assign each misfit value to the location at the middle of the corresponding receiver couple. While e_d shows and average misfit value for all the DCs, we can see the spatial distribution of the local DCs misfit (e_c) in Figure 4.4.

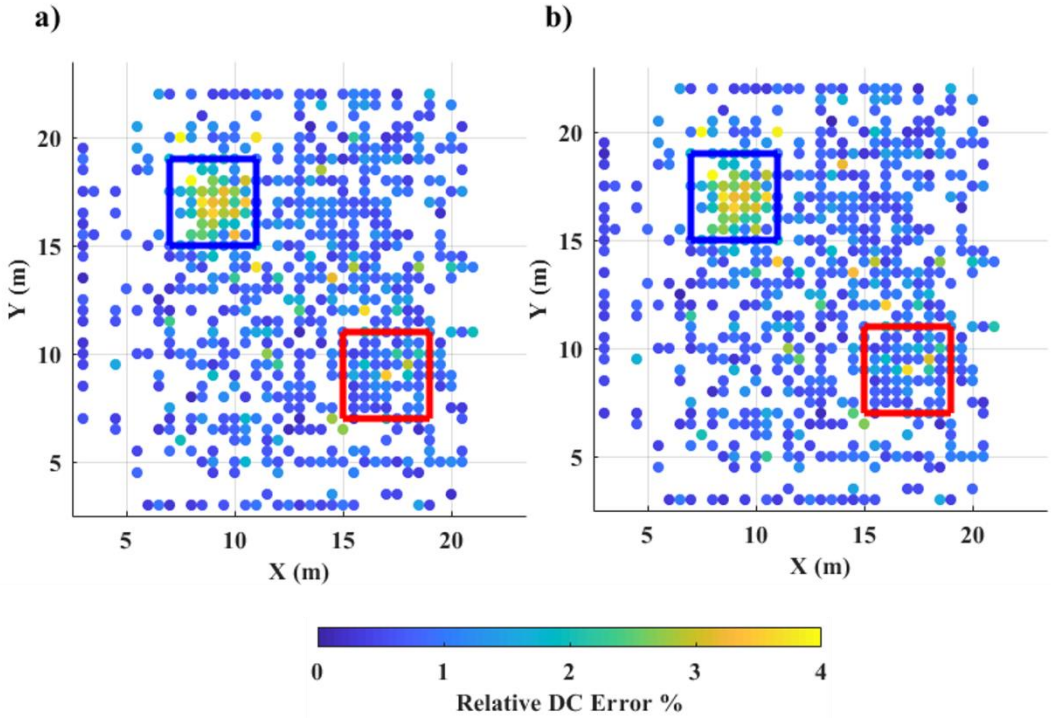

Figure 4.4. Distribution of local DCs misfits (e_c) at the last iteration of the inversion of a) straight-ray SWT, b) curved-ray SWT. The boundaries of the low- and high-velocity anomalies are superimposed in blue and red, respectively.

Figure 4.4 shows that the final values of DC misfits at different locations are very similar for the straight- and curved-ray. We can see in Figure 4.4 that for both approaches, most locations with high misfits (3-4 %) are inside the block of low velocity. We also see that the data misfits are very small for both approaches: 63 % of the simulated DCs from the straight-ray and 62 % of the DCs from the curved-ray have misfit values less than 1 %.

We show two examples of DCs and their fittings in Figure 4.5. In the first example (Figure 4.5a), the ray paths between the receiver couples cross the high-

velocity block, and in Figure 4.5b they travel through the low-velocity block. The average relative DC misfits in the first case (Figure 4.5a) are 0.71 % and 0.59 % for the straight-ray and curved-ray SWT, respectively. In the second example (Figure 4.5b), the misfits are 0.40 % and 0.39 % for the straight- and curved-ray.

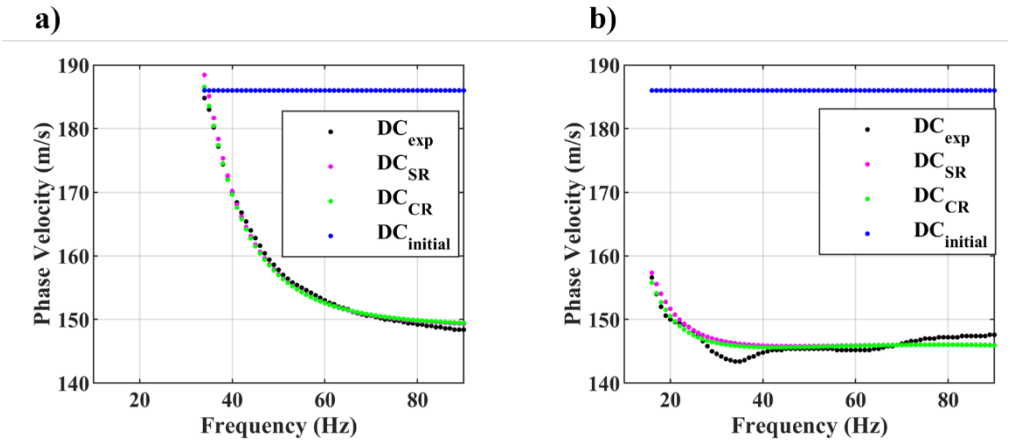

Figure 4.5. Examples of the estimated DCs with their corresponding simulated DCs at the first and last iteration of SWT inversion. The experimental DC is shown in black and the computed DCs from the straight- and curved-ray SWT are displayed in magenta and green, respectively. a) An example of a computed DC where the ray paths cross the high-velocity anomaly. The receiver pair are located at (15 m, 9 m) and (21 m, 11 m). b) The locations of the receivers in this case are at (15 m, 17 m) and (5 m, 17 m), and the ray paths between the receiver couple cross the low-velocity block.

As mentioned earlier, we impose very weak spatial regularization in our SWT inversions by setting the values of $\boldsymbol{C_R}$ equal to 10^6. To illustrate the impact of stronger regularization constraint on the inversion process, we perform another straight-ray SWT inversion where the VS difference between adjacent cells is set to 50 m/s (equivalent of setting $\boldsymbol{C_R}$ equal to 2500). The obtained VS model is compared with the true model and the VS model with weak regularization in Figure 4.6.

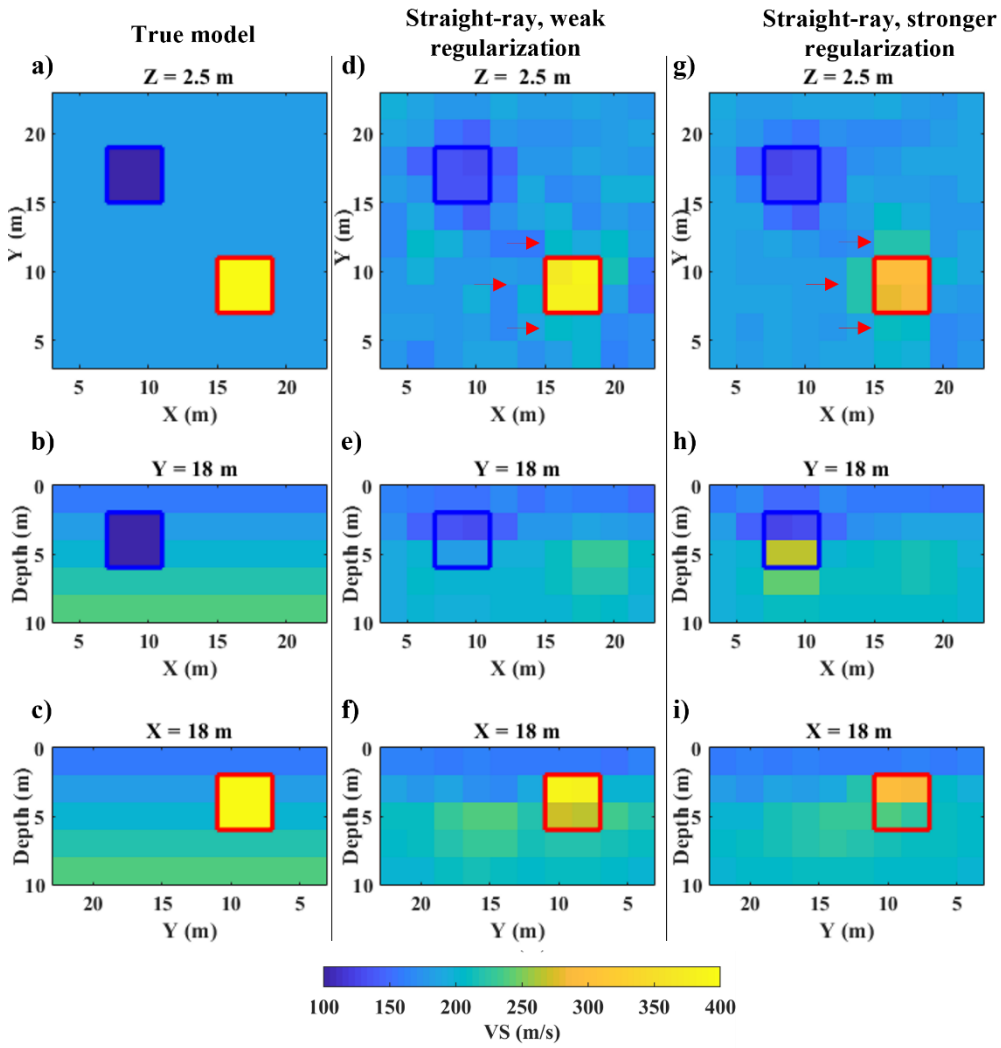

Figure 4.6. a) True VS model. The obtained VS model from straight-ray SWT inversion with: b) weak regularization constraint (C_R equal to 10^6), c) stronger regularization constraint (C_R equal to 2500). The red arrows show the difference between the smoothness of the velocity variation around the high-velocity block.

We see in Figure 4.6 that using a weak regularization constraint (Figure 4.6d-f) has retrieved the blocks of velocity anomaly and the area around them (shown as red arrows) more accurately than using a stronger constraint (Figure 4.6g-i). Therefore, in all the following examples, we carry out the inversion using a weak regularization.

4.2 Sand Bar model

To start the inversion process, we define an initial model with 10 layers where the VS values in all cells are 80 m/s. The inversion blocks are 2 m in horizontal dimensions and 1 m in the vertical dimension. We use the true VP and ρ values in the initial model. The parameters of the initial model are reported in Table 4.1. We set very weak spatial regularization by setting the values of the C_R equal to 10^6. In Figure 4.7, we display the values of the misfit function at different iterations of SWT inversions.

Table 4.1. The defined initial model for the SWT inversion

Layer	1	2	3	4	5	6	7	8	9	10
VS (m/s)	80	80	80	80	80	80	80	80	80	80
VP (m/s)	1700	1700	1700	1700	1700	1700	1850	1850	1850	1850
v	0.498	0.498	0.498	0.498	0.498	0.499	0.499	0.499	0.499	0.499
h (m)	1	1	1	1	1	1	1	1	1	1
ρ (kg/m^3)	1750	1750	1750	1750	1750	1750	1950	1950	1950	1950

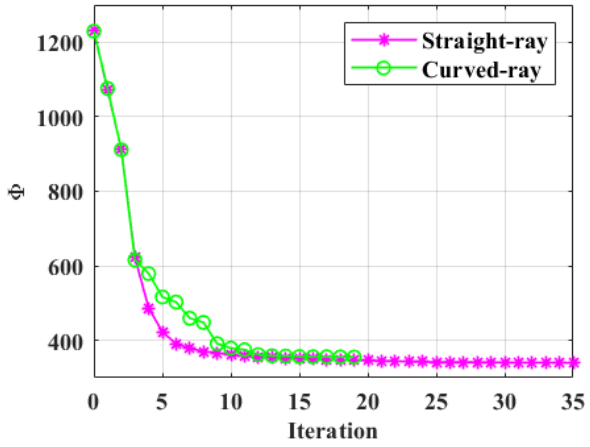

Figure 4.7. The values of misfit (Φ) at different iterations of the straight- and curved-ray SWT inversions.

We can see in Figure 4.7 that the misfit values are almost the same for both inversions until the 3rd iteration but after that the misfit from the curved-ray approach decreases with a lower rate than straight-ray. The inversion of the straight- and curved-ray SWT end at the 35th and 19th iteration, respectively. We show the obtained VS models at the last iteration of the straight-ray and curved-ray SWT inversions in Figure 4.8 with the boundaries of the target (sand layer) superimposed in red.

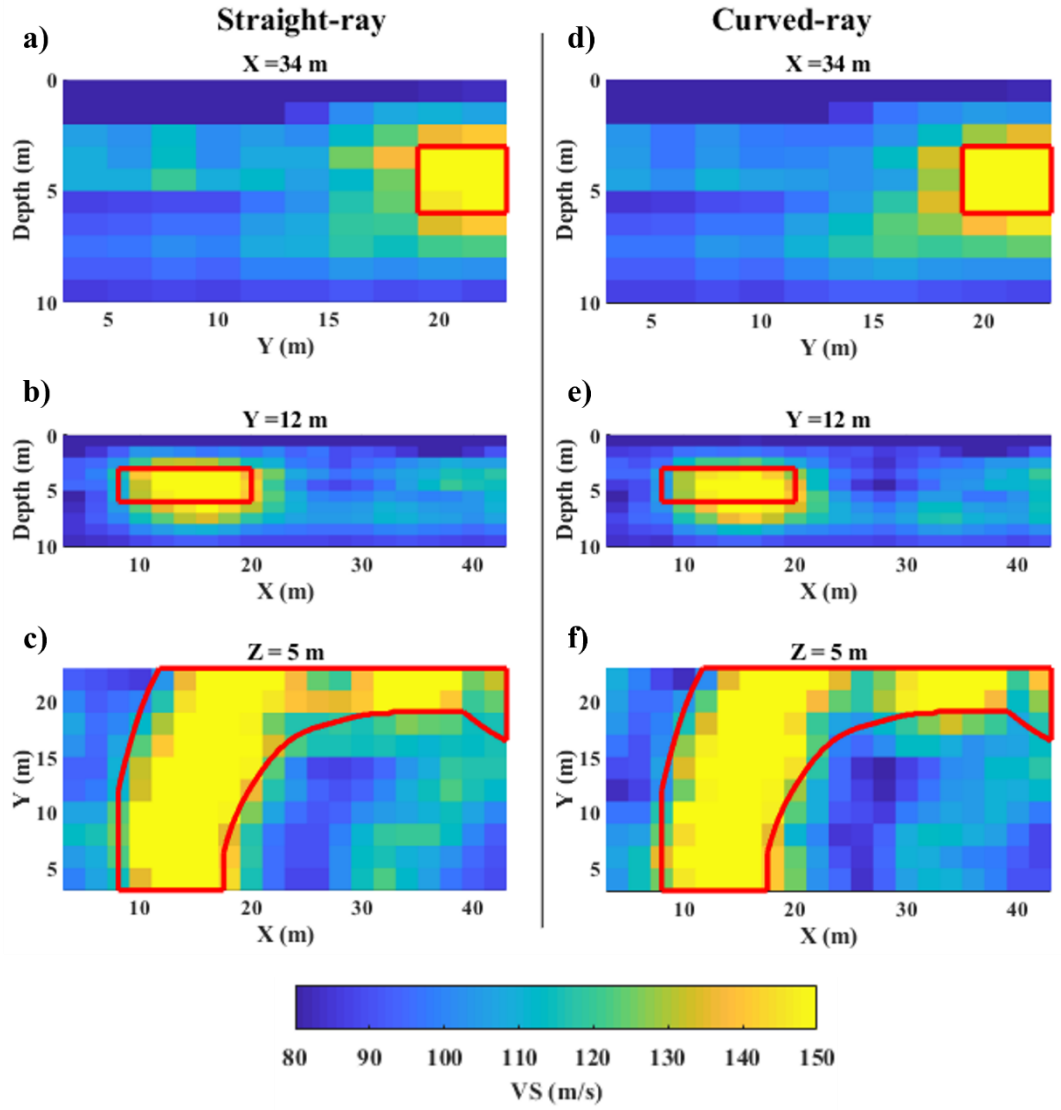

Figure 4.8. The obtained VS models at the last iteration of SWT inversion. The boundaries of the sand layer are superimposed in red. The 2D slices of the obtained VS model from the straight-ray SWT are shown at three slices: a) vertical slice at X=34 m, b) vertical slice at Y=12 m, c) horizontal slice at 5 m depth. The corresponding results for the curved-ray SWT are displayed at: d) vertical slice at X=34 m, e) vertical slice at Y=12 m, f) horizontal slice at 5 m depth. The colour bar that is shown at the bottom of the figure is the same for all subfigures

In Figure 4.8, we can see that both straight- and curved-ray approaches have properly located the sand layer. For each corresponding pair of the 2D slices in Figure 4.8, the computed VS models from the straight- and curved-ray SWT are very similar to each other. By comparing the obtained VS models from SWT

inversions (Figure 4.8) and the true VS model, we can qualitatively see that the computed models are close to the true model, having in mind that the inversion started from a vertically and horizontally homogeneous VS model. Using Equation 3.35, the computed e_m values for the straight-ray and curved-ray SWT are 15.80 % and 15.11%, respectively. The distribution of relative model misfits for the VS models from straight- (Figure 4.8a-c) and curved-ray SWT (Figure 4.8d-f) is shown in Figure 4.9.

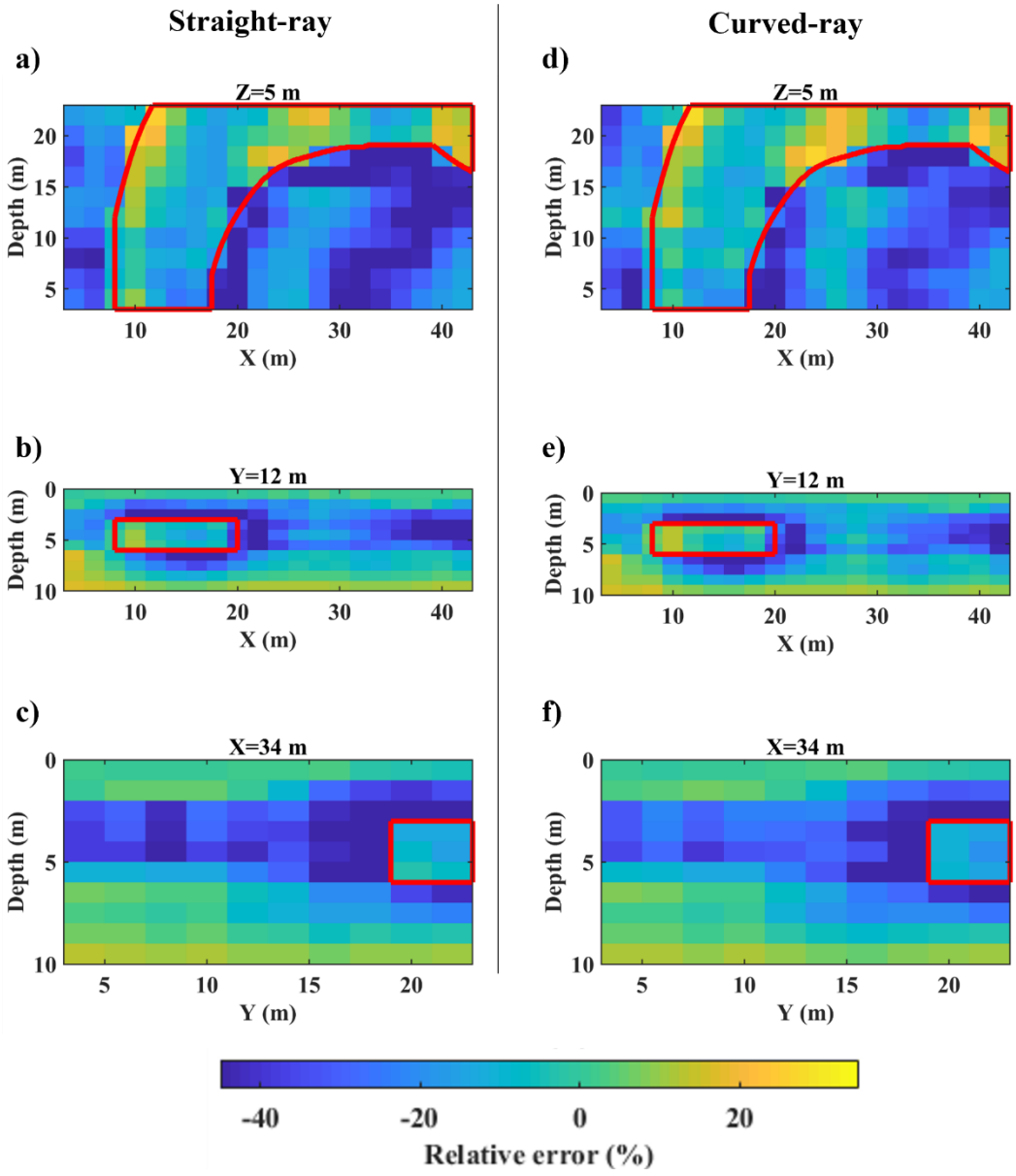

Figure 4.9. Distribution of model misfits at the last iteration of the inversion of straight-ray (subfigures a-c) and curved-ray SWT (subfigures d-f). The boundaries of the target are superimposed in red. All subfigures have the same colour scale which is shown at the bottom of the figure.

The computed value of e_d at the last iteration of straight- and curved-ray SWT is 1.12 % for both approaches. We show the spatial distribution of computed e_c (Equation 3.34) from the straight- and curved-ray SWT (at their last iteration) in

Figure 4.10. For each DC, we compute the average relative misfit and assign it to the mid-point between the receiver pair.

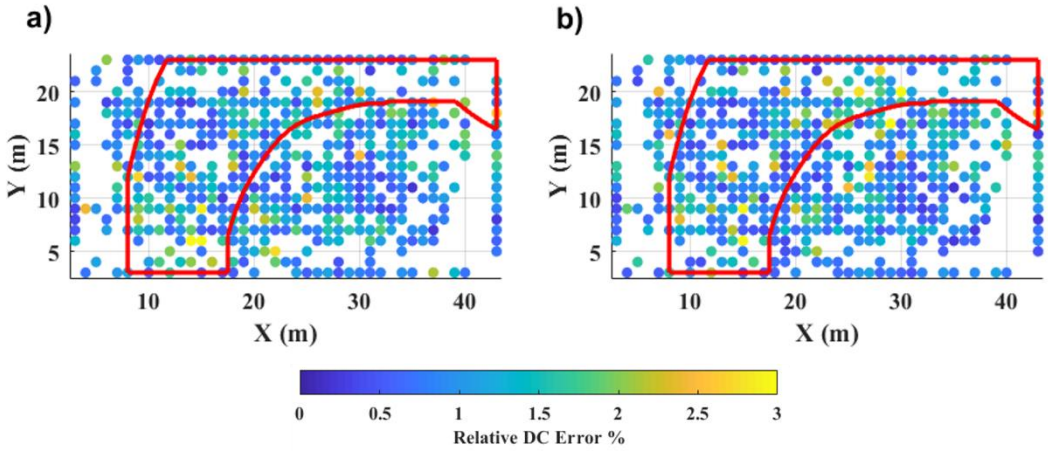

Figure 4.10. The obtained spatial distribution of the local misfit between the experimental DC and the simulated DC (e_c) from the last iteration of a) straight-ray, b) curved-ray SWT. The external boundaries of the sand channel are superimposed in red.

We can see that both straight-ray (Figure 4.10a) and curved-ray (Figure 4.10b) approaches have produced very low final data misfits. The misfit of the DCs from the straight-ray and curved-ray are below 1 % for most of the DCs (52 % for the straight-ray and 53% for the curved-ray). In Figure 4.11, we display two examples of the experimental DCs together with the computed DCs at the last iteration of straight- and curved-ray SWT inversions. The ray paths between the receiver pair in the first example (Figure 4.11a) travel through the sand channel, but in case of the second example (Figure 4.11b) the rays do not pass the sand channel.

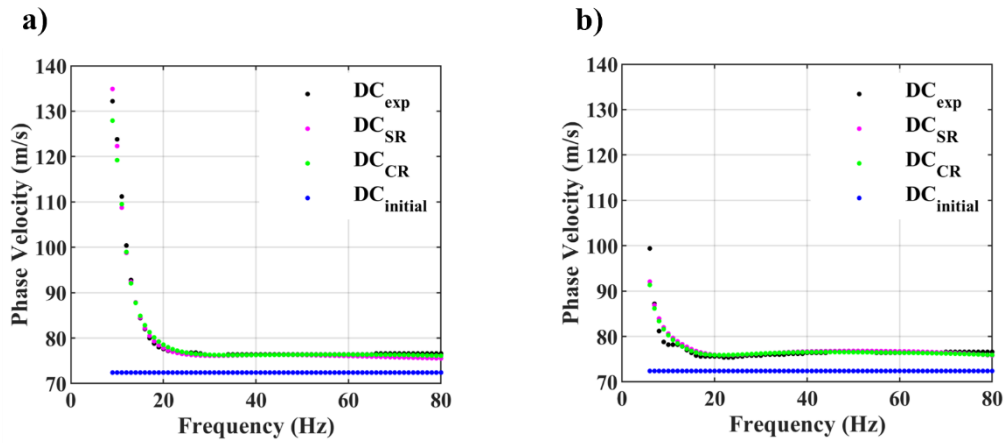

Figure 4.11. Two examples of DCs fittings at the first and last iterations of the straight-ray and curved-ray SWT inversion. The experimental DCs are shown in black, the initial DC is displayed in blue, and the computed DCs from the straight- and curved-ray SWT are displayed in magenta and green, respectively. a) The experimental and simulated DCs for the receivers that are located at (7 m, 13 m) and (15 m, 5 m). b) An example of an estimated DC where the ray paths between the receivers do not cross the sand layer. The locations of the receiver couple are at (21 m, 3 m) and (41 m, 3 m).

We can see in Figure 4.11 that the misfit between the simulated and experimental DCs are very low in both examples. For the DCs in Figure 4.11a, the average relative misfit for the straight- and curved-ray are 0.56 % and 0.45 %, respectively. These misfit values for the second example (Figure 4.11b) are 0.72 % and 0.58 % for the straight- and curved-ray.

4.3 Pijnacker field

We start the inversion from a 6-layer model where the horizontal dimensions of each cell are 2 m, and the vertical size increases from 1 m to 3 m. The VS is set to 60 m/s in all cells, VP is equal to 200 m/s and ρ is 1700 kg/m^3 for all cells. Also in this case, we damp the impact of the spatial regularization by setting the values of C_R to 10^6. The values of misfit function at different iterations of the SWT inversions are depicted in Figure 4.12. We show three slices of the obtained VS models from the straight- and curved-ray SWT in Figure 4.13.

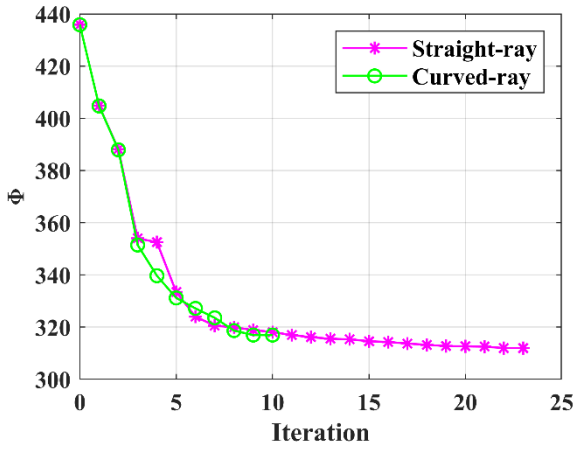

Figure 4.12. The misfit values at different iterations of the straight-ray and curved-ray SWT.

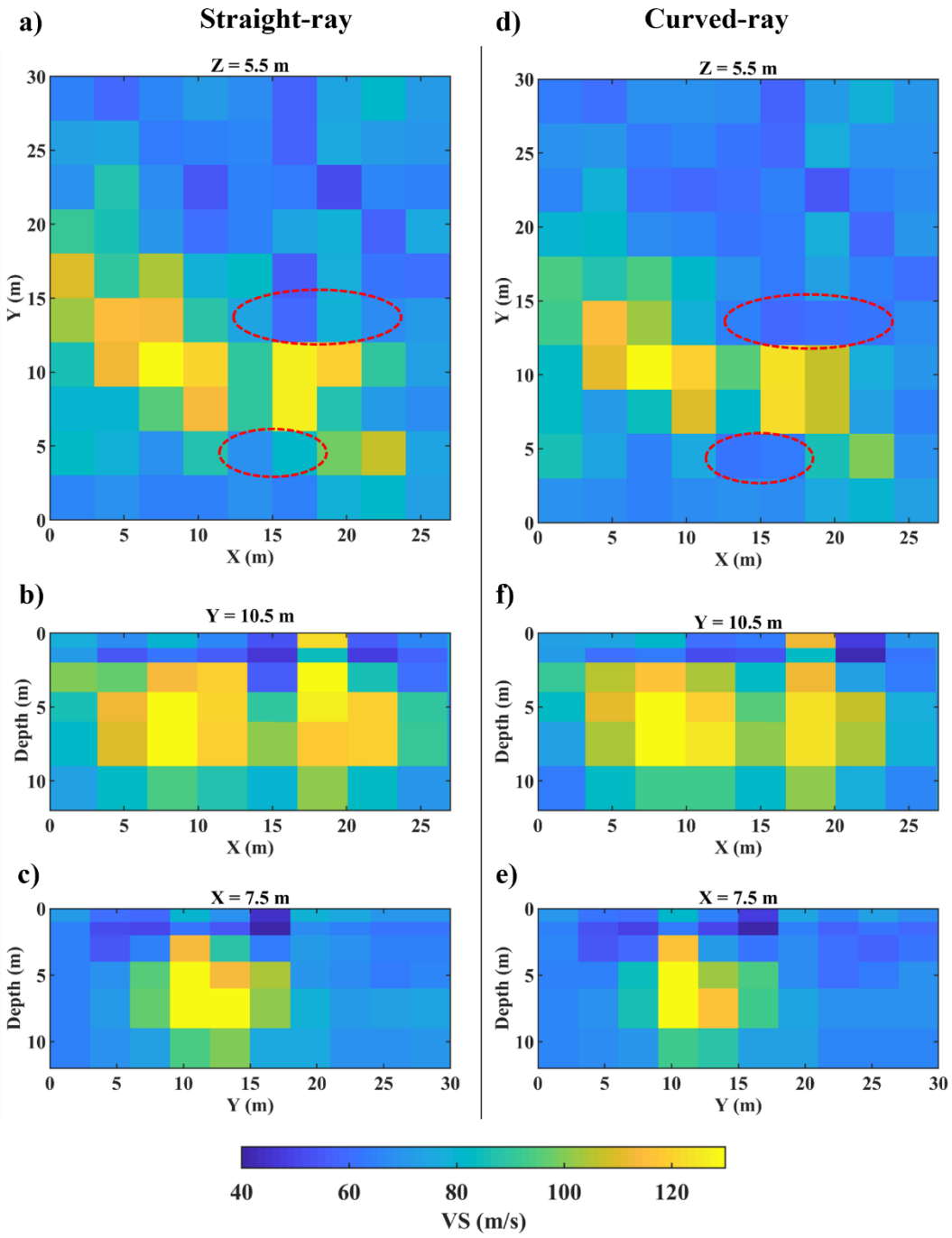

Figure 4.13. The VS models from the last iteration of SWT inversion. The slices of the VS model from the straight-ray SWT are shown at: a) Z=5.5 m, b) Y=10.5 m, and c) X=7.5 m. The 2D slices of the VS model from the curved-ray SWT are displayed at: d) Z=5.5 m, e) Y=10.5 m, and f) X=7.5 m. Some areas where the difference between the straight- and curved-ray SWT are clearer are shown in dashed red. The colour scale shown at the bottom of the figure applies to all plots.

In Figure 4.13, we can see that the VS models from the straight-ray (Figure 4.13a to c) and curved-ray (Figure 4.13d to f) do not differ significantly. We can see in the horizontal sections that the VS values at the grid cells around the high-velocity portion (shown in dashed red) are better retrieved in the curved-ray (Figure 4.13d) than the straight-ray (Figure 4.13a).

We show the available well data close to the Pijnacker field in Figure 4.14. We can see in Figure 4.14 that the medium mainly consists of clay with peat and sand in some locations. A previous 2D full waveform study (Bharadwaj et al., 2017) on a clay-field close to the Pijancker field, produced a VS model in range of 40-80 m/s up to 15 m depth. This agrees with the inversion results shown in Figure 4.13. The high velocity portions of the retrieved model in Figure 4.13 relate to the sand. We see in the vertical slices (Figure 4.13b, c, e, and f) that the depth of the high-velocity portion (sand layer) is mainly in range of 2-9 m which seems reasonable given the a priori well data (Figure 4.14).

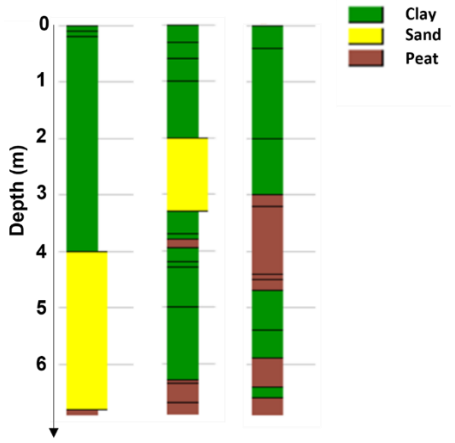

Figure 4.14. The available well data near to the Pijnacker field

The computed values of e_d for the straight-ray is slightly less than the curved-ray SWT (9.25 % against 9.81 %). In Figure 4.15, we display the computed misfits between the experimental and the simulated DCs as a function of location.

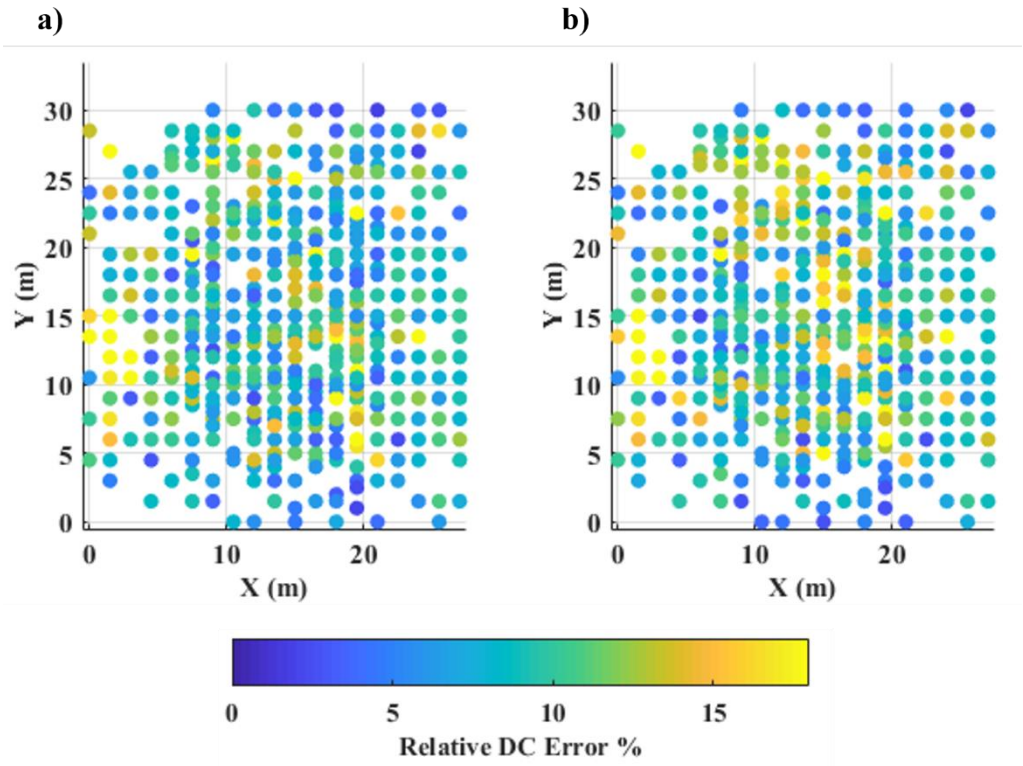

Figure 4.15. Spatial distribution of misfit between the experimental and simulated DCs (e_c) at the last iteration of a) straight-ray, b) curved-ray SWT.

We can see that the DCs misfits for the straight-ray (Figure 4.15a) are slightly lower than curved-ray (Figure 4.15a). We show two examples of the fittings of the DCs in Figure 4.16.

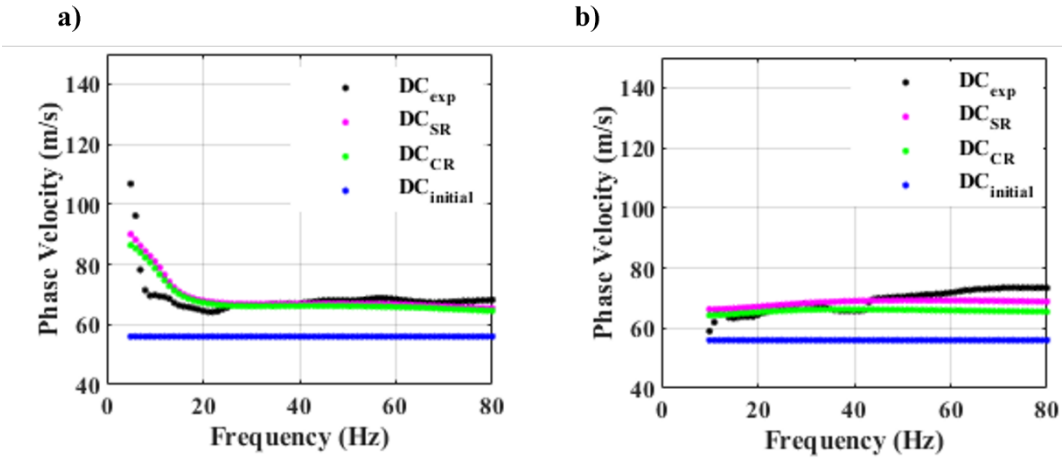

Figure 4.16. Two examples of the experimental DCs and the computed DCs at the first and last iterations of the inversions. a) The locations of the receiver pair are at (24 m, 12 m) and (18 m, 21 m). b) The receivers are located at (15 m, 6 m) and (3 m, 15 m).

The computed average misfits for the straight- and curved-ray in Figure 4.16a are 3.72 % and 5.24 %, respectively. The corresponding misfit values for the DCs in Figure 4.16b are equal to 3.55 % and 4.00 %, respectively.

4.4 CNR field

As the initial model for the inversion, we define an 8-layer 3D model where the horizontal and vertical sizes of each cell is 0.5 m. The initial VS value is set to 200 m/s in all cells, the initial VP is equal to 400 m/s and ρ is 2000 kg/m^3 for the first four layers and 2100 kg/m^3 for the deeper layers. Figure 4.17 displays the values of misfit function at different iterations of the straight- and curved-ray SWT inversions.

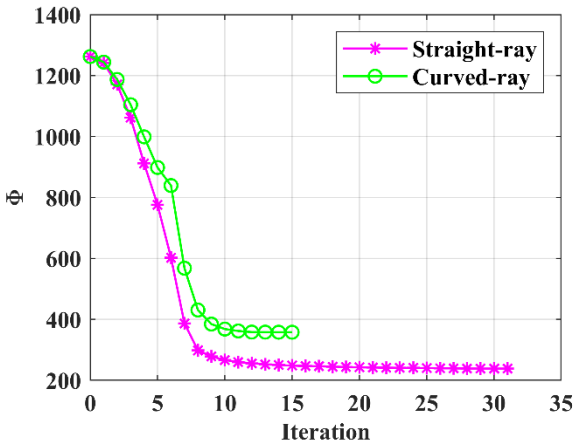

Figure 4.17. The computed values of misfit function (Φ) at different iterations of the straight-ray and curved-ray SWT inversions.

We can see in Figure 4.17 that the curved-ray converges faster than straight-ray (15 against 31 iterations), but its final misfit Φ is higher than the straight-ray (357 against 238). We can also see that the curved-ray has a higher misfit than the straight-ray for all iterations. In Figure 4.18, we show the final VS models from the straight-ray (Figure 4.18a to c) and curved-ray (Figure 4.18d to f) SWT inversions at their last iterations. The red arrows in Figure 4.18a and c mark the locations of the corresponding 2D slices.

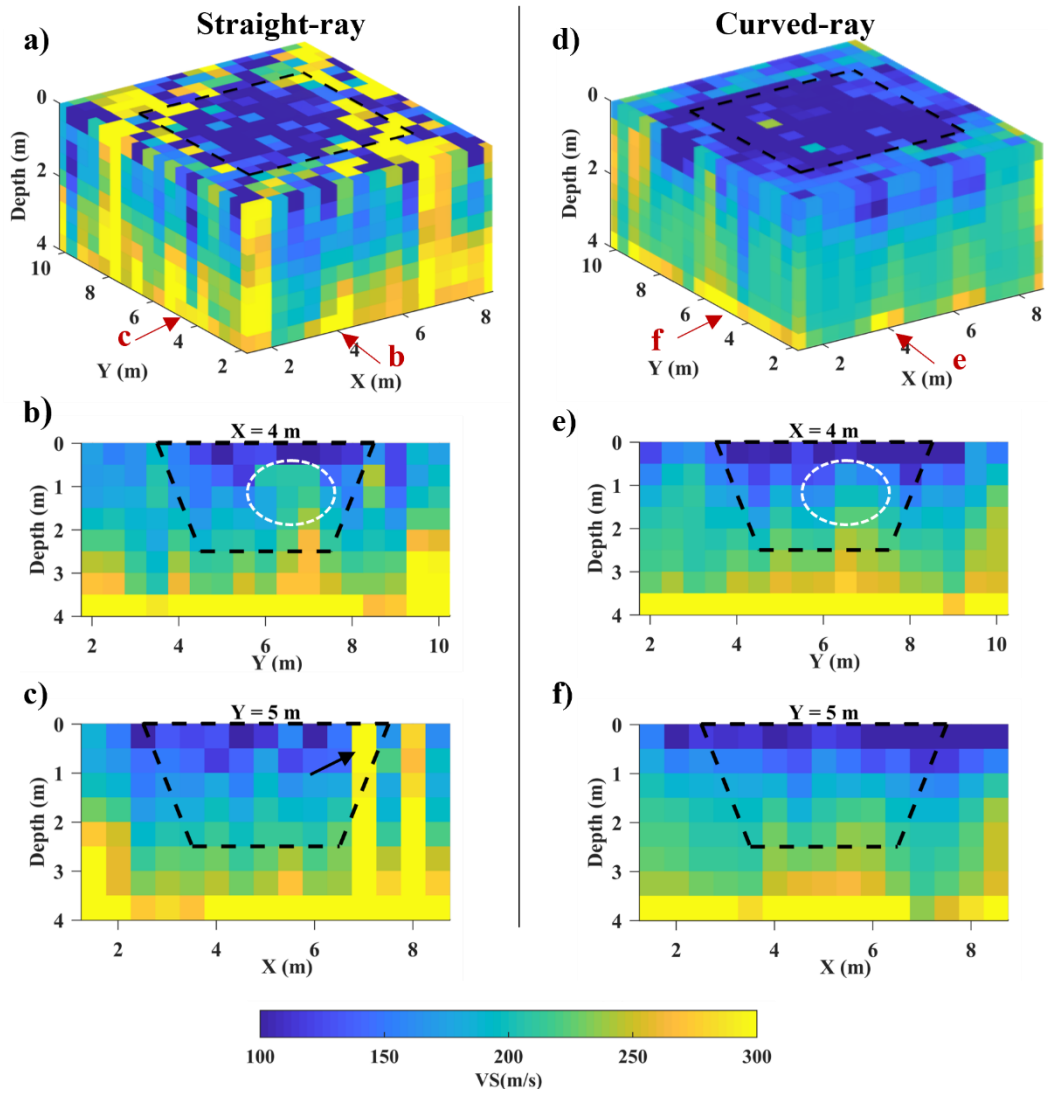

Figure 4.18. The VS models from the straight-ray (a-c) and curved-ray (d-f) SWT. The boundaries of the loose sand body are superimposed in dashed black. a) The 3D view of the VS model from the straight-ray SWT. The two arrows (b and c) correspond to the vertical slices that are shown in subfigures (b-c). b) The vertical slice from the straight-ray SWT at X=4 m. c) The VS model from the straight-ray SWT at Y=5 m. d) 3D VS model from the curved-ray SWT. The two arrows correspond to the vertical slices in subfigures (e-f). e) The vertical slice from the curved-ray SWT at X=4 m. f) The vertical slice at Y=5 m for the obtained VS model from the curved-ray SWT.

Figure 4.18 shows that the difference between straight- and curved-ray models are more pronounced in this example. There are some cells with relatively high velocity values inside the sand body in the model obtained from the straight-ray

(Figure 4.18a). The boundaries of the loose sand body at the surface are better retrieved by the curved-ray SWT (Figure 4.18d). The area shown in dashed white in Figure 4.18b and Figure 4.18e displayed that the gradual increase of the VS values with depth inside the sand body is clearer in the model from the curved-ray (Figure 4.18e) than the straight-ray (Figure 4.18b). The arrow in Figure 4.18c shows the high velocity cells inside the loose sand body in the retrieved model from the straight-ray SWT. This artefact does not exist in the corresponding slice from the curved-ray SWT (Figure 4.18b).

The obtained e_d using Equation 3.33 for the straight- and curved-ray SWT are 4.40 % and 7.21 %, respectively. Figure 4.19 shows the spatial distribution of the computed misfit between the experimental DC and the simulated DCs. In Figure 4.19, we see that the calculated misfits from the curved-ray are higher than straight-ray SWT, especially for the DCs with mid-points inside the sand body. We display two examples of the fittings of the DCs in Figure 4.20.

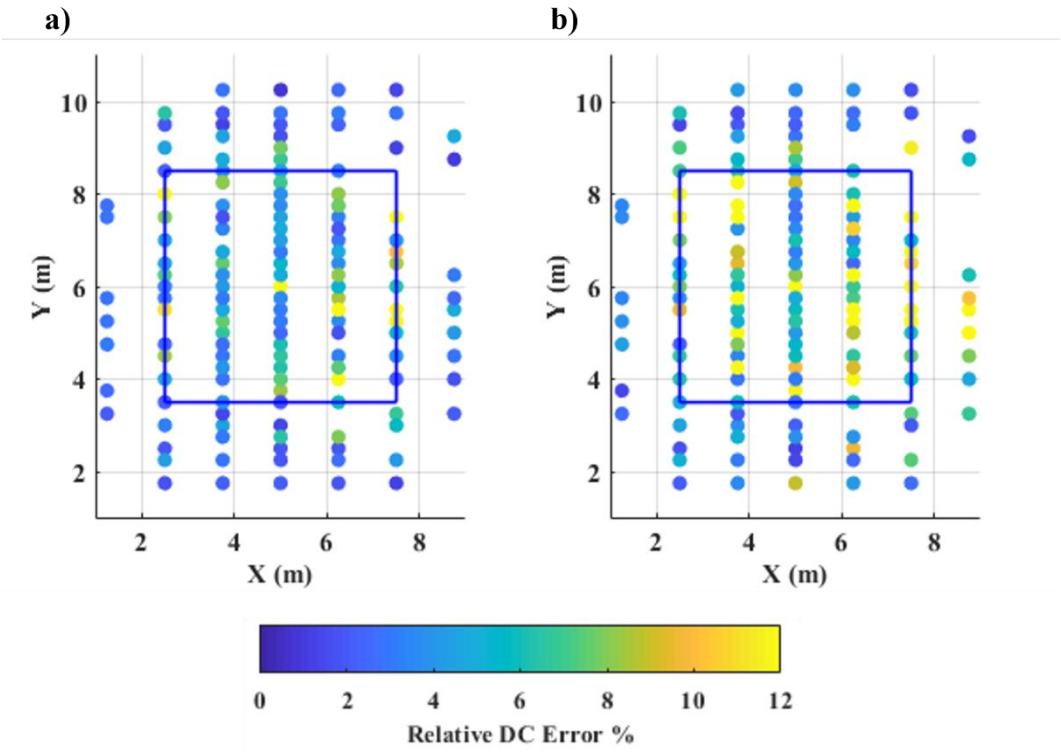

Figure 4.19. The maps of misfit between the experimental DCs and the simulated DCs (e_c) at the last iteration of a) straight-ray, b) curved-ray SWT. The blue lines represent the boundaries of the loose sand body at the surface.

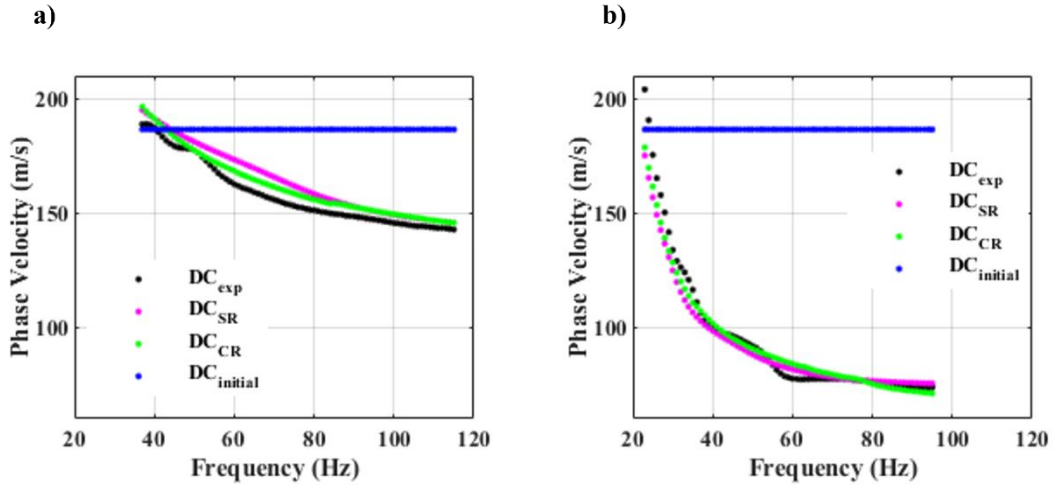

Figure 4.20. Examples of the estimated DCs with the corresponding fittings from the first and last iteration of inversion. The experimental DC is shown in black, the DC at the first iteration of inversion is shown in blue, and the computed DCs from the last iterations of straight- and curved-ray SWT are displayed in magenta and green, respectively. a) An example of a computed DC where the path between the receivers does not cross the sand body. The receiver pair are located at (6.25 m, 9.75 m) and (3.75 m, 9.75 m). b) The path between the receiver couple crosses the sand body. The locations of the receivers are (6.25 m, 5.25 m) and (3.75 m, 4.75 m).

In Figure 4.20a, both receivers are located outside the sand body and the relative misfits for the straight- and curved-ray approaches are 3.58 % and 3.50 %, respectively. For the experimental DC shown in Figure 4.20b, both receivers are located inside the sand body and average DC misfits for the DCs from the straight- and curved-ray are 3.86 % and 2.63 %.

4.5 Discussion

So far in this chapter, we have shown the SWT inversion results for four 3D examples. There are some points to be noted to have a clearer comparison between the straight-ray and curved-ray SWT. We divide our analysis into four subsections:

- the ray paths,
- the data misfits, model misfits and computational cost,
- the impact of data coverage,

- and the role of data weighting.

4.5.1 ray paths

We have shown the improvement of the model by using the curved-ray with respect to straight-ray SWT in the numerical and real world examples. This improvement was more pronounced particularly at the boundaries of the velocity anomalies. We show several examples of the computed ray paths at the last iteration of the curved-ray SWT for the Sand Bar model, the Blocky model, and the CNR field in Figure 4.21.

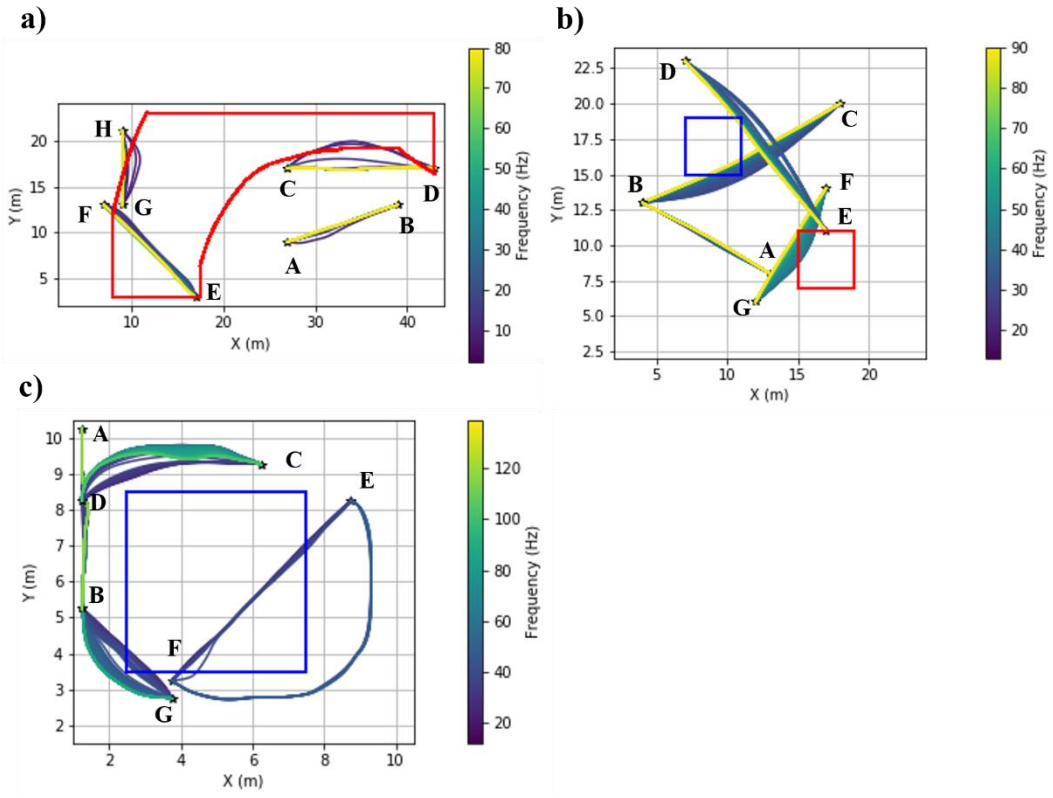

Figure 4.21. Examples of the computed ray paths at the last iteration of the curved-ray SWT inversion for: a) the Sand Bar model, b) the Blocky model, c) the CNR field. The boundaries of the low- and high-velocity anomalies are shown in blue and red, respectively. The receiver locations are labelled as A-H.

In all the three models in Figure 4.21 the receivers A and B are located outside the velocity anomalies, and we see that the computed ray paths between them do not cross the anomalies. Therefore, the obtained paths do not deviate considerably from straight lines. In Figure 4.21a, the high-velocity anomaly exists at the depth

range of 3-6 m. Hence, we can see that the high-frequency components of the DCs, which correspond to the shallow parts of the model, do not deviate from straight lines. However, the lower frequencies (i.e., higher wavelengths) for the C-D and G-H pairs have deviated from straight lines and travelled through the high-velocity parts. In Figure 4.21b, the depth of velocity anomalies is in range of 2 m to 6 m. We see that also in this case the ray paths for higher frequencies have almost no deviations from straight lines since they do not cross the anomalies. However, we can see for the obtained paths between B-C and D-E pairs that the lower frequencies have bypassed the low-velocity anomaly. Similarly, lower-frequencies in case of the G-F pair have deviated from straight paths and travelled through the high-velocity anomaly. In Figure 4.21c, the sand body (low-velocity anomaly) starts at the surface and reaches down to 2.5 m depth. Its area shrinks from (5 m × 5 m) at the surface to (3 m × 3 m) at 2.5 m depth. The shrinkage in size of the anomaly can be seen in the computed path for the B-G, C-D, and E-F pairs, where the degree of the deviation from the straight line decreases as the depth increases (frequency decreases).

We have not shown the computed ray paths for the Pijnacker field in Figure 4.21, because the exact boundaries of the anomaly (sand channel) are unknown. Nevertheless, the computed ray paths can provide helpful insights. For instance, the computed ray paths from straight- and curved-ray SWT, for the DCs data with the wavelengths in range of 6-9 m are displayed in Figure 4.22. Since the initial VS model is vertically and horizontally homogeneous, the initial ray paths for both straight- and curved-ray SWT are straight lines. As shown in Figure 4.22a, the ray paths do not change during the inversion in the straight-ray approach. However, the paths are updated at every iteration of the curved-ray SWT inversion. We see that some areas in Figure 4.22b (shown in dashed red) are bypassed by almost all the rays even though the data coverage of these areas in the straight-ray approach (Figure 4.22a) is considerably high. Therefore, these portions are likely to correspond to the low velocity materials, i.e., clay and peat. The area between these low-velocity portions has both higher concentration of ray paths and higher average phase velocity values. Therefore, they probably show the sand layer. These locations agree with the obtained VS model from the curved-ray SWT inversion (Figure 4.13d).

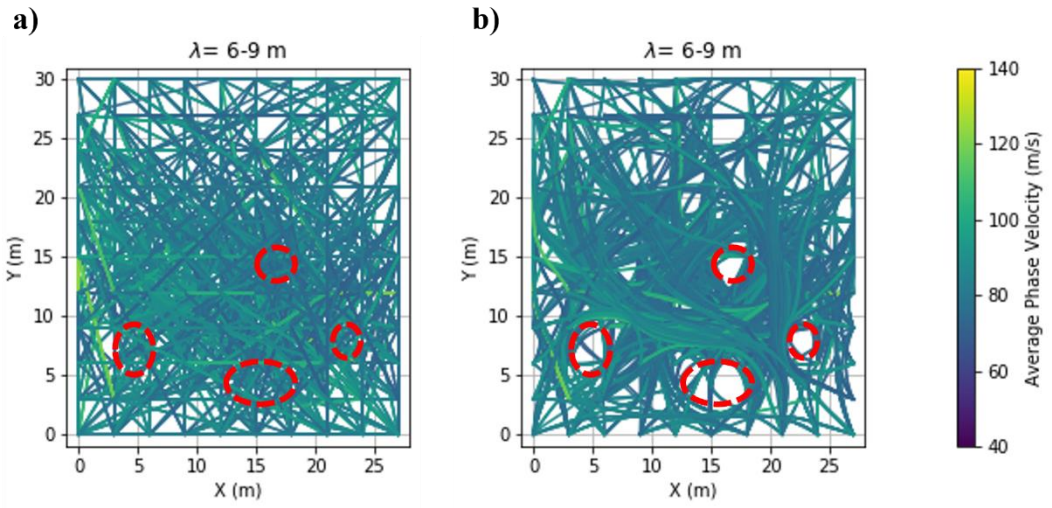

Figure 4.22. The computed ray paths for the data with wavelengths in range of 6-9 m for the Pijnacker field at the last iteration of a) straight-ray, b) curved-ray SWT. The different colours correspond to the computed path-average phase velocity between receiver pairs. The areas marked with dashed red show low-velocity portions which are more visible in the obtained model form the curved-ray SWT.

4.5.2 Data misfits, model misfits, and computational cost

In this part, we compare the results of the straight-ray and curved-ray SWT quantitatively. We have reported the following parameters in Table 4.2:

- n_{dc} : the number of the input DCs,
- n_i : the number of iterations to reach the stopping criteria,
- r_t : the spent time to run all the iterations of the inversion. It should be noted that the simulations have been performed on 40 cores on a shared memory cluster,
- $mem_{\max}$: the maximum memory consumption during the inversion process,
- e_d : the relative data misfit at the last iteration of the inversion computed from Equation3.33,
- e_m : the relative model misfit at the last iteration of the inversion using Equation 3.35,
- e_t : the computed relative model misfit (Equation 3.35) only for the depth range of the target,
- *CI*: the normalised cost of the inversion to be run. The cost depends on the needed memory and the running time. We computed the *CI* at Microsoft

cloud service (Azure) but since the cost value can change at different times, we normalise the obtained *CI* values to the *CI* of the straight-ray SWT.

Table 4.2. The comparison of the straight-ray and curved-ray SWT.

Straight	Curved	Sand Bar		Blocky		CNR		Pijnacker		Average	
n_{dc}		1207		921		315		972		-	
n_i		35	19	16	20	31	15	23	10	1.00	0.72
r_t (hr)		15.17	18.99	3.13	6.1	1.97	1.70	8.31	7.74	1.00	1.25
mem_{max} (GB)		17.25	18.41	2.85	3.85	3.89	3.94	40.35	40.41	1.00	1.11
e_d (%)		1.12	1.12	0.99	0.99	4.40	7.21	9.25	9.81	1.00	1.18
e_m (%)		15.80	15.11	8.71	8.48	-	-	-	-	1.00	0.98
e_t (%)		23.19	20.36	9.74	9.23	-	-	-	-	1.00	0.96
Cost		1.00	1.25	1.00	1.95	1.00	0.86	1.00	0.93	1.00	1.25

It should be noted that we have computed e_m only for the synthetic examples (Sand Bar and Blocky models), where the true velocity models are known. The valued in the last column in Table 4.2 are unitless. For each parameter in that column, we sum the values from straight- and curved-ray SWT. We normalise them to the value of the straight-ray SWT and report the obtained results in the last column in Table 4.2. In this way, the average values for the straight-ray SWT are always one and we can see the relative change if the curved-ray is used instead of the straight-ray.

We can see in Table 4.2 that in all examples except for the Blocky model, curved-ray SWT has converged in less iterations than the straight-ray. However, the curved-ray SWT has increased r_t by 25 % compared to straight-ray. For all cases, curved-ray SWT needed more memory (11 % by average) than straight-ray. In terms of data misfit (e_d), straight-ray approach has provided better performance than the curved ray and it has a lower e_d value in all examples in Table 4.2. We can also see that the difference between the obtained e_d values from the straight- and

curved-ray SWT is negligible in case of the synthetic examples (the Sand bar and Blocky models), but the difference is more pronounced for the field examples (the CNR and Pijnacker). Despite having higher e_d, the curved-ray approach has produced lower model misfits than straight-ray. Using curved-ray SWT has decreased the overall model misfit (e_m) and the target model misfit (e_t) by 2 % and 4 %, respectively. We see in Table 4.2 that using curved-ray SWT has increases the computational cost by an average of 25 %. It means that by average, to have 1 % improvement of the model using curved-ray SWT, the computational cost increase by 12.5 %.

4.5.3 Impact of the data coverage

In all the examples that we presented in this chapter, the computed VS models from the straight-ray and curved-ray SWT do not differ significantly except for the CNR field. The reason for this difference can be the low data coverage, particularly in the shallower portion of the medium. Figure 4.23 depicts the ray paths of the DCs data with the wavelengths in range of 0-1 m.

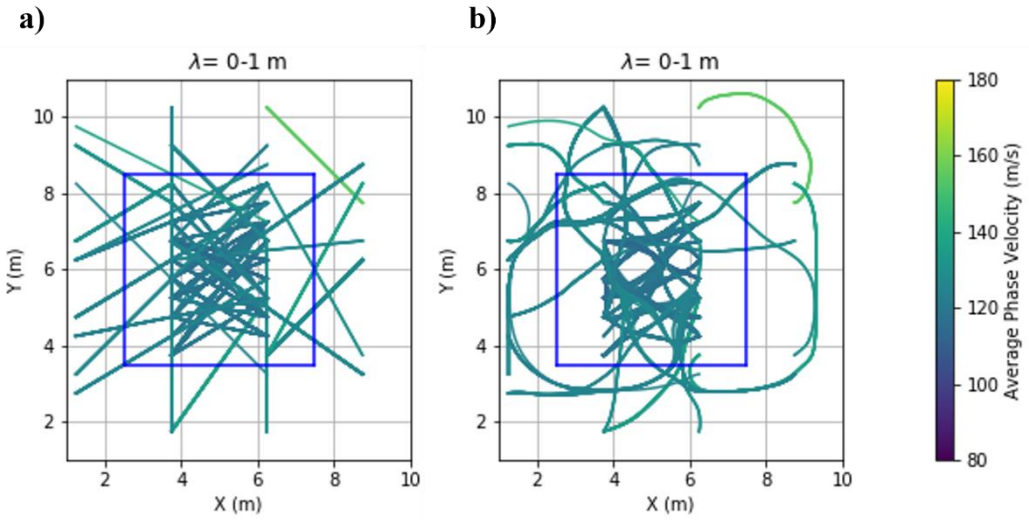

Figure 4.23. The ray paths for the data points with wavelengths in range of 0-1 m from: a) the last iteration of the straight-ray, b) the last iteration of curved-ray SWT inversion. The boundaries of the sand body at the surface are superimposed in blue. The colours of ray paths correspond to the computed path-averaged phase velocity along the path.

We can see in Figure 4.23a that some areas of the medium are not covered with straight-rays, especially outside the sand body. It should be noted that for both

cases, the ray paths at the first iteration are straight lines since the initial model has a constant VS value for all cells.

The lack of high data coverage is less critical for the Sand Bar model, the Blocky model, and Pijnacker field. This is because we have optimised the source locations for the Sand Bar model, Blocky model, and the Pijnacker field to ensure high data coverage (as discussed in Chapter 2), but the CNR dataset had been acquired using a classical cross-spread acquisition layout which is typical for 3D exploration schemes, and the shot positions had not been optimised for a 3D SWT study. As a result, even though the number of source positions in this case (83 shot positions) is more than other three examples, the obtained DC coverage is lower than them. As we can also see in Table 4.2, the number of estimated DCs for the CNR dataset is also less than the others.

4.5.4 Data weighting

Uneven sampling of DC data in terms of wavelength can be problematic. In case of the Pijnacker field, while the available well data suggest that the depth of the target (sand layer) is expected to vary in range of 2-7 m, most of the extracted DC data (81 %) have wavelengths less than 3 m. This can be a serious problem since the inversion might reach the stopping criteria without any significant updates in the deeper portion of the initial velocity model. To address this issue, we used a wavelength-based weighting scheme suggested by Khosro Anjom and Socco (2019) to compensate for the non-uniform sampling of the DC data in terms of wavelength. In this weighting method, the weight of the i^{th} data point of the j^{th} DC is computed as:

$$w_{i,j} = \frac{\Delta\lambda_{i,j}}{\Delta\lambda_{j,\max}}, \qquad 4.1$$

where $\Delta\lambda_{i,j}$ represents the wavelength distance between the data point *i* and its closest data point. In this way, the data points with larger wavelengths get higher weights. The obtained weights are then normalised to the maximum computed wavelength $\Delta\lambda_{j,\max}$. Finally, the computed weights are incorporated in the data covariance matrix ($C_{\exp}$) as:

$$C_{\exp} = \begin{pmatrix} \frac{\sigma_{1,1}^2}{w_{1,1}} & & 0 \\ & \ddots & \\ 0 & & \frac{\sigma_{i,j}^2}{w_{i,j}} \end{pmatrix} \qquad 4.2$$

where $\sigma_{i,j}$ is the standard deviation of the ith data point of the jth DC. Then, the modified data covariance matrix is used in Equation 3.11 to update the model iteratively. In Figure 4.24, we show the obtained VS models with (Figure 4.24 a and b) and without (Figure 4.24 c and d) the wavelength-based weighting at 5.5 m depth.

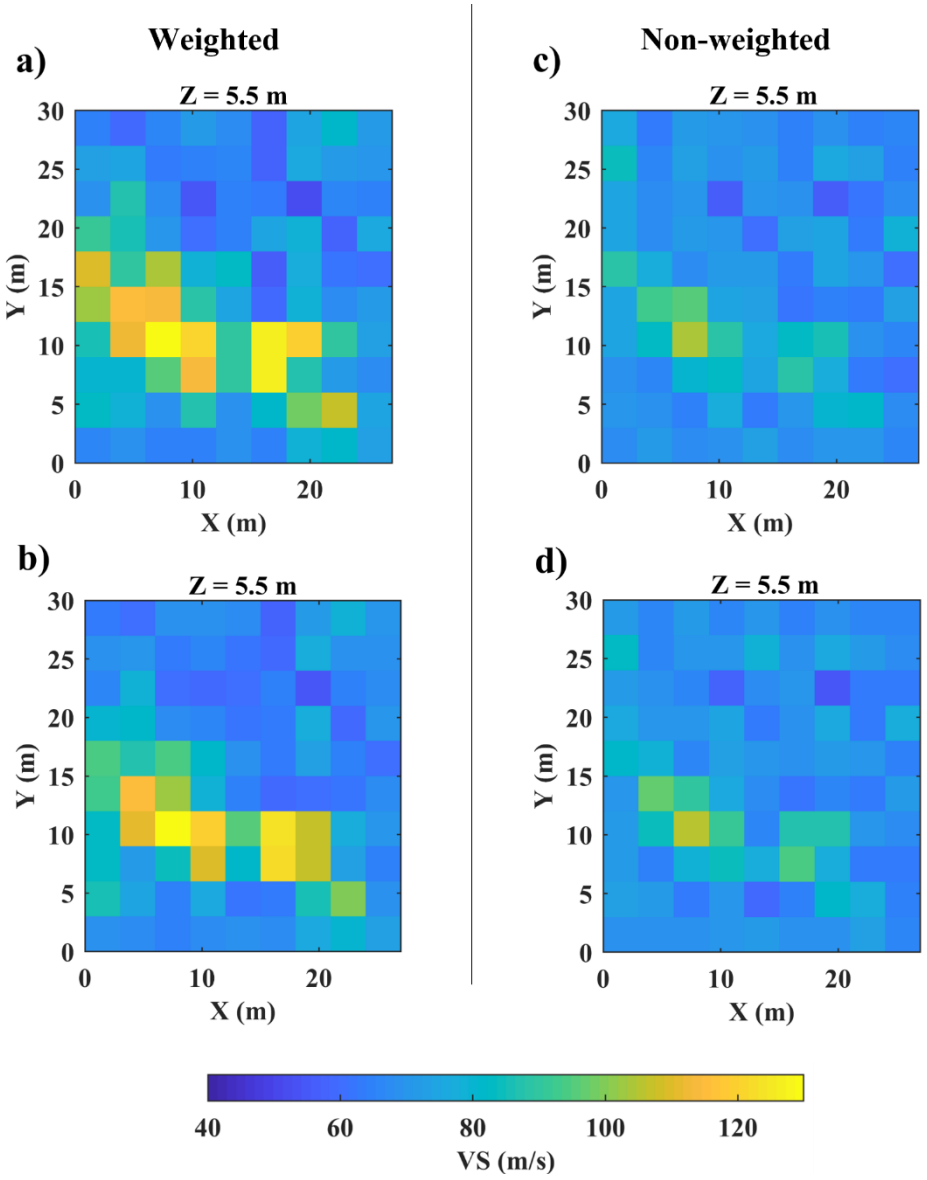

Figure 4.24. The impact of weighting on the SWT inversion results. The computed VS model at the depth of 5.5 m from: a) weighted straight-ray, b) weighted curved-ray, c) non-weighted straight-ray, d) non-weighted curved-ray SWT.

We can see the improvement of the retrieved VS model after applying the wavelength-based weighting method in Figure 4.24. We see this improvement for both straight-ray (Figure 4.24a) and curved-ray SWT (Figure 4.24b). The VS models from the non-weighted SWT inversions (Figure 4.24 c and d) have barely retrieved any pattern to locate the target (sand layer), whereas the sand layer can be seen clearer in the models from the weighted inversions (Figure 4.24 a and b).

4.6 Conclusions

We have applied SWT to four datasets and built near-surface VS models. We have compared the obtained results from the straight-ray and curved-ray SWT in terms of data misfit, model misfit, and computational cost. We showed that compared to the straight-ray approach, using curved-ray SWT improves the accuracy of the computed VS model. We illustrated that the acquisition layout can play an important role in the obtained data coverage and consequently in the inversion results. We showed that the classical cross-spread acquisition layout (which was used in the CNR example) may not provide high DC coverage. In this case, the improvement of inversion results from curved-ray SWT can be significant. We also showed that in case of high data coverage, which can be achieved by optimisation of source positions, the difference between the obtained VS models from the straight-ray and curved-ray can be very small even in the presence of high lateral variation of the velocity. By analysing the results from our four datasets, we also showed that by average, using curved-ray SWT leads to a considerable increase of the computational cost.

Chapter 5

Joint inversion of surface and body wave tomography[2]

In this Chapter, we apply joint inversion of SWT and BWT, which was described in Section 3.2, to three 2D and one 3D datasets. The 2D examples consist of the Step model, the Pijnacker field, and the CNR field. Then, we apply the joint inversion algorithm to CNR 3D dataset. For each example, we compute VP, VS, and ν models from both the individual and joint inversions and compare the results.

5.1 Step model

The true VS, VP, and ν distribution of the Step model are shown in Figure 2.1. To start the inversion process, we define a laterally homogeneous model (Table 5.1). Both individual and joint inversions start from the same initial model and a very weak regularization is applied by setting $\mathbf{C_R}$ to 10^6.

[2] Most of this chapter is based on the following paper:
Karimpour, M., Slob, E.C., and Socco, L.V., 2022, Physically constrained 2D joint inversion of surface and body wave tomography, Journal of Environmental and Engineering Geophysics, 27(2), 57-71, doi: 10.32389/JEEG21-031.

Table 5.1. Geophysical parameters of the initial model.

Layer	*VS* (m/s)	*VP* (m/s)	*h* (m)	ρ (kg/m^3)
1	200	300	3	2000
2	300	600	6	2100
Half-space	500	930	-	2200

Since the number of data points is different in SWT, BWT, and the joint inversion of SWT and BWT, we define the normalised misfit value as:

$$\Phi_{norm} = \Phi/n_d, \qquad 5.4$$

where Φ is the value of the misfit function from Equation 3.1, and n_d is the number of data points. We depict the values of Φ_{norm} for different iterations of the inversions in Figure 5.1.

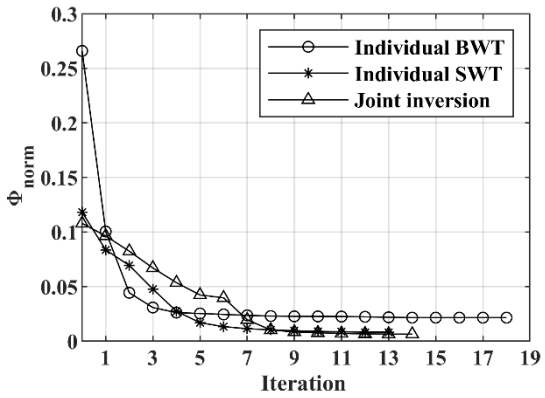

Figure 5.1. The computed Φ_{norm} for different iterations of individual and joint inversion of SWT and BWT.

We can see in Figure 5.1 that the final value of Φ_{norm} has the lowest value in joint inversion. Assuming the data are not redundant, the larger the dataset the harder it becomes to reduce the misfit. Even though the joint inversion scheme deals with a larger dataset, it generates lower final misfit than both individual inversions. The number of iterations required by joint inversion is of the same order of the

individual inversions. We show the obtained VS, and VP models from the individual and joint inversion in Figure 5.2 and Figure 5.3, respectively.

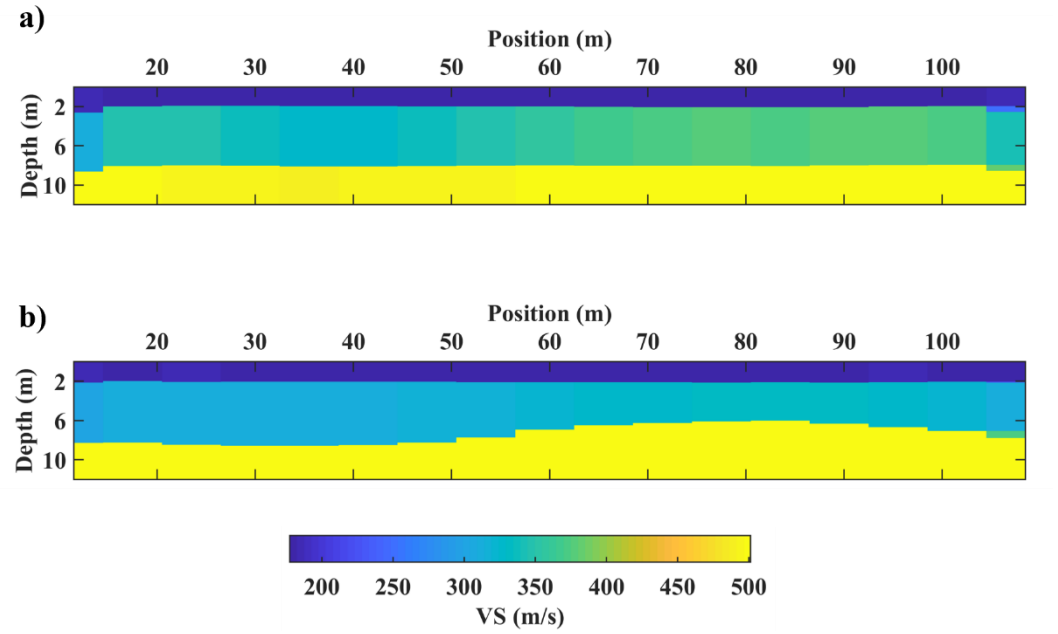

Figure 5.2. The obtained VS models from a) individual SWT, b) joint inversion of SWT and BWT.

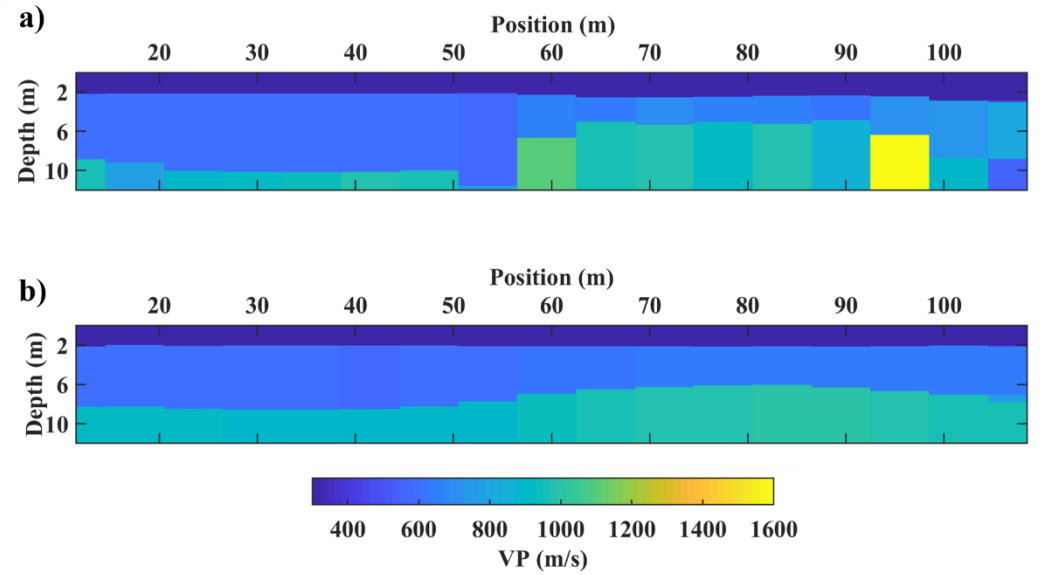

Figure 5.3. The computed VP models from a) individual BWT, b) joint inversion of SWT and BWT.

As shown in Figure 5.2, the second interface is much better recovered in the joint inversion, compared to the individual SWT. In case of individual BWT inversion (Figure 5.3a), the variation of the VP values in the third layer is considerably high with a maximum velocity of more than 1600 m/s, which is far from the true value (950 m/s). This variation is reduced significantly by applying the joint inversion algorithm (Figure 5.3b). The velocity models in Figure 5.2 and Figure 5.3 are used to compute an average error relative to the true velocity models (e_m) from Equation 4.1.In case of VS models (Figure 5.2), the joint inversion produces a model with an average error equal to 8.62%, whereas this error for the VS model from individual SWT is 12.51%. For VP models (Figure 5.3), the e_m for the models from joint inversion and individual BWT are 8.49% and 9.06%, respectively. The obtained velocity models from individual SWT and BWT inversions are used to compute a ν distribution (Figure 5.4a). We have shown the cells with ν values more than 0.5 in black, and the ones with negative values in white. However, the generated ν model from the joint inversion (Figure 5.4b) is both physically meaningful and close to the Poisson's ratio values of the true model. Even though the initial model has ν values which are far from the true values (average error of 22.4%), the obtained ν from the joint inversion algorithm is, with an e_m value of 5.2%, substantially more accurate than from the individual inversions.

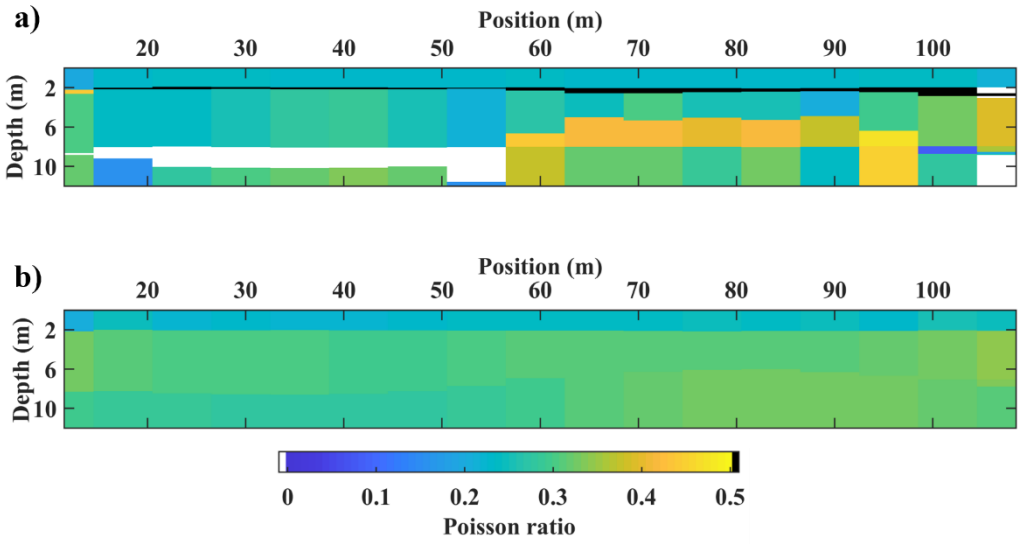

Figure 5.4. The computed ν models from a) individual SWT and BWT inversions, b) joint inversion of SWT and BWT. The cells in black or white have non-physical ν values.

5.3 Pijnacker field: 2D line

We have shown the available well data close to the Pijnacker field in Figure 2.13. We use these data not as a priori information to obtain results, but only a posteriori to assess the results of the inversions.

To start the inversion process, we define an 8-layer laterally homogeneous model. The cell width is equal to 1 m for all cells. Also in this example, we plotted the DC with the broadest frequency band as a function of pseudo-depth (half wavelength) and the mean of the phase velocities in the pseudo-depth range corresponding to each layer interval was computed to obtain the initial VS model. We report the parameters of the initial model in Table 5.2. Also in this case, the values of $\mathbf{C_R}$ were set equal to 10^6. All the inversions start from the same initial model and constraint values. The values of Φ_{norm} for different iterations of the inversions are displayed in Figure 5.5.

Table 5.2. Parameters of the defined initial model.

Layer	1	2	3	4	5	6	7	8
VS (m/s)	70	70	73	74	86	93	103	113
ν	0.3	0.3	0.3	0.3	0.4	0.4	0.4	0.4
h (m)	1	1	1	1	2	2	2	2
ρ (kg/m^3)	1700	1700	1700	1700	1700	1700	1700	1700

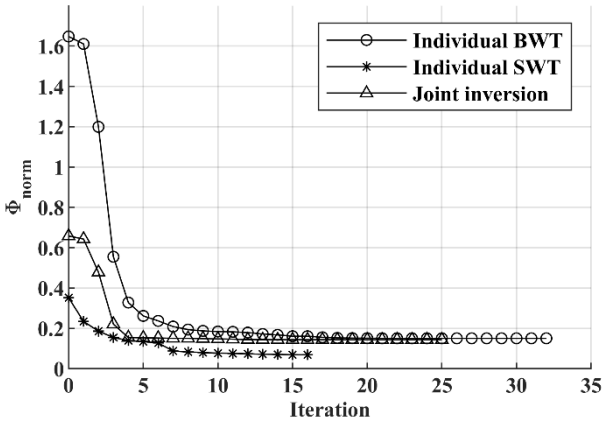

Figure 5.5. The computed normalised misfit Φ_{norm} for different iterations of individual and joint inversions of SWT and BWT.

The obtained VS and VP values from the inversions are depicted in Figure 5.6 and Figure 5.7.

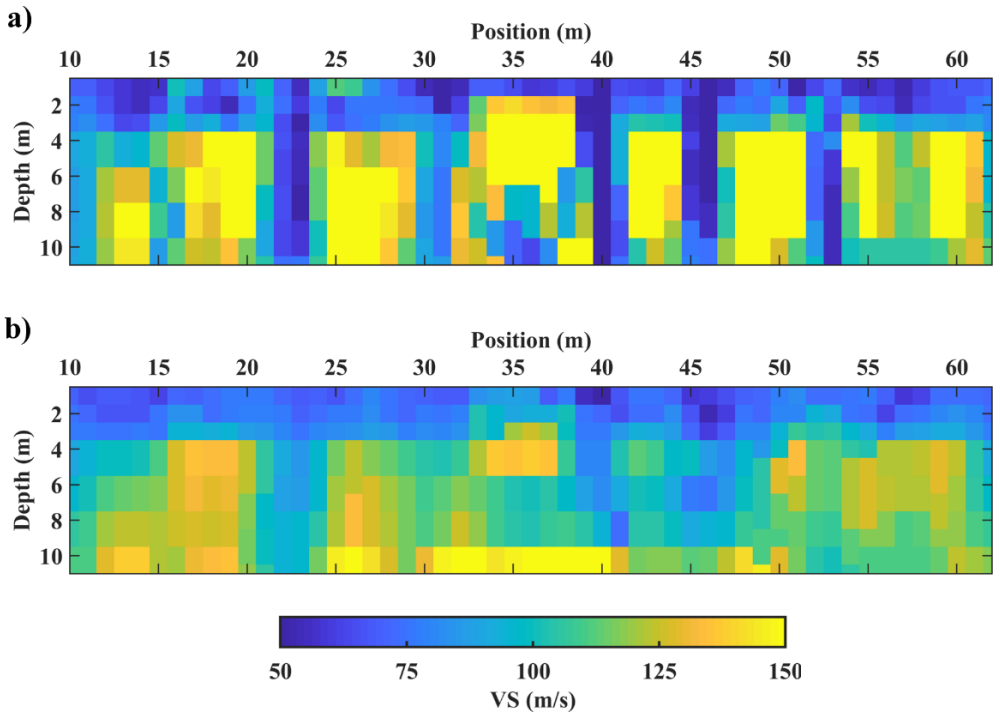

Figure 5.6. The computed VS model from a) individual SWT, b) joint inversion.

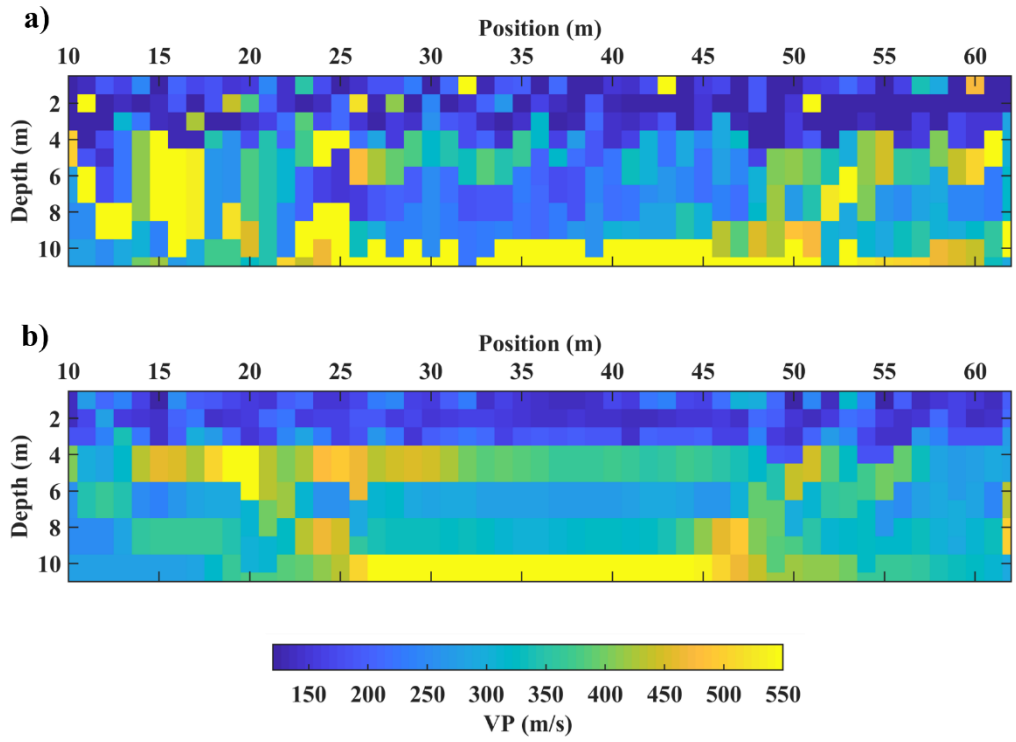

Figure 5.7. The obtained VP model from a) individual BWT, b) joint inversion.

We can see in Figure 5.6 that the VS values in the first three layers are mainly less than 80 m/s. This range of VS, which can be seen particularly in the shallower portion of the model, can be indicative of layers of clay and peat (Bharadwaj et al., 2017). Also, the levels with higher VS values can be associated to sand layers. In most parts of the obtained VS model from individual SWT (Figure 5.6a), higher VS values exist at the depth interval of 4-9 m while in the VS model from joint inversion (Figure 5.6b) the higher VS values mainly exist at levels either deeper than 10 m or depth interval of 4-6 m. In the obtained VP model from joint inversion (Figure 5.6b) there are two layers with high VP. The uppermost one is approximately at the depth of 4-6 m which agrees with well data (the first well in Figure 2.13c) where the sand layer extends from 4-6.5 m followed by peat where VP decreases significantly. Even though the well data are not available for depths more than 7 m, the high VP layer at depth deeper than 10 m probably represents the sand since its VP is close to the shallower high VP layer. The two sand layers are retrieved clearer in the obtained VP model from joint inversion (Figure 5.7b) than individual BWT (Figure 5.7a). Figure 5.8 shows the computed ray paths for the VP models shown in Figure 5.7.

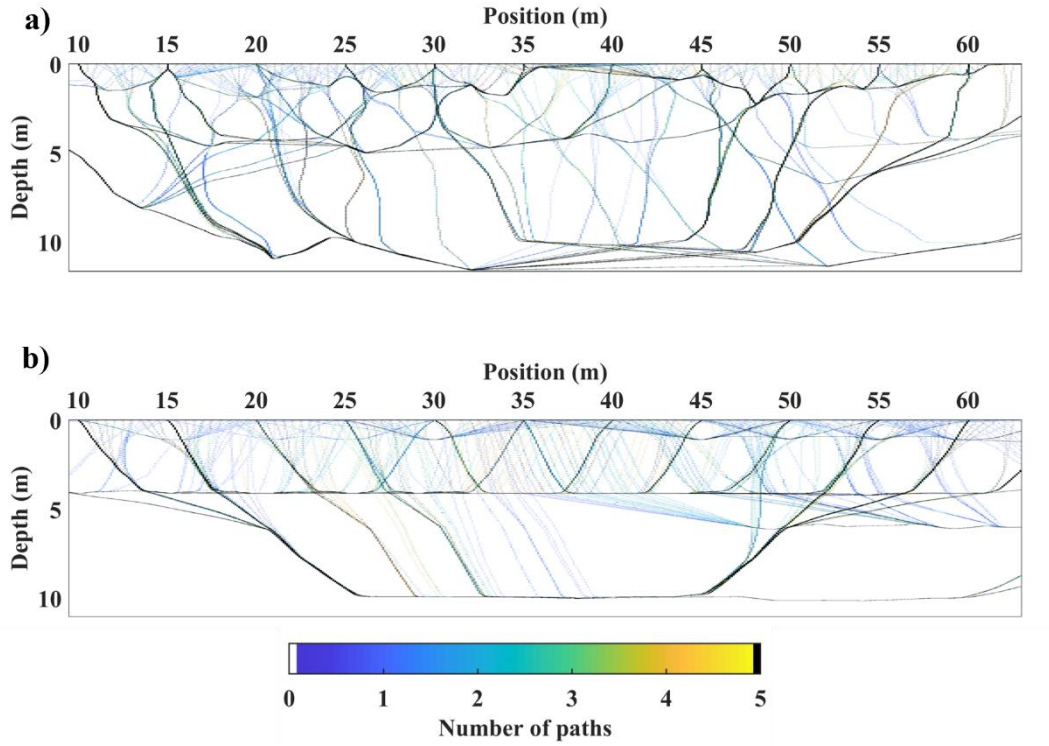

Figure 5.8. The computed ray paths of first arrivals for the Pijnacker field from a) individual BWT, b) joint inversion of SWT and BWT.

We can see in Figure 5.8 that the shallower sand layer has been retrieved with much more lateral consistency by joint inversion (Figure 5.8b) than by individual BWT inversion (Figure 5.8a), particularly from the position at 45 m to the end of the line. The computed ν models from individual inversions and joint inversion are displayed in Figure 5.9. We see also in this case that the ν model from individual inversions (Figure 5.9a) has unrealistic values in several locations, particularly at the shallower portions of the model. However, joint inversion of SWT and BWT has produced physically a meaningful distribution of ν in all the cells (Figure 5.9b).

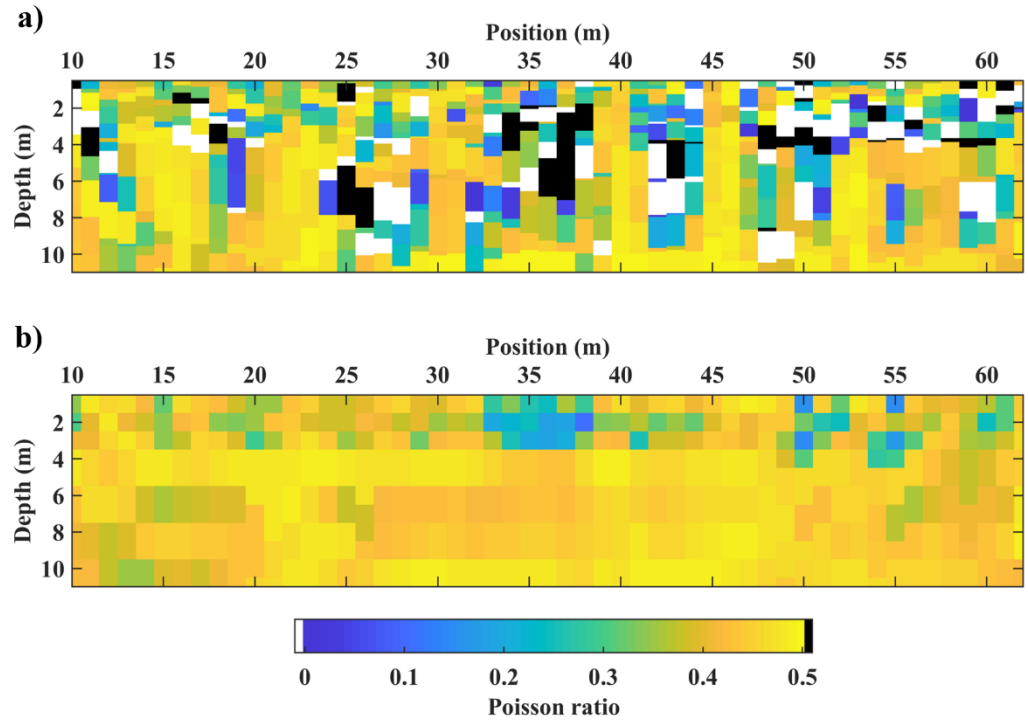

Figure 5.9. The computed v from a) individual SWT and BWT inversions, b) joint inversion of SWT and BWT.

5.2 CNR field: 2D line

We start the inversion from a 5-layer laterally homogeneous model. The assigned width of all cells was 1 m. To define the initial VS values, we again plotted the DC with the broadest frequency band as a function of pseudo-depth (half-wavelength) and the phase velocities were averaged in the pseudo-depth range corresponding to each layer interval. We report the initial model parameters in Table 5.3. To damp the effect of regularization, we set the values of $\mathbf{C_R}$ to 10^6, which means limiting the variation of VS (for example) to 1000 m/s for neighbouring model points.

Table 5.3. Initial model properties for the CNR field example.

Layer	VS (m/s)	ν	Computed VP (m/s)	h (m)	ρ (kg/m^3)
1	100	0.33	200	1	2000
2	120	0.33	240	1	2000
3	150	0.33	300	1	2100
4	190	0.33	380	1	2100
5	260	0.33	520	1	2200

The Φ_{norm} values for different inversions as a function of iteration number is displayed in Figure 5.10.

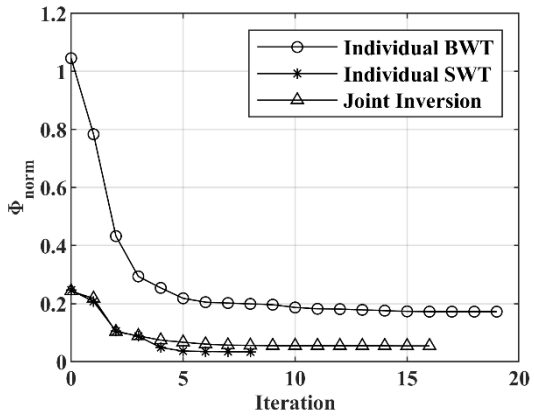

Figure 5.10. The computed Φ_{norm} for different iterations of individual and joint inversion of SWT and BWT.

We can see in Figure 5.10 that the joint inversion algorithm has both lower Φ_{norm} and faster convergence than individual BWT inversion. The SWT inversion seems to get trapped in a local minimum whereas the joint inversion gives a better VS model, even though with a slightly higher misfit value. The obtained velocity models are shown in Figure 5.11 and Figure 5.12.

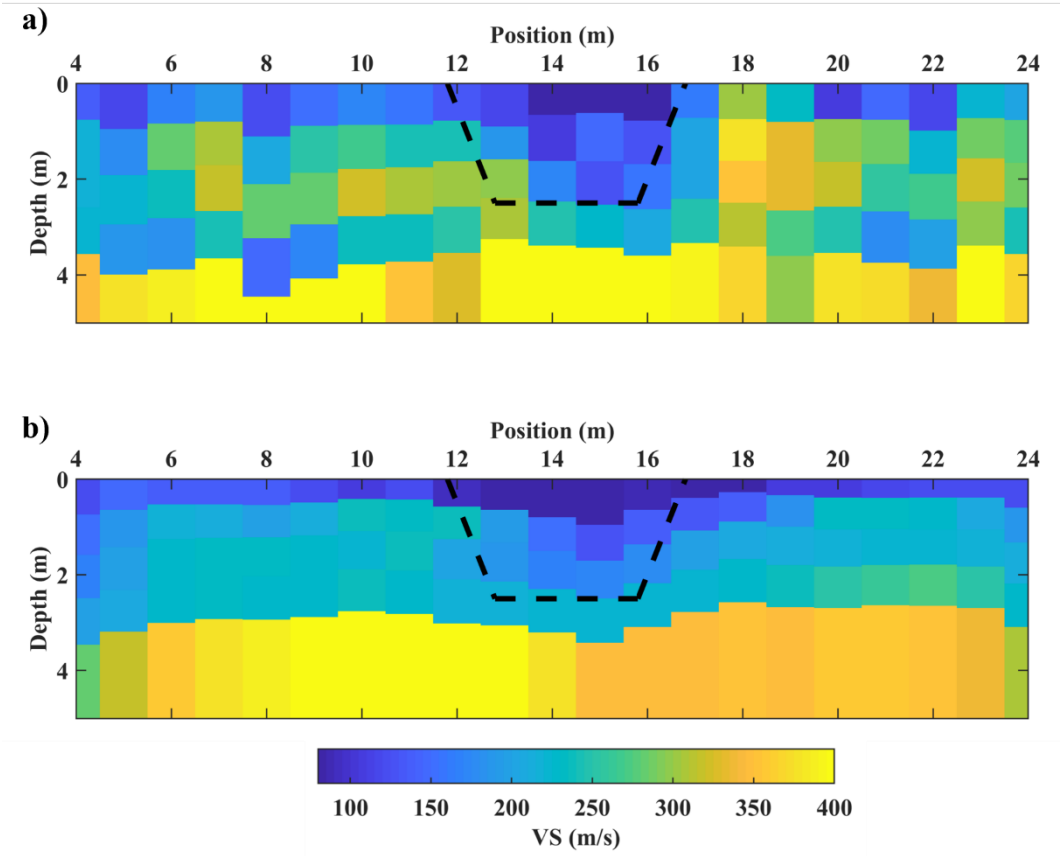

Figure 5.11. The VS models from a) individual SWT, b) joint inversion SWT and BWT. The boundaries of the sand body are superimposed in dashed black.

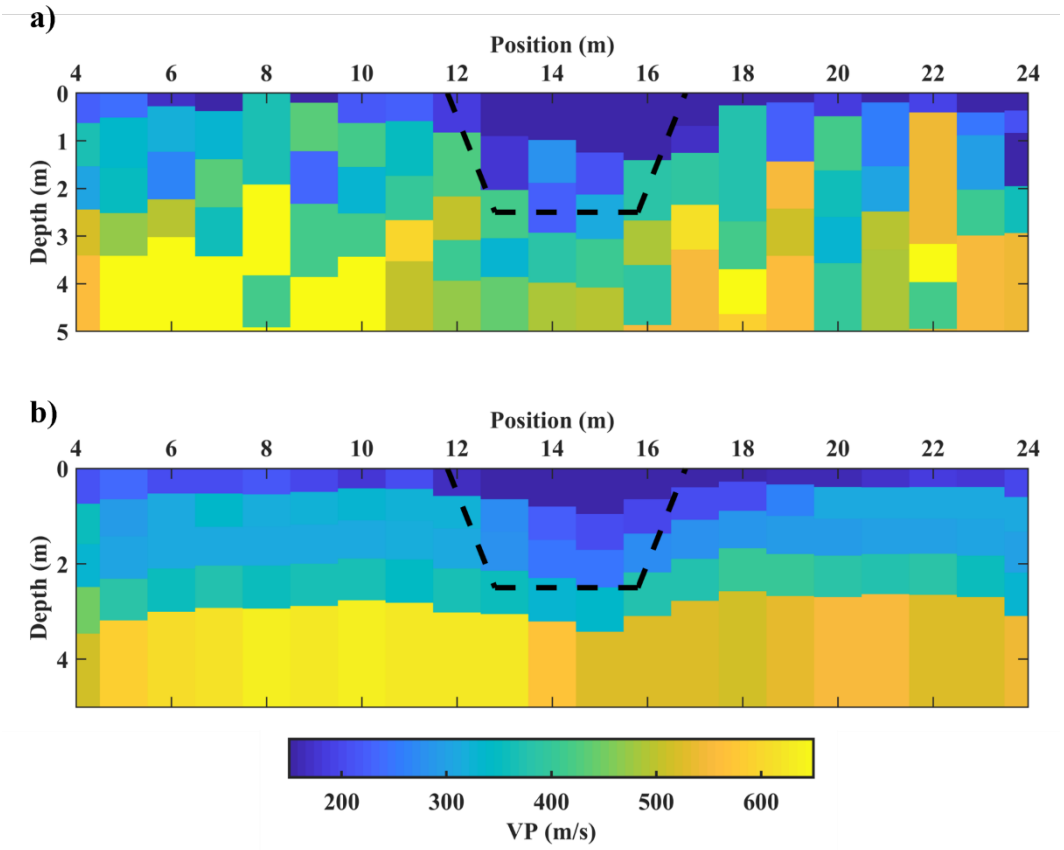

Figure 5.12. The obtained VP models from a) individual BWT, b) joint inversion of SWT and BWT. The boundaries of the sand body are superimposed in dashed black.

Although the velocity contrast between the sand body and the background can be observed in the models from individual inversions (Figure 5.11a and Figure 5.12a), the join inversion velocity models (Figure 5.11b and Figure 5.12b) provide much clearer image of this contrast. Moreover, the gradual increase of the velocities with depth inside the sand body is more obvious in the joint inversion results. Furthermore, the boundaries of the sand deposit are well recovered by the joint inversion algorithm.

In Figure 5.13, we show the computed ray paths of first arrivals corresponding to the VP models in Figure 5.12.

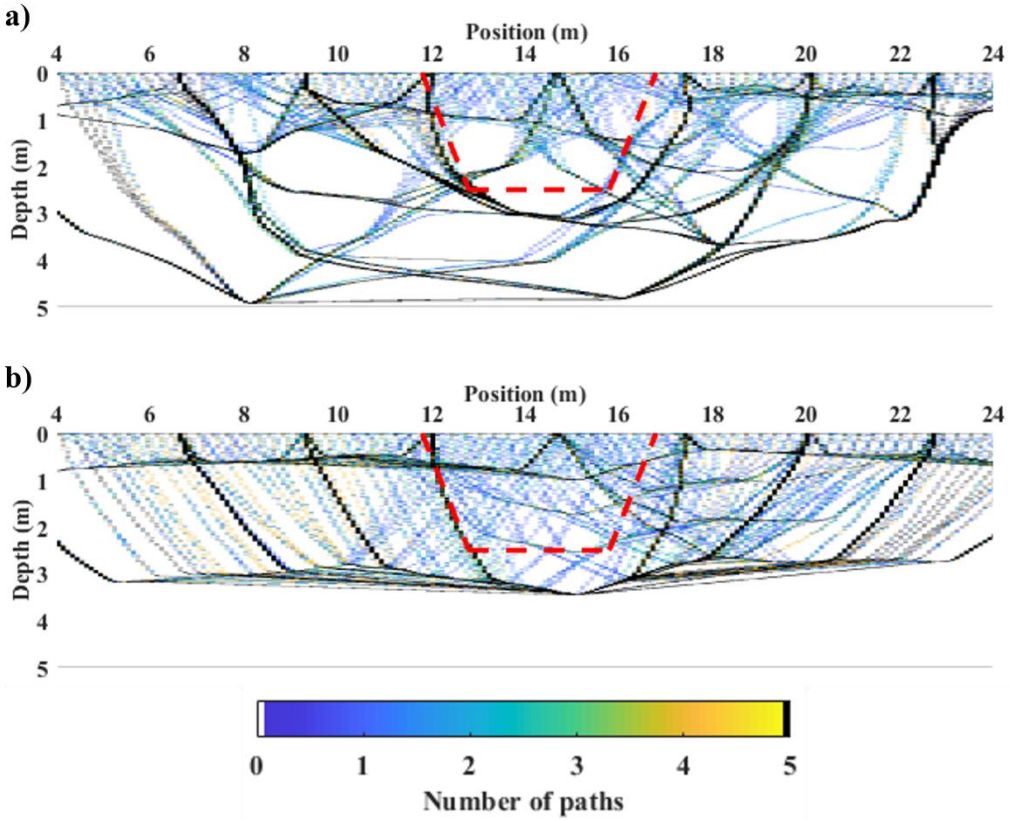

Figure 5.13. The computed ray paths of the first arrivals for the CNR site from a) individual BWT, b) joint inversion of SWT and BWT. The boundaries of the loose sand are shown in dashed red.

We see in Figure 5.13 that the distribution of ray paths is more uniform in case of the joint inversion (Figure 5.13b), particularly in the bottom half of the sand body.

The obtained ν distribution from individual inversions and joint inversion are shown in Figure 5.14. We can see that the computed ν model from individual inversions (Figure 5.14a) consists of non-physical values in many locations (shown in black or white). However, the obtained ν values from the joint inversion of SWT and BWT (Figure 5.14b) do not suffer from this problem. As mentioned previously in Chapter 3, during the joint inversion process, some cells may have non-physical ν values. To address this issue, we change the damping factor until at least 75 % of all cells have physical ν values. Then, for the remaining cells with non-physical ν, we assign velocity values equal to the average of the velocities of adjacent cells. Figure 5.14b shows that only a couple of cells (marked in white) in the last iteration of the joint inversion had non-physical ν values. For these cells, new velocities are

computed through averaging the velocities of the neighbouring cells and new Poisson ratio values are obtained.

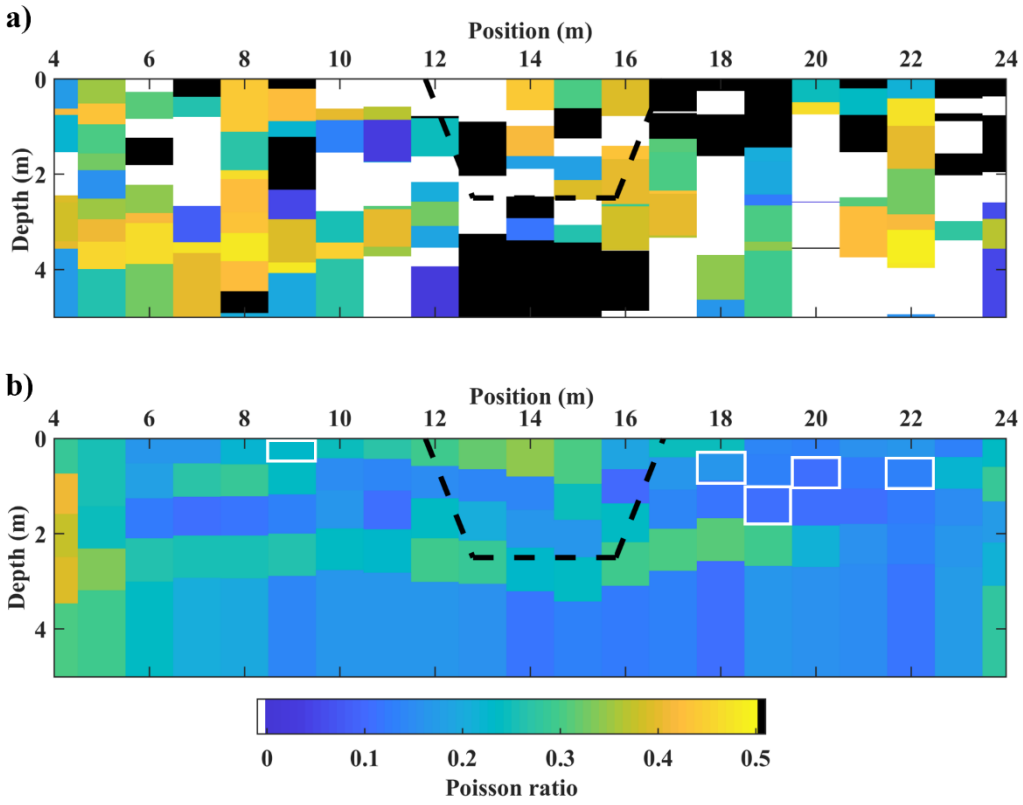

Figure 5.14. The computed v models from a) individual SWT and BWT inversions, b) joint inversion of SWT and BWT. The boundaries of the cells which had non-physical v values in the last iteration of joint inversion are shown in white. The boundaries of the sand body are superimposed in dashed black.

5.4 3D example: CNR

Here, we extend the joint inversion of SWT and BWT to 3D. In 3D, we can perform SWT in two different ways: straight-ray and curved-ray. Therefore, we carry out the joint inversion twice. First, joint inversion of BWT and straight-ray SWT, and then joint inversion of BWT and curved-ray SWT.

We apply the 3D joint inversion algorithm to the CNR 3D dataset. In Chapter 4, we used four 3D examples to investigate the results of straight- and curved-ray SWT. The CNR example had the lowest computational time among all those four examples which makes it a good candidate for our 3D joint inversion since adding

3D BWT to SWT will considerably increase the computational time. Moreover, the difference between straight- and curved-ray SWT was more significant in case of the 3D CNR example. This also makes the CNR example suitable for the joint inversion since we can track the possible model improvement by 3D joint inversion more clearly.

To have a fair comparison, we start all individual and joint inversions from the same initial model. Also in this case, we compute the initial VS based on the phase velocity values of the DC with the broadest frequency band. We show the parameters of the initial model in Table 5.4.

Table 5.4. The parameters of the initial model for the inversion.

Layer	VS (m/s)	ν	Computed VP (m/s)	h (m)	ρ (kg/m^3)
1	100	0.33	200	0.5	2000
2	110	0.33	220	0.5	2000
3	120	0.33	240	0.5	2000
4	135	0.33	270	0.5	2000
5	150	0.33	300	0.5	2100
6	165	0.33	330	0.5	2100
7	190	0.33	380	0.5	2100
8	250	0.33	500	0.5	2100

Also in this case, the values of $\mathbf{C_R}$ are set equal to 10^6, and we start the individual and joint inversion from the same initial model. We show the obtained VS models from individual and joint inversions in Figure 5.15. There are four columns in Figure 5.15. The first two columns correspond to the VS models from individual straight-ray and curved-ray SWT, respectively. The third column

displays the VS model from the joint inversion of BWT and straight-ray SWT and the last one corresponds to the joint inversion of BWT and curved-ray SWT. It should be noted that the level of complexity of the method increases from the first column (straight-ray SWT) as the simplest to the last column (joint inversion of BWT and curved-ray SWT).

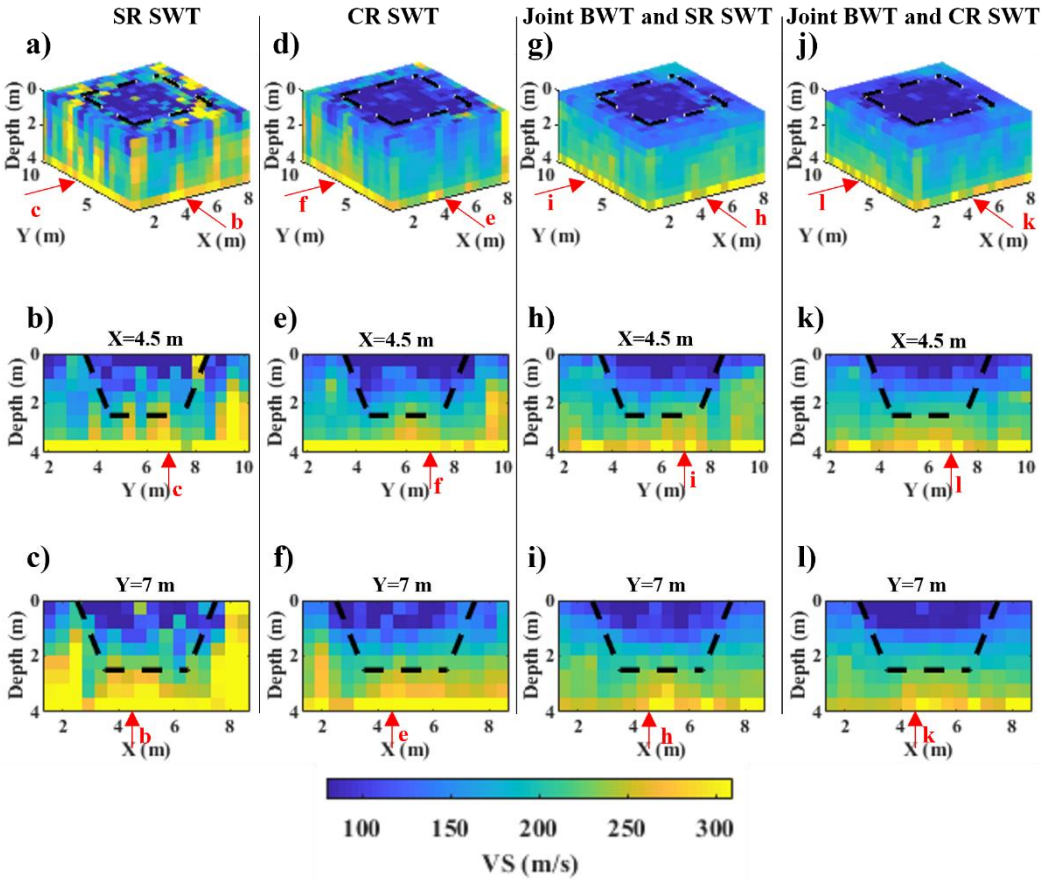

Figure 5.15. The obtained VS models from individual straight-ray SWT (subfigures a-c), individual curved-ray SWT (subfigures d-f), joint inversion of BWT and straight-ray SWT (subfigures g-i), and joint inversion of BWT and curved-ray SWT (subfigures j-l). For each method, we have shown the 3D model at the top of the column, following by two cross-sections at X=4.5 m and Y=7 m. The boundaries of the sand body are superimposed in dashed black. Each red arrow shows the location of the corresponding cross-section in the current subfigure.

We see in Figure 5.15 that the quality of the obtained VS model improves as we move from the first column (individual straight-ray SWT) to the last one (joint inversion of BWT and curved-ray SWT). We can see in the 3D model from straight-ray SWT (Figure 5.15a) that even though the boundaries of the sand body can be

observed, there are some high velocity artefacts in the shallow portions of the reconstructed model. These artefacts are reduced in the obtained VS models from the other methods, with the joint inversion of BWT and curved-ray SWT (Figure 5.15j) providing the clearest image of the sand body.

For each method in Figure 5.15, the two vertical cross-sections show the produced VS models in depth. We see in both cross-sections that the sand body is better retrieved in depth as we move to the right (joint inversion of BWT and curved-ray SWT) where the low-velocity and the boundaries of the sand body are better constructed than the other methods.

In Figure 5.16, we show the computed ray paths for three DCs corresponding to the obtained VS models in Figure 5.15. Since the ray paths in the straight-ray SWT do not change, we only display the examples of ray paths for individual curved-ray SWT (Figure 5.16a) and joint inversion of BWT and curved-ray SWT (Figure 5.16b).

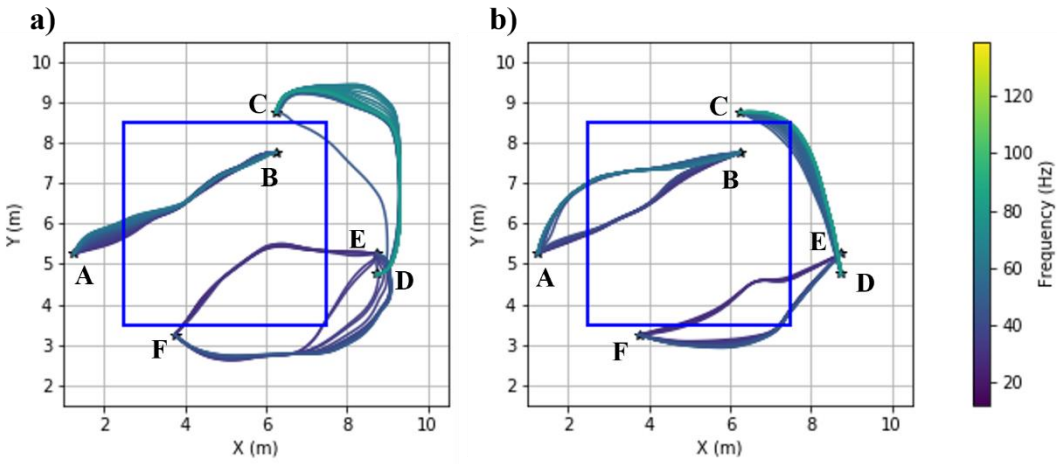

Figure 5.16. Examples of the computed ray paths for three DCs at the last iteration of a) individual curved-ray SWT, b) joint inversion of BWT and curved-ray SWT. The boundaries of the sand body at the surface are superimposed in blue. The locations of the receivers are labelled as A-F.

Figure 5.16 shows that the computed ray paths from the joint inversion (Figure 5.16b) have responded to the sand body better than the individual curved-ray SWT (Figure 5.16a). We can see that while the paths between A and B are almost straight in Figure 5.16a, the high frequency components in Figure 5.16b have deviated from the straight line and travel in the higher velocity portion. Moreover, the depicted ray paths for the other two DCs (CD and EF pairs) also show that the ray paths from

the joint inversion (Figure 5.16b) have responded to the edges of the sand body more properly than the individual inversion (Figure 5.16a).

In Figure 5.17, we show the obtained VP models in three columns: first, individual BWT, then joint inversion of BWT and straight-ray SWT, and finally joint inversion of BWT and curved-ray SWT. For each method, the results are shown in 3D and two vertical cross-sections at X equal to 4.5 m and Y equal to 7 m.

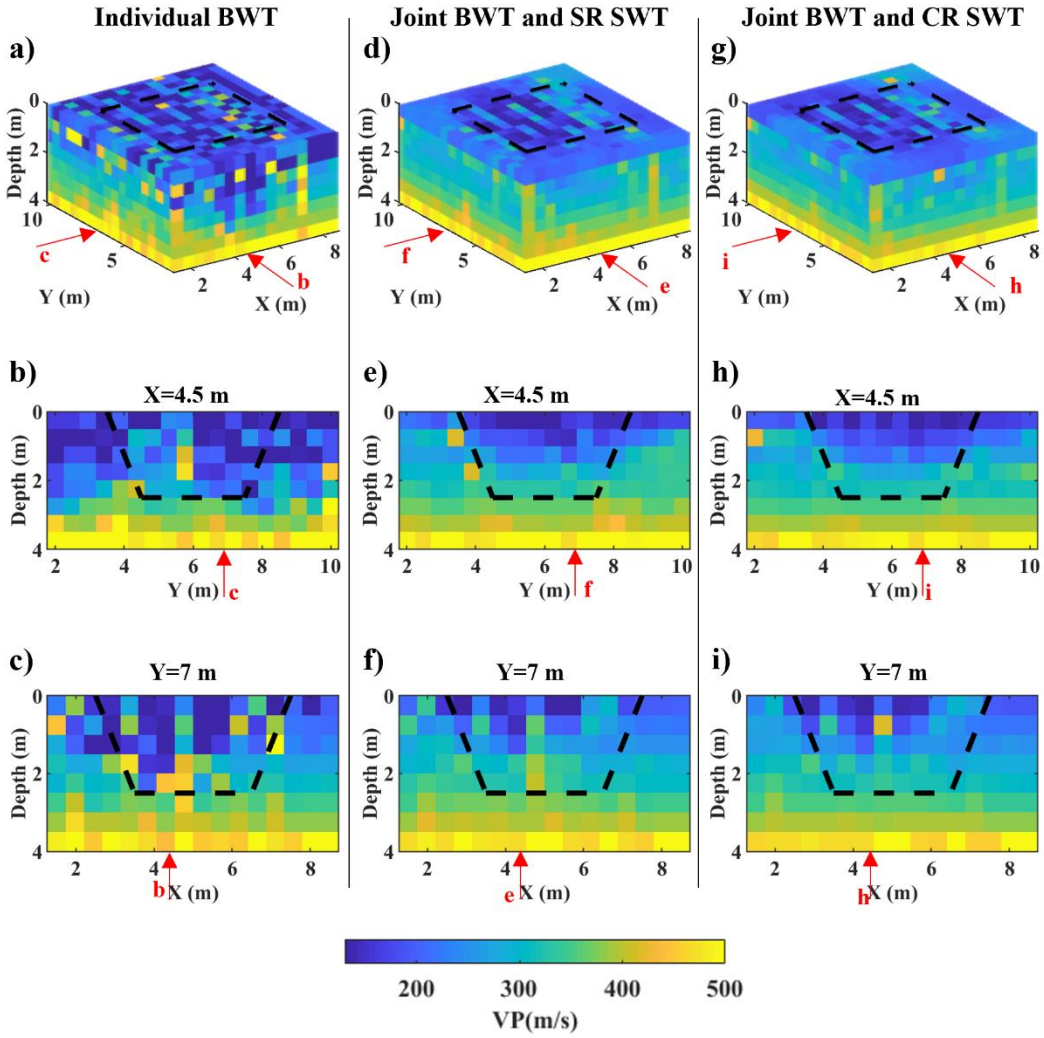

Figure 5.17. The obtained VP models from individual BWT (subfigures a-c), joint inversion of BWT and straight-ray SWT (subfigures d-f), and joint inversion of BWT and curved-ray SWT (subfigures g-i). For each method, we have shown the 3D model at the top of the column, following by two vertical cross-sections at X=4.5 m and Y=7 m. The boundaries of the sand body are superimposed in dashed black. Each red arrow shows the location of the corresponding cross-section in the current subfigure.

Figure 5.17 shows that the sand body cannot be seen properly in the retrieved 3D VP model from individual BWT (Figure 5.17a). However, the extent of the sand body is significantly clearer in the obtained 3D VP model from the joint inversions (Figure 5.17d and e). The footprint of the acquisition layout (Figure 2.21a) is clear the in these figures (Figure 5.17d and e) where the improvement of the 3D VP model in the Y direction is more significant than the X direction. For the cross-

sections in the X direction, we see that the VP model from individual BWT inversion (Figure 5.17b) has not modelled the boundaries of the sand body properly. On the other hand, the sand body can be clearly seen in the VP models from both joint inversions (Figure 5.17e and h). In case of the cross-section at Y equal to 7 m, the sand body can be seen in the VP model from the individual BWT (Figure 5.17c). Even though the boundaries of the sand body are not retrieved accurately, this cross-section of individual BWT provides a better image of the sand body compared to its 3D image (Figure 5.17a) and the cross-section in X-direction (Figure 5.17b). In the VP models from both joint inversions (Figure 5.17f and i), we can see that the cells with a low velocity value are located inside the area of the sand body (shown in dashed black).

In Figure 5.18, we display the computed ray paths of the first arrivals for the VP models shown in Figure 5.17.

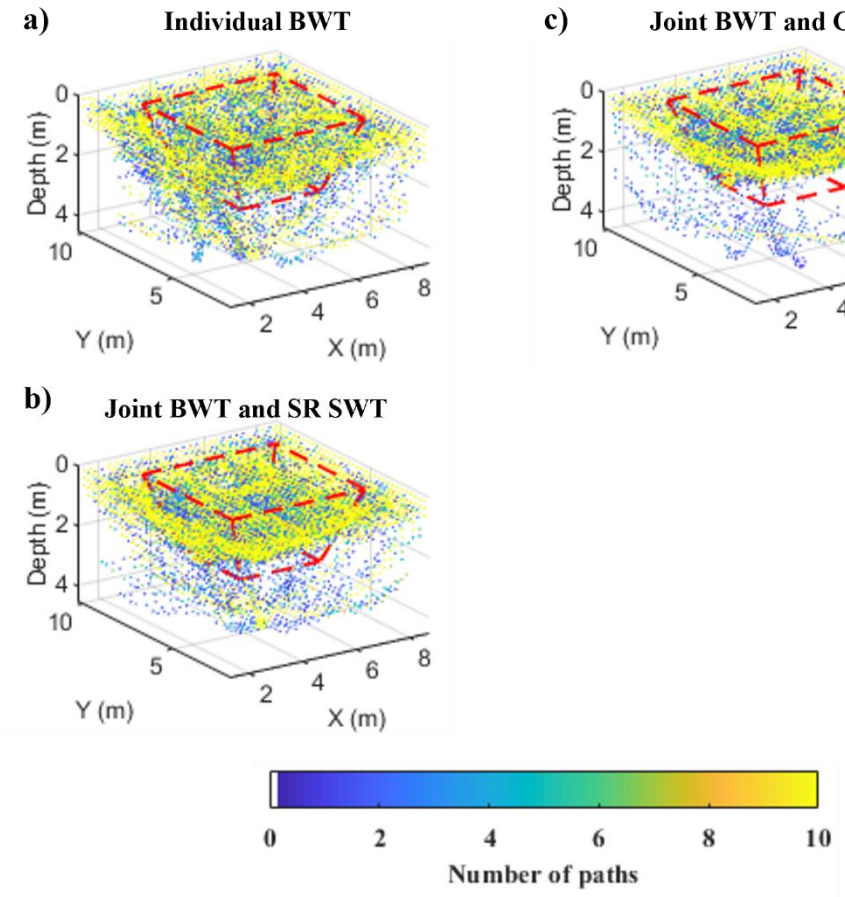

Figure 5.18. The computed ray paths of the first arrivals for the obtained VP model from a) individual BWT (Figure 5.17a), b) joint inversion of BWT and straight-ray SWT (Figure 5.17d), c) joint inversion of BWT and curved-ray SWT (Figure 5.17g). The boundaries of the sand body are superimposed in red.

Figure 5.18 shows that most of the paths are concentrated in the depths range of 0-2 m and some paths which correspond to larger distances between shots and receivers, travel through the deepest portion of the model. We can also see in the joint inversions that the straight-ray SWT (Figure 5.18b) changes the deeper ray paths much less than the curved-ray SWT (Figure 5.18c).

In Figure 5.19, we depict the computed ν models from individual and joint inversions in four columns. For the first two columns, we have computed the ν using the VP from individual BWT and the VS model from individual straight- and curved-ray SWT, respectively. The third column represents the ν from the joint inversion of BWT and straight-ray SWT and the fourth one corresponds to the joint inversion of BWT and curved-ray SWT.

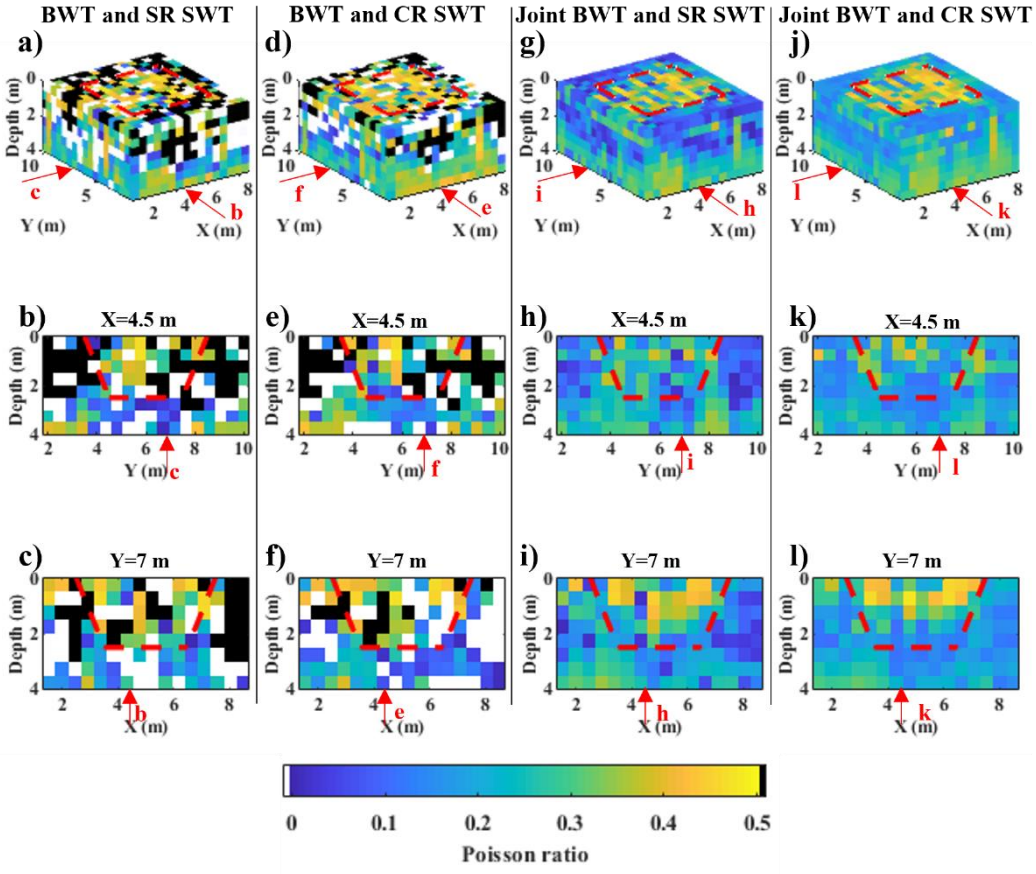

Figure 5.19. The computed ν models from: individual BWT and straight-ray SWT (subfigures a-c), individual BWT and curved-ray SWT (subfigures d-f), joint inversion of BWT and straight-ray SWT (subfigures g-i), and joint inversion of BWT and curved-ray SWT (subfigures j-l). For each method, we have shown the 3D model at the top of the column, following by two vertical cross-sections at X=4.5 m and Y=7 m. The grids with ν values more than 0.5 are shown in black, and the ones with ν values less than zero are displayed in white. The boundaries of the sand body are superimposed in dashed red. Each red arrow shows the location of the corresponding cross-section in the current subfigure.

In Figure 5.19, we can see that the ν models from the individual inversions (Figure 5.19a-f) contain non-physical values in many locations. However, the models from both joint inversions (Figure 5.19g-l) have physical ν values in all cells. It should be noted that the constructed ν models from the joint inversions might have some artefacts. Particularly, some cells at shallow depths have much higher ν values than the layers beneath them (Figure 5.19g, i, j, and l). Nevertheless, the retrieved ν models from the joint inversions (Figure 5.19g-l) show significant improvement compared to the individual ones (Figure 5.19a-f).

5.4 Conclusions

We applied the joint inversion of BWT and SWT to one synthetic and two field examples in 2D. We have compared the computed VS, VP, and ν models from the individual and joint inversion of SWT and BWT. We showed that the proposed joint inversion algorithm provides better velocity models than the individual inversions. Joint inversion produced ν models that appear more physically meaningful, which individual inversions did not. We then applied the joint inversion to one 3D example. We showed that also in 3D, the obtained velocity and ν models from the joint inversion improved considerably compared to models obtained from individual inversions.

Chapter 6

Conclusions and Outlook

6.1 Concluding remarks

We aimed to investigate the following two questions:

- What are the differences between the performance of straight-ray and curved-ray SWT at the near-surface scale?
- Is it possible to improve the obtained velocity models from SWT and BWT through a joint inversion scheme?

We successfully applied SWT to different numerical and field examples. We also proposed a scheme for the joint inversion of SWT and BWT in 2D and 3D media. We showed that the suggested joint inversion algorithm improved the results of individual inversions.

We employed a survey design scheme which enabled us to choose the source positions such that high coverage of DC data could be obtained in 3D acquisition layouts. We applied this method to optimise the shot positions in three 3D examples (Blocky model, Sand Bar model, and Pijnacker field) and obtained high data coverage in all cases. In the CNR 3D example, we showed that the classical cross-spread acquisition layout, which is a typical exploration layout, might not provide high DC coverage for a SWT study.

We showed that SWT, an established method in seismology, could successfully construct VS models of the shallow (first few meters) subsurface. In case of the numerical examples, we were able to model the velocity anomalies accurately even though the inversion started from a homogeneous half-space. In both Blocky and Sand Bar models, the final average data misfit values at the last iteration of straight-ray and curved-ray SWT were very low (almost 1 %). In both numerical examples, the obtained VS models at the last iteration of straight-ray and curved-ray SWT were similar.

We then successfully applied both SWT approaches to the Pijnacker field 3D dataset and showed that the obtained VS models agree with the available borehole data near to the site location. We showed that the VS models from straight-ray and curved-ray SWT were very similar. We found that in case of CNR example, despite the previous examples, the difference between the obtained VS models from straight-ray and curved-ray approaches was more pronounced. The target (sand body) came out more clearly in the results using curved-ray in the inversion. We illustrated that the DC coverage in the straight-ray approach was not high enough and some areas in the shallower part of the model were not covered by the data while in the curved-ray approach, the inter-station paths responded to the target properly and covered more areas of the model.

By evaluating the SWT results from all four 3D examples, we realized that the use of a ray tracing method improved the accuracy of the obtained final VS model slightly (by average 4 %) but increased the computational cost significantly (by average 23 %). We concluded that in case of high data coverage, straight-ray SWT could provide almost equally good results as curved-ray approach, with considerably less computational cost. However, if the DC coverage was not high, which could be the case in the typical exploration layouts, the use of curved-ray SWT can significantly improve the obtained VS model.

We also developed a scheme for the joint inversion of SWT and BWT in 2D and 3D media. To the best of our knowledge, it is the first example in which SW and first-arrivals from active seismic data are integrated into a tomographic joint inversion scheme. The application of our joint inversion method to a 2D synthetic example (the Step model) revealed that the retrieved VS and VP models from the joint inversion were more accurate than individual inversions. Moreover, the retrieved Poisson's ratio distribution from the joint inversion was very close to the true values (average error of 5.2 %). However, the computed Poisson's ratio model from the individual inversions had non-physical values in several positions. We then applied the proposed joint inversion scheme to the CNR and Pijnacker 2D field datasets. In case of the CNR example, the results showed that even though the target could be modelled by individual SWT and BWT inversions, it was clearer in the produced velocity models by the proposed joint inversion algorithm. For the Pijnacker field example, the comparison between the obtained velocity models from individual and joint inversions with the available borehole data in the site verified that the joint inversion has produced better results. In both CNR and Pijnacker field examples, the obtained Poisson's ratio model from the proposed joint inversion provided physically meaningful values for all cells while the computed model from

the individual inversions contained non-physical Poisson's ratio values in many positions.

After successful application of the suggested joint inversion scheme to three 2D examples, we applied the method to the CNR 3D dataset. We obtained four VS models and three VP models for this example. The VS models were produced by individual straight-ray SWT, individual curved-ray SWT, joint inversion of straight-ray SWT and BWT, and joint inversion of curved-ray SWT and BWT. The VP models were the results of individual BWT, joint inversion of straight-ray SWT and BWT, and joint inversion of curved-ray SWT and BWT. The results illustrated that for both VS and VP models, the joint inversion methods provided better results than individual inversions. The obtained VS models showed that curved-ray SWT generated better results than straight-ray SWT. Individual curved-ray SWT produced a better VS model than individual straight-ray SWT, and the VS model from the joint inversion of curved-ray SWT and BWT was better than the joint inversion of straight-ray SWT and BWT. We also compared the computed frequency dependent ray paths of DCs from individual curved-ray SWT and joint inversion of curved-ray SWT and BWT. We showed that the response of ray paths to the target, from the joint inversion was better than individual curved-ray SWT. The improvement was very significant in case of the VP models where the individual BWT could not locate the target properly, whereas the joint inversion methods provided VP models with a clearer image of the target. The footprint of the cross-spread acquisition layout was clear in the obtained VP models, where the gained improvement of VP was more significant in one horizontal direction than the other. It revealed that the typical exploration acquisition layouts may not be optimum for near-surface studies. We then evaluated the obtained Poisson's ratio models from the joint inversion methods and individual inversions. Like the 2D examples, the results determined that the computed Poisson's ratio models from individual inversions had non-physical values in many locations. However, the models from joint inversion methods were physically meaningful in all layers.

6.2 Suggestions for future works

In our inversion algorithms, both individual and joint, we employed the "standard" spatial regularization (Auken and Christiansen, 2004). As a future work, other types of regularizations can be tested and integrated into our inversion scheme.

Regarding the SWT methods in Chapter 4, a possible extension would be to evaluate straight-ray and curved-ray approaches in shallow marine environments. For this purpose, the forward modelling of the SW should be performed by considering Scholte waves, which are the dominant type of surface waves in the shallow marine environments.

In case of the proposed joint inversion scheme, a priori information on Poisson's ratio values can be incorporated to the defined algorithm. We found out that even though constraining the values of Poisson's ratio to be physically meaningful improves the velocity models, it does not necessarily guarantee that they are also physically realistic. Khosro Anjom (2021) proposed a method to estimate Poisson's ratio distributions using only SW data. This method might be used to constrain the obtained Poisson's ratio values from the proposed joint inversion method.

Chapter 7

References

Aki, K., Richards, P.G., 1980, Quantitative seismology: Theory and methods, W.H. Freeman & Co.

Almeida, S., Holcombe, E.A., Pianosi, F., and Wagener, T., 2017, Dealing with deep uncertainties in landslide modelling for disaster risk reduction under climate change, Natural Hazards and Earth System Sciences, 17, 225–241, doi: 10.5194/nhess-17-225-2017

Anbazhagan, P., Sheikh, M.N., and Parihar, A., 2013, Influence of rock depth on seismic site classification for shallow bedrock regions, Natural Hazards Review, 14(2), 108-121, doi: 10.1061/(ASCE)NH.1527-6996.0000088

Aster, R.A., Brochers, B., and Thurber, C.H., 2005, Parameter Estimation and Inverse Problems, Elsevier Academic Press

Auken, E., and Christiansen, A.V., 2004, Layered and laterally constrained 2D inversion of resistivity data, Geophysics, 69(3), 752-761, doi: 10.1190/1.1759461.

Bačić, M., Librić, L., Kaćunić, D.J., Kovačević, M.S., 2020, The Usefulness of Seismic Surveys for Geotechnical Engineering in Karst: Some Practical Examples, Geosciences, 10(10), 406, doi:10.3390/geosciences10100406

Bardainne, T., Garceran, K., Retailleau, M., Duwattez, X., Sternfels, R., and Le Meur, D., 2017, Laterally Constrained Surface Wave Inversion, Expanded abstract, EAGE, 1-5, doi: 10.3997/2214-4609.201700957.

Bardainne, T., 2018, Joint Inversion of Refracted P-waves, Surface Waves and Reflectivity, European Association of Geoscientists and Engineers, 1, 1-5, doi: 10.3997/2214-4609.201801158.

Barone, I., Kästle, E., Strobbia, C., and Cassiani, G., 2021, Surface wave tomography using 3D active-source seismic data, Geophysics, 86, 13-26, doi: 10.1190/GEO2020-0068.1

Bergamo, P., Dashwood, B., Uhlemann, S., Swift, R., Chambers, J.E., Gunn, D.A., and Donohue, S., 2016, Time-lapse monitoring of climate effects on earthworks using surface wave, Geophysics, 81(2), 1-15, doi: 10.1190/GEO2015-0275.1.

Bharadwaj, P., Drijkoningen, G., Mulder, W., Thorbecke, J., Neducza, B. and Jenneskens, R., 2017. A shear-wave seismic system using full-waveform inversion to look ahead of a tunnel-boring machine. Near Surface Geophysics, *15*(3), pp.210-225, doi: 10.3997/1873-0604.2017014

Bodin, T., and Sambridge, M., 2009, Seismic tomography with the reversible jump algorithm, Geophysical Journal International, 178, 1411-1436, doi: 10.1111/j.1365-246X.2009.04226.x

Bohlen, T., 2002, Parallel 3-D viscoelastic finite-difference seismic modelling, Computers and Geosciences., 28, 887-899, doi: 10.1016/S0098-3004(02)00006-7.

Bohlen, T., and Wittkamp, F., 2016, Three-dimensional viscoelastic time-domain finite-difference seismic modelling using the staggered Adams–Bashforth time integrator, Geophysical Journal International, 204(3), 1781-1788, doi: 10.1093/gji/ggv546.

Boiero, D, 2009, Surface wave analysis for building shear wave velocity models: Ph.D. thesis, Politecnico di Torino.

Boiero, D., and Socco, L.V., 2014, Joint inversion of Rayleigh-wave dispersion and P-wave refraction data for laterally varying models, Geophysics, 79(4), 49-59, doi: 10.1190/geo2013-0212.1.

Boschi, L. and Ekström, G., 2002, New images of the Earth's upper mantle from measurements of surface wave phase velocity anomalies, Journal of Geophysical Research: Solid Earth, 107(4), doi: 10.1029/2000JB000059.

Bozdağ, E., and Trampert, J., 2008, On crustal corrections in surface wave tomography, Geophysical Journal International, 172(3), 1066-1082, doi: 10.1111/j.1365-246X.2007.03690.x.

Bussat, S., and Kugler, S., 2011, Offshore ambient-noise surface-wave tomography above 0.1 Hz and its applications, The Leading Edge, 30(5), 514-524, doi: 10.1190/1.3589107.

Chiao, L.Y. and Kuo, B.Y., 2001, Multiscale seismic tomography, Geophysical Journal International, 145(2), 517-527, doi: 10.1046/j.0956-540x.2001.01403.x

Colombo, D., and Rovetta, D., 2018, Coupling strategies in multiparameter geophysical joint inversion, Geophysical Journal International, 215(2), 1171-1184, doi: 10.1093/GJI/GGY341.

Da Col, F., Papadopoulou, M., Koivisto, E., Sito, L., Savolainen, M., and Socco, L.V., 2020, Application of surface-wave tomography to mineral exploration: a case study from Siilinjärvi, Finland, Geophysical Prospecting, 68(1), 254-269, doi: 10.1111/1365-2478.12903.

Dal Moro, G., Pipan, M., and Gabrielli, P., 2007, Rayleigh wave dispersion curve inversion via genetic algorithms and marginal posterior probability density estimation, Journal of Applied Geophysics, 61, 39-55.

Dal Maro, G., 2008, VS and VP vertical profiling via joint inversion of Rayleigh waves and refraction travel times by means of bi-objective evolutionary algorithm, Journal of Applied Geophysics, 66, 15-24, doi: 10.1016/j.jappgeo.2008.08.002.

De Stefano, M., 2011, Simultaneous joint inversion for susceptibility and velocity, SEG Technical Program Expanded Abstracts, doi: 10.1190/1.3628198.

Dell'Aversana, P., Bernasconi, G., Miotti, F., and Rovetta, D., 2011, Joint inversion of rock properties from sonic, resistivity and density well-log measurements, Geophysical Prospecting, 59(6), 1144–1154, doi: 10.1111/j.1365-2478.2011.00996.x.

Doetsch, J., Linde, N., Coscia, I., Greenhalgh, S.A., Green, A.G., 2010, Zonation for 3D acquifer characterization based on joint inversion of multimethod crosshole geophysical data, Geophysics, 75, 53-64, doi: 10.1190/1.3496476.

Dunkin, J.W., 1965, Computation of modal solutions in layered, elastic media at high frequencies, Bulletin of the Seismological Society of America, 55, 335- 358, doi: 10.1785/BSSA0550020335.

Dziewonski, A. M., and Hales, A. L., 1972, Numerical Analysis of Dispersed Seismic Waves, Methods in Computational Physics: Advances in Research and Applications, 11, 39-85, doi: 10.1016/B978-0-12-460811-5.50007-6.

Esfahani, R.D.D., Gholami, A., Ohrnberger, M., 2020, An inexact augmented Lagrangian method for nonlinear dispersion curve inversion using Dix-type global linear approximation, Geophysics, 85(5), 1-38, doi: 10.1190/geo2019-0717.1.

Fang, H., Yao, H., Zhang, H., Huang, Y., and van der Hilst, R.D., 2015, Direct inversion of surface wave dispersion for three-dimensional shallow crustal structure based on ray tracing: methodology and application, Geophysical Journal International, 201, 1251-1263, doi: 10.1093/gji/ggv080.

Fang, H., Zhang, H., Yao, H., Allam, A., Zigone, D., Ben-Zion, Y., Thurber, C., and van der Hilst, R.D., 2016, A new algorithm for three-dimensional joint inversion of body wave and surface wave data and its application to the Southern California plate boundary region, Journal of Geophysical Research: Solid Earth, 121, 3557–3569, doi:10.1002/2015JB012702.

Fomel, S., Luo, S., and Zhao, H., 2009, Fast sweeping method for the factored eikonal equation, Journal of Computational Physics, 228, 6440-6455, doi: 10.1016/j.jcp.2009.05.029.

François, B., Schlef, K.E., Wi, S., and Brown, C.M., 2019, Design considerations for riverine floods in a changing climate – A review, Journal of Hydrology, 574, 557-573, doi: 10.1016/j.jhydrol.2019.04.068.

Gallardo, L.A., and Meju, M.A., 2003, Characterization of heterogeneous near-surface materials by joint 2D inversion of DC resistivity and seismic data, Geophysical Research Letters, 30(13), 1658-1658, doi: 10.1029/2003GL017370.

Gao, G., Abubakar, A., and Habashy, T.M., 2012, Joint inversion of borehole electromagnetic and sonic measurements, SEG Technical Program Expanded Abstracts, 1-6, doi: 10.1190/segam2012-0133.1.

Garofalo, F., 2014, Physically constrained joint inversion of seismic and electrical data for near-surface application, Ph.D. thesis, Politecnico di Torino.

Garofalo, F., Sauvin, G., Socco, L.V., and Lecomte, I., 2015, Joint inversion of seismic and electric data applied to 2D media, Geophysics, 80(4), 93–104, doi: 10.1190/geo2014-0313.1.

Gerstenberger, M. C., Marzocchi, W., Allen, T., Pagani, M., Adams, J., Danciu, L., Field, E.H., Fujiware, H., Luco, N., Ma, K.-F., Meletti, C., and Petersen, M.D., 2020, Probabilistic seismic hazard analysis at regional and national scales: State of the art and future challenges, Reviews of Geophysics, 58, doi: 10.1029/2019RG000653.

Gouédard, P., Yao, H., van der Hilst, R. D., and Verdel, A., 2010, Surface-wave eikonal tomography in a scattering environment, SEG Technical Program Expanded Abstracts, 1919-1923, doi: 10.1190/1.3513217.

Grigoli, F., Cesca, S., Priolo, E., Rinaldi, A.P., Clinton, J.F., Stabile, T. A., Dost, B., Fernandez, M.G., Wiemer, S., and Dahm, T., 2017, Current challenges in monitoring, discrimination, and management of induced seismicity related to underground industrial activities: A European perspective, Reviews of Geophysics., 55, 310– 340, doi:10.1002/2016RG000542.

Gu, Y.J., Dziewonski, A.M., Su, W. and Ekström, G., 2001. Models of the mantle shear velocity and discontinuities in the pattern of lateral heterogeneities, Journal of Geophysical Research: Solid Earth, 106(B6), 11169-11199, doi: 10.1029/2001JB000340.

Guo, Q., Fu, B., Shi, P., Cudahy, T., Zhang, J. and Xu, H., 2017, Satellite monitoring the spatial-temporal dynamics of desertification in response to climate change and human activities across the Ordos Plateau, China, Remote sensing, *9*(6), 525, doi: 10.3390/rs9060525.

Haber, E., and Holtzman Gazit, M., 2013, Model fusion and joint inversion, Surveys in Geophysics, 34, 675–695, doi: 10.1007/s10712-013-9232-4.

Haney, M.M., and Qu, L., 2010, Rayleigh wave dispersion curve inversion: Occam versus the L1-norm, 80th SET Annual International Meeting, Expanded Abstracts, 1871-1876, doi:10.1190/1.3513206.

Haskell, N., 1953, The dispersion of surface waves on multilayered media, Bulletin of the Seimological Society of America, 43, 17-34, 10.1785/BSSA0430010017.

Heincke, B., Jegen, M., Moorkamp, M., Hobbs, R.W. and Chen, J., 2017, An adaptive coupling strategy for joint inversions that use petrophysical information as

constraints, Journal of Applied Geophysics, 136, 279-297, doi: 10.1016/j.jappgeo.2016.10.028.

Hole, J.A., and Zelt, B.C., 1995, 3-D finite-difference reflection traveltimes, Geophysical Journal International, 121, 427-434, doi: 10.1111/j.1365-246X.1995.tb05723.x.

Ikeda, T., and Tsuji, T., 2020, Two-station continuous wavelet transform cross-coherence analysis for surface-wave tomography using active-source seismic data, Gephysics, 85, 17- 28, doi: 10.1190/geo2019-0054.1.

Jegen, M.D., Hobbs, R.W., Tarits, P. and Chave, A., 2009, Joint inversion of marine magnetotelluric and gravity data incorporating seismic constraints: Preliminary results of sub-basalt imaging off the Faroe Shelf, Earth and Planetary Science Letters, 282, 47-55, doi: 10.1016/j.epsl.2009.02.018.

Jordi, C., Doetsch, J., Günther, T., Schmelzbach, C., Maurer, H., and Robertsson, J.O.A., 2019, Structural joint inversion on irregular meshes, Geophysical journal international, 220(3), 1995-2008, doi: 10.1093/gji/ggz550.

Karimpour, M., Slob, E., and Socco, L.V., 2022, A comparison of straight-ray and curved-ray surface wave tomography approaches at near-surface studies, Solid Earth [preprint], doi: 10.5194/egusphere-2022-279.

Karimpour, M., Slob, E.C., and Socco, L.V., 2022, Physically constrained 2D joint inversion of surface and body wave tomography, Journal of Environmental and Engineering Geophysics, 27(2), 57-71, doi: 10.32389/JEEG21-031.

Kästle, E.D., El-Sharkawy, A., Boschi, L., Meier, T., Rosenberg, C., Bellahsen, N., Cristiano, L., and Weidle, C., 2018, Surface wave tomography of the Alps using ambient-noise and earthquake phase velocity measurements, Journal of Geophysical Research: Solid Earth, 123, 1770–1792, doi: 10.1002/2017JB014698.

Kelemen, P., Benson, S.M., Pilorgé, H., Psarras, P., and Wilcox, J., 2019, An Overview of the Status and Challenges of CO2 Storage in Minerals and Geological Formations, Frontiers in Climate, 1, doi: 10.3389/fclim.2019.00009.

Khosro Anjom, F., and L.V. Socco, 2019, Improved surface wave tomography: Imposing wavelength-based weights: Extended Abstracts, 38th GNGTS national convention.

Khosro Anjom, F., 2021, S-wave and P-wave velocity model estimation from surface waves, Ph.D. thesis, Politecnico di Torino.

Kugler, S., Bohlen, T., Forbriger, T., Bussat, S., and Klein, G., 2007, Scholte wave tomography for shallow-water marine sediments, Geophysical Journal International, 168, 551–570, doi: 10.1111/j.1365-246X.2006.03233.x.

Kutanaei, S.S., and Choobbasti, A.J., 2019, Prediction of liquefaction potential of sandy soil around a submarine pipeline under earthquake loading, Journal of Pipeline Systems Engineering and Practice, 10(2), doi: 10.1061/(ASCE)PS.1949-1204.0000349.

Laske, G., 1995, Global observations of off-great-circle propagation of long-period surface waves, Geophysical Journal International, 13, 245-259, doi: 10.1111/j.1365-246X.1995.tb06673.x.

Levander, A.R., 1988, Fourth-order finite-difference P-SV seismograms, Geophysics, 53(11), 1425-1436, doi: 10.1190/1.1442422.

Levshin, A.L., Barmin, M.P., Ritzwoller, M.H., and Trampert, J., 2005, Minor-arc and major-arc global surface wave diffraction tomography, Physics of the Earth and Planetary Interiors, 149, 205–223, doi: 10.1016/j.pepi.2004.10.006.

Li, X.D., and Romanowicz, B., 1996, Global mantle shear velocity model developed using nonlinear asymptotic coupling theory, Journal of Geophysical Research: Solid Earth, 101(10), 22245-22272.

Lien, M., 2013, Simultaneous joint inversion of amplitude-versus-offset and controlled-source electromagnetic data by implicit representation of common parameter structure, Geophysics, 78(4), 15-27, doi: 10.1190/geo2012-0188.1.

Lin, F.C., Moschetti, M.P., and Ritzwoller, M.H., 2008, Surface wave tomography of the western United States from ambient seismic noise: Rayleigh and Love wave phase velocity maps, Geophysical Journal International, 173(1), 281-298, doi: 10.1111/j.1365-246X.2008.03720.x.

Lin, F.C., Ritzwoller, M.H., and Snieder, R., 2009, Eikonal tomography: Surface wave tomography by phase front tracking across a regional broad-band seismic array, Geophysical Journal International, 177, 1091-1110, doi: 10.1111/j.1365-246X.2009.04105.x.

Linde, N., Tryggvason, A., Peterson, J.E., Hubbard, S.S., 2008, Joint inversion of crosshole radar and seismic traveltimes acquired at the South Oyster bacterial transport site, Geophysics, 73, 29-37, doi: 10.1190/1.2937467.

Manzi, M., Cooper, G., Malehmir, A., Durrheim, R., and Nkosi, Z., 2015, Integrated interpretation of 3D seismic data to enhance the detection of the gold-bearing reef: Mponeng Gold mine, Witwatersrand Basin (South Africa). Geophysical Prospecting, 63(4), 881-902, doi: 10.1111/1365-2478.12273.

Maraschini, M., and Foti, S., 2010, A Monte Carlo multimodal inversion of surface waves, Geophysical Journal International, 182(3), 1557-1566, doi: 10.1111/j.1365-246X.2010.04703.x.

Marquardt, D.W., 1963, An algorithm for least squares estimation of nonlinear parameters, Journal of the Society of Industrial Applied Mathematics, 11(2), 431-441, doi: 10.1137/0111030.

Masters, G., Jordan, T.H., Silver, P.G., and Gilbert, F., 1982, Aspherical Earth structure from fundamental spheroidal-mode data, Nature, 298(5875), 609-613, doi: 10.1038/298609a0.

Mollaret, C., Wagner, F.M., Hilbich, C., Scapozza, C. and Hauck, C., 2020, Petrophysical joint inversion applied to alpine permafrost field sites to image subsurface ice, water, air, and rock contents, Frontiers in Earth Science, 8, 85, doi: 10.3389/feart.2020.00085.

Molodtsov, D.M., Colombo, D., Roslov, Y.V., Troyan, V.N., Kashtan, B.M., 2015, Comparison of structural constraints for seismic-MT joint inversion in a subsalt imaging problem, Saint Petersburg State University Bulletin, 4, 230-236.

Montagner, J.P., 1991, Global upper mantle tomography of seismic velocities and anisotropies, Journal of Geophysical Research Atomospheres, 96351(10), 20337-20351, doi: 10.1029/91JB01890.

Moorkamp, M., Heincke, B., Jegen, M., Roberts, A.W., and Hobbs, R.W., 2011, A framework for 3-D joint inversion of MT, gravity and seismic refraction data, Geophysical Journal International, 184(1), 477-493, doi: 10.1111/j.1365-246X.2010.04856.x.

Mourey, J., Marcuzzi, M., Ravanel, L., and Pallandre, F., 2019, Effects of climate change on high Alpine mountain environments: Evolution of

mountaineering routes in the Mont Blanc massif (Western Alps) over half a century, Arctic, Antarctic, and Alpine Research, 51(1), 176-189, doi: 10.1080/15230430.2019.1612216.

Nataf, H.C., Nakanishi, I., and Anderson, D.L., 1986, Measurements of mantle wave velocities and inversion for lateral heterogeneities and anisotropy. III – Inversion, Journal of Geophysical Research Atmospheres, 91(7), 7261-7307, doi: 10.1029/JB091iB07p07261.

Noble, M., Gesret, A., and Belayouni, N., 2014, Accurate 3-D finite difference computation of traveltimes in strongly heterogeneous media, Geophysical Journal International, 199, 422 1572-1585, doi: 10.1093/gji/ggu358.

Ogunbo, J.N., Marquis, G., Zhang, J., and Wang, W., 2018, Joint inversion of seismic traveltime and frequency-domain airborne electromagnetic data for hydrocarbon exploration, Geophysics, 83, 9-22, doi: 10.1190/geo2017-0112.1.

Papadopoulou, M., 2021, Surface wave methods for mineral exploration, Ph.D. thesis, Politecnico di Torino.

Park, C.B., Miller, R.D., and Xia, J., 1998, Imaging dispersion curves of surface waves on multi-channel record, SEG Technical Program Expanded Abstracts, 1377-1380, doi: 10.1190/1.1820161.

Pasquet, S., Bodet, L., Longuevergne, L., Dhemaied, A., Camerlynck, C., Rejiba, F., and Guérin, R., 2015, Near Surface Geophysics, 13(4), 315-332, doi: 10.3997/1873-0604.2015028.

Passeri, F., 2019, Development of an advanced geostatistical model for shear wave velocity profiles to manage uncertainties and variabilities in ground response analyses, Ph.D. thesis, Politecnico di Torino.

Paulatto, M., Moorkamp, M., Hautmann, S., Hooft, E., Morgan, J.V., and Sparks, R.S.J., 2019, Vetically extensive magma reservoir revealed from joint inversion and quantitative interpretation of seismic and gravity data, Journal of Geophysical Research: Solid Earth, 124, 11170-11191, doi: 10.1029/2019JB018476.

Podvin, P., and Lecomte, I., 1991, Finite difference computation of traveltimes in very contrasted velocity models: a massively parallel approach and its associated

tools, Geophysical Journal International, 105, 271-284, doi: 10.1111/j.1365-246X.1991.tb03461.x.

Qian, J., and Symes, W.W., 2002, An adaptive finite-difference method for traveltimes and amplitudes, Geophysics, 67, 167-176, doi: 10.1190/1.1820878.

Qin, T., Zhao, Y., Hu, S., An, C., Bi, W., Ge, S., Capineri, L., and Bohlen, T., 2020, An interactive integrated interpretation of GPR and Rayleigh Wave Data Based on the Genetic Algorithm, Surveys in Geophysics, 41, 549-574, doi: 10.1007/s10712-019-09543-x.

Rawlinson, N., and Sambridge, M., 2004a, Multiple reflection and transmission phases in complex layered media using a multistage fast marching method, Geophysics, 69, 1338-1350, doi: 10.1190/1.1801950.

Rawlinson, N., 2005, FMST: Fast marching surface tomography package: Research School of Earth Sciences, Australian National University, Canberra, ACT, 0200.

Rector, J.W., Pfeiffe, J., Hodges, S., Kingman, J., and Sprott, E., 2015, Tomographic imaging of surface waves: A case study from the Phoenix Mine, Battle Mountain, Nevada, The Leading Edge, 34, 1360-1364, doi: 10.1190/tle34111360.1.

Richart, F.E., Hall, J.R., and Woods, R.D., 1970, Vibrations of soils and foundations, Prentice-Hall.

Ritzwoller, M.H., and Levshin, A.L., 1998, Eurasian surface wave tomography: Group velocities, Journal of Geophysical Research Solid Earth, 103, 4839- 4878, doi: 10.1029/97JB02622.

Ritzwoller, M.H., Shapiro, N.M., Barmin, M.P., and Levshin, A.L., 2002, Global surface wvae diffraction tomography, Journal of geophysical Research, 107, B12, 2335, doi:10.1029/2002JB001777.

Roe, G.H., Baker, M.B., and Herla, F., 2017, Centennial glacier retreat as categorical evidence of regional climate change, Nature Geoscience, 10(2), 95-99, doi: 10.1038/ngeo2863.

Rosendahl, K.E, 2019, EU ETS and the waterbed effect, Nature Climate Change, 9, 734–735, doi: 10.1038/s41558-019-0579-5

Shapiro, N.M., and Campillo, M., 2004, Emergence of broadband Rayleigh waves from correlations of the ambient seismic noise, Geophysical Research Letters, 31(7), doi: 10.1029/2004GL019491.

Shapiro, N.M., Campillo, M., Stehly, L., and Ritzwoller, M.H., 2005, High-resolution surface-wave tomography from ambient seismic noise, Science, 307(5715), 1615-1618, doi: 10.1126/science.1108339.

Sheriff, R.E., 2002, Encyclopedic Dictionary of Applied Geophysics, 4, SEG, doi: 10.1190/1.9781560802969.

Sieminski, A., Lévêque, J.-J., and Debayle, E., 2004, Can finite-frequency effects be accounted for in ray theory surface wave tomography?, Geophysical Research Letters, 31, L24614, doi:10.1029/2004GL021402.

Smith, M.F., and Masters, G., 1989, Aspherical structure constraints from free oscillation frequency and attenuation measurements, Journal of Geophysical Research Atmospheres, 94(2), 1953-1976, doi: 10.1029/JB094iB02p01953.

Socco, L.V., Boiero, D., Foti, S., and Wisen, R., 2009, Laterally constrained inversion of ground roll from seismic reflection records, Geophysics, 74, 35-45, doi: 10.1190/1.3223636.

Spetzler, J., Trampert, J., and Snieder, R., 2001, Are we exceeding the limits of the great circle approximation in global surface wave tomography?, Geophysical research letters, 28(12), 2341-2344, doi: 10.1029/2000GL012691

Spetzler, J., Trampert, J., and Snieder, R., 2002, The effect of scattering in surface wave tomography, Geophysical Journal International, 149, 755-767, doi: 10.1046/j.1365-246X.2002.01683.x.

Tanimoto, T., 1986, The Backus–Gilbert approach to the 3-D structure in the upper mantle–II. SH and SV velocity, Geophysical Journal International, 84(1), 49-69, doi: 10.1111/j.1365-246X.1986.tb04344.x.

Thomas, S., Pillai, G.N., Pal, K., and Pushpak, J., 2016, Prediction of ground motion parameters using randomized ANFIS (RANFIS), Applied Soft Computing, 40, 624-634, doi: 10.1016/j.asoc.2015.12.013.

Thomson, W.T., 1950, Transmission of elastic waves through a stratified solid medium, Journal of applied Geophysics, 21, 89-93, doi: 10.1063/1.1699629.

Trampert, J., and Woodhouse, J.H., 1995, Global phase velocity maps of Love and Rayleigh waves between 40 and 150 seconds, Geophysical Journal International, 122(2), pp.675-690, doi: 10.1111/j.1365-246X.1995.tb07019.x

Trampert, J., and Spetzler, J., 2006, Surface wave tomography: finite-frequency effects lost in the null space, Geophysical Journal International, 164, 394-400, doi: 10.1111/j.1365-246X.2006.02864.x.

Toney, L. D., Abbott, R.E., Preston, L.A., Tang, D.G., Finlay, T., Phillips-Alonge, K., 2019, Joint Body- and Surface-Wave Tomography of Yucca Flat, Nevada, Using a Novel Seismic Source, Bulletin of the Seismological Society of America, 109 (5), 1922-1934, doi: 10.1785/0120180322.

Varangoulis, D., 2014, Surface wave tomography: survey design and data coverage, M.Sc. thesis, Politecnico di Torino.

Vidale, J., 1988, Finite-difference calculation of travel times, Bulletin of the Seismological Society of America, 78, 2062-2076.

Vignoli, G., Guillemoteau, J., Barreto, J., and Rossi, M., 2021, Reconstruction, with tunable sparsity levels, of shear wave velocity profiles from surface wave data, Geophysical Journal International, 225(3), 1935-1951, doi: 10.1093/gji/ggab068.

Virieux, J., 1986, P-SV wave propagation in heterogeneous media: velocity-stress finite-difference method, Geophysics, 51(4), 889-901, doi: 10.1071/EG984265a.

Vozoff, K., and Jupp, D.L.B., 1975, Joint inversion of geophysical data, Geophysical Journal of the Royal Astronomical Society, 42, 977- 991, doi: 10.1111/j.1365-246X.1975.tb06462.x.

Wagner, F.M., Mollaret, C., Günther, T., Kemna, A., and Hauck, C., 2019, Quantitative imaging of water, ice and air in permafrost systems through petrophysical joint inversion of seismic refraction and electrical resistivity data, Geophysical Journal International, 219, 1866-1875, doi: 10.1093/gji/ggz402.

Wang, X., Zeng, X., Li, J., Yang, X., and Wang, H., 2018, A review on recent advancements of substructures for offshore wind turbines, Energy Conversion and Management, 158, 103-119, doi: 10.1016/j.enconman.2017.12.061.

Wathelet, M., Jongsman, D., and Ornberger, M., 2004, Surface wave inversion using a direct search algorithm and its application to ambient vibration measurements, Near Surface Geophysics, 2, 211-221, doi: 10.3997/1873-0604.2004018.

Wisén, R., and V. Christiansen, 2005, Laterally and Mutually Constrained Inversion of Surface Wave Seismic Data and Resistivity Data, Journal of Environmental and Engineering Geophysics, 10, 251-262, doi: 10.2113/JEEG10.3.251.

Woodward, R.L., and Masters, G., 1991, Lower-mantle structure from ScS–S differential travel times, Nature, 352(6332), 231-233, doi: 10.1038/352231a0.

Woodhouse, J.H., and Dziewonski, A.M., 1984, Mapping the upper mantle: Three-dimensional modelling of Earth structure by inversion of seismic waveforms, Journal of Geophysical Research Atmospheres, 89(7), 5953-5986, doi: 10.1029/JB089iB07p05953.

Xia, J., Miller, R.D., and Park, C.B., 1999, Estimation of near-surface shear-wave velocity by inversion of Rayleigh waves, Geophysics, 64(3), 691-700, doi: 10.1190/1.1444578.

Yao, H., van der Hilst, R.D., and De Hoop, M.V., 2006, Surface-wave array tomography in SE Tibet from ambient seismic noise and two-station analysis—I. Phase velocity maps, Geophysical Journal International, 166(2), 732-744, doi: 10.1111/j.1365-246X.2006.03028.x.

Yao, H., Beghein, C., and van der Hilst, R., 2008, Surface wave array tomography in SE Tibet from ambient seismic noise and two-station analysis - II. Crustal and upper-mantle structure, Geophysical Journal International, 173, 205-219, doi: 10.1111/j.1365-246X.2007.03696.x.

Yao, H., van der Hilst, R.D., and Montagner, J.-P., 2010, Heterogeneity and anisotropy of the lithosphere of SE Tibet from surface wave array tomography, Journal of geophysical Research: Solid Earth, 115(12), doi:10.1029/2009JB007142.

Yoshizawa, K., and Kennett, B.L.N., 2004, Multimode surface wave tomography for the Australian region using a three-stage approach incorporating

finite frequency effects, Journal of geophysical research solid earth, 109, doi: 10.1029/2002JB002254.

Zhang, J., and Morgan, F.D., 1997, Joint seismic and electrical tomography, 10th EEGS Symposium on the Application of Geophysics to Engineering and Environmental Problems, 391-396, doi: 10.3997/2214-4609-pdb.204.1997_040.

Zhang, L., Rector, J.W., and Hoversten, G.M., 2005, Eikonal solver in the celerity domain, Geophysical Journal International, 162, 1-8, doi: 10.1111/j.1365-246X.2005.02626.x.

Zhang, X., Curtis, A., Galetti, E., and De Ridder, S., 2018, 3-D Monte Carlo surface wave tomography, Geophysical Journal International, 215(3), 1644-1658, doi: 10.1093/gji/ggy362

Zhou, Y., Dahlen, F.A., Nolet, G., and Laske, G., 2005, Finite-frequency effects in global surface-wave tomography, Geophysical Journal International, 163, 1087-1111, doi: 10.1111/j.1365-246X.2005.02780.x.